Master's thesis

NTNU
Norwegian University of Science and Technology
Faculty of Engineering
Department of Marine Technology

Apoorva Sinha

VIV suppression in 2D circular cylinders through staggered grooves: A numerical investigation at low Reynolds number

Master's thesis in Marine Technology
Supervisor: Lars Erik Holmedal
June 2023

NTNU
Norwegian University of
Science and Technology

Apoorva Sinha

VIV suppression in 2D circular cylinders through staggered grooves: A numerical investigation at low Reynolds number

Master's thesis in Marine Technology
Supervisor: Lars Erik Holmedal
June 2023

Norwegian University of Science and Technology
Faculty of Engineering
Department of Marine Technology

Abstract

Vortex-induced vibration (VIV), a ubiquitous fluid-structure interaction phenomenon, plays a crucial role in the operational safety and longevity of various engineering structures subjected to fluid flow, such as marine risers and offshore structures among others. The VIV phenomenon, characterized by the shedding of vortices and consequential oscillations of the structure, often induces fatigue and potential structural failure. Symmetric staggered grooves have recently emerged as a promising passive VIV control mechanism, but a comprehensive understanding and systematic exploration of their performance under varying conditions is yet to be achieved.

This thesis is devoted to an in-depth numerical analysis of the impact of symmetric staggered grooves on VIV suppression in a two-dimensional circular cylinder at a Reynolds number (Re) of 100. This research harnesses the integration of computational fluid dynamics (CFD) and computational structural dynamics (CSD) simulation tools to form a fluid-structure interaction (FSI) model using the open-source package OpenFOAM to model and simulate different grooved cylinder geometries with variations in groove depth, width, and position.

The first phase of the research focuses on the simulation and analysis of a smooth elastically mounted 2D cylinder, identifying the lock-in regime, a crucial aspect of VIV. This part of the research has already been conducted in a previous study that this work is a continuation of. Subsequently, the study systematically explores the relationship between groove parameters and VIV suppression performance in the grooved cylinder cases. A total of 36 grooved-cylinder configurations are analysed and the findings are reported. Intriguing correlations between VIV amplitudes and groove parameters were identified throughout these simulations. Notably, it was observed that as the groove width increased at a 90° position, VIV amplitudes reciprocally decreased. In contrast, VIV amplitudes escalated as the groove width increased at a 60° position. The grooves positioned at 90° registered a maximum reduction in cross-flow amplitude of 6.4% and an 11.1% reduction in in-line amplitude. On the other hand, for the grooves situated at a 60° position, there was a recorded maximum increase of 4.6% in cross-flow amplitude and a 6.4% increament in the in-line amplitude, when compared to the smooth cylinder case. Special attention was

directed towards these specific groove positions based on intriguing observations from the analysis conducted on the smooth cylinder case. It was noted that these positions were characterised by regions of low vorticity, which are usually linked with flow separation. Therefore, it was expected that these positions, specifically at 60° and 90°, might have a significant effect on VIV suppression. This led to further investigation of how altering groove parameters at these positions could influence VIV reduction. Meanwhile, other positions displayed insignificant deviation from the smooth cylinder case, suggesting that the groove position plays a significant role in VIV suppression.

The present research dives deeper into the hydrodynamics around the cylinders and inside the grooves, encompassing analyses of vorticity distribution. The results contribute to enhancing the understanding of VIV mechanisms, particularly the influence of grooves on vortex shedding and fluid-structure interaction.

This comprehensive investigation provides insights into the design and optimization of grooves for efficient VIV suppression, thereby significantly contributing to the development of safer and more reliable engineering structures exposed to fluid flow. The findings of this study, especially the dependencies of VIV amplitudes on groove parameters, has the potential to have significant implications for engineering applications dealing with VIV-induced fatigue and failure.

Through this computational exploration, this thesis fills the existing research gap in the systematic study of symmetric staggered grooves for VIV suppression, providing a reference point for future studies and designs aiming to optimise VIV suppression techniques. The understanding derived from this research will pave the way for extending these investigations to three-dimensional structures and turbulent flows, further bolstering our capability to control VIV in a broader range of real-world applications.

Acknowledgements

Completing this thesis has been a profoundly enriching journey, and I genuinely feel that it wouldn't have been achievable without the considerable support I received along the way. The academic challenges I faced during my time at NTNU pushed me to grow and learn beyond measure, for which I am deeply grateful.

I extend my heartfelt gratitude to my thesis supervisor, Lars Erik Holmedal, whose invaluable insights and regular availability greatly aided my progress. I also wish to express my profound appreciation to Jianxun Zhu and Cai Tian who guided me at every step of the way. Their consistent guidance and remarkable patience contributed significantly to my work.

A note of thanks also goes out to the faculty and staff who imparted their knowledge and expertise to me over the past three years. Your dedication to education has truly been instrumental in shaping my academic journey.

On a personal note, I cannot express enough gratitude to my parents and brother. Their unwavering support and understanding laid the foundation for this work. My deepest thanks to my girlfriend, Martine, for her uplifting encouragement during times when my tasks seemed impossible.

Lastly, I would like to acknowledge the support and encouragement of my friends and colleagues. Your camaraderie has been a great source of strength and motivation throughout this process.

Apoorva Sinha

June 2023

Contents

List of Figures

List of Tables

Nomenclature

Symbol	Description	Unit
c	Structural damping	N.s/m
C_D	Drag coefficient	[-]
$C_{D,mean}$	Mean drag coefficient	[-]
$C_{D,rms}$	RMS of drag coefficient	[-]
C_L	Lift coefficient	[-]
$C_{L,rms}$	RMS of lift coefficient	[-]
Co	Courant number	[-]
Co_{max}	Maximum Courant number	[-]
d	Groove depth	m
D	Cylinder diameter	m
f*	Frequency ratio	[-]
f_n	Natural frequency	Hz
f_{shed}	Vortex shedding frequency	Hz
H	Cross-sectional height of cylinder	m
k	Spring constant	N/m
m	Structural mass of cylinder	kg
m_f	Mass of displaced fluid	kg
m*	Mass ratio	[-]
n_{cells}	Number of cells	[-]
p	Position of groove	°
P	Fluid pressure	$kg/(m.s^2)$
Re	Reynolds number	[-]
St	Strouhal number	[-]
u	Velocity component in x-direction	m/s
U*	Reduced velocity	[-]
U_∞	Freestream velocity	m/s
v	Velocity component in y-direction	m/s
w	Groove width	°
W	Grid velocity	m/s

x	In-line displacement	m/s
x_{rms}	RMS of in-line displacement	m/s
y	Transverse displacement	m/s
y_{max}	Maximum transverse displacement	m/s
y_{rms}	RMS of transverse displacement	m/s
ζ	Damping ratio	[-]
μ	Dynamic viscosity of the fluid	$N.s/m^2$
ν	Kinematic viscosity of the fluid	m^2/s
ρ_s	Fluid density	kg/m^3
Abbreviations		
ALE	Arbitrary Lagrangian-Eulerian method	
CSD	Computational Structural Dynamics	
CFD	Computational Fluid Dynamics	
DOF	Degrees of Freedom	
DNS	Direct Numerical Simulation	
FSI	Fluid-Structure Interaction	
VIV	Vortex Induced Vibration	

1

Introduction

1.1. Motivation

Vortex-induced vibration (VIV) is a critical phenomenon encountered in various engineering applications, particularly in offshore structures, marine risers, and cables exposed to fluid flow. The shedding of vortices in the wake of these structures leads to oscillations, causing fatigue and possible structural failure over time (Bearman, 1984). Thus, understanding and suppressing VIV is of significant importance to ensure the safety and longevity of such structures.

Various VIV suppression techniques have been studied in the past, including strakes, fairings, and other devices that alter the wake of the structure (Sarpkaya, 2004). Recently, symmetrical grooves have shown potential in reducing VIV for circular cylinders and other geometries (Hu et al., 2023). The optimization of groove parameters, such as width, depth, and position, can lead to a more effective VIV suppression design. However, systematic studies on the optimization of these parameters are scarce, and a comprehensive understanding of the effects of staggered grooves on VIV suppression is yet to be achieved.

In light of these challenges, this thesis aims to contribute to the knowledge of VIV suppression by conducting a detailed investigation of the impact of symmetrical staggered grooves on a 2D circular cylinder. The study will focus on low Reynolds number (Re = 100) flow in the lock-in regime, which can be relevant for small-scale structures and applications. Using computational fluid dynamics (CFD) simulations in OpenFOAM, the research will explore the relationship between groove dimensions, angular position, and VIV suppression performance.

This thesis will leverage the power of CFD and fluid-structure interaction (FSI) simulations to optimize the groove parameters, providing a better understanding of the underlying physics behind VIV suppression by symmetrical staggered grooves. The results are expected to offer valuable insights for the development of efficient VIV suppression techniques for offshore structures, marine risers, and other engineering applications prone to VIV-induced fatigue and failure.

Moreover, this work will contribute to the growing body of research on VIV suppression using innovative techniques and designs, such as the use of grooves. The systematic exploration of the design space for groove parameters will help identify optimal configurations for maximum VIV suppression, leading to safer and more durable structures in a wide range of industries.

In summary, the motivation for this thesis lies in the potential of low Reynolds number VIV suppression research to serve as a foundation for more advanced and complex investigations. By first understanding the fundamental mechanisms governing VIV at low Reynolds numbers, the knowledge gained can be applied to tackle more intricate problems in the future. This includes the extension to three-dimensional (3D) structures and turbulent flows, which are commonly encountered in real-world engineering applications like the design of more effective VIV suppression devices for various engineering applications.

1.2. Previous Work

The current research is an extension of the investigations conducted in a prior "specialisation project". This section gives a quick review of that past work and its main findings. Moreover, this review will tie the current work to the earlier research, framing it as a coherent body of work in its entirety.

As outlined in Section 1.1, the fundamental objective of this study is to pinpoint the lock-in region for a 2D cylinder at a Reynolds number of 100, and subsequently examine a range of staggered groove configurations. The aim is to gain insights about effective VIV suppression in relation to groove parameters. During the former study, the primary tasks and achievements were:

1. A comprehensive literature review was undertaken. This exercise not only deepened understanding of the VIV phenomenon but also underlined the relevance of this research. It recognized existing research in the field, making use of the vast body of knowledge that has been built over time.

2. A fundamental fluid-structure interaction (FSI) framework was established, combining the Pimplefoam solver for fluid flow analysis with an integrated structural motion solver for the cylinder, all within the OpenFOAM CFD package. This setup is retained in the current work to ensure consistent comparison.

3. Two strategies were evaluated for managing mesh motion: a morphing mesh and an overset method. The morphing mesh technique reported better alignment with results obtained by (Singh & Mittal, 2005), thus proving to be the more effective of the two.

4. In order to identify the lock-in region, several values of the reduced velocity (U*) were experimented with by modifying the spring stiffness in the mounting setup (chapter 3). A U* value of 5.5 generated high-amplitude vibrations, distinct from those produced at lower and higher U* values. This outcome was consistent with the findings of (Singh & Mittal, 2005). As a result, efforts to suppress these amplitudes focused on this specific lock-in condition, i.e., U* = 5.5.

5. The fluid flow around and in the wake of the cylinder in the lock-in state was thoroughly analyzed. Key areas of interest were marked, including points of separation and regions of low vorticity. This analysis suggested possible positioning of grooves, and configurations with grooves near these identified areas indeed led to significant changes in the VIV oscillation amplitudes (refer to section 5.2).

Additional details from the previous study have been discussed in Section 5.2. Those results are compared with the current findings to observe the impact of varying groove configurations.

1.3. Research objective and question

The primary objective of this thesis is to investigate the suppression of Vortex-Induced Vibrations (VIV) of a 2D circular cylinder subjected to a uniform incoming flow at low Reynolds numbers (Re = 100). The present study aims to explore and assess the effectiveness of employing symmetric staggered grooves as a passive control strategy for VIV suppression. This study is motivated by the need to enhance the understanding of the fundamental physics of VIV and techniques to reduce their impact. Such understanding is critical for improving the design and optimization of engineering structures subjected to fluid flow.

To achieve this objective, the research questions have been formulated as follows:

- *How does the presence of symmetric staggered grooves influence the vortex shedding and fluid-structure interaction mechanisms in the vicinity of a 2D circular cylinder exposed to a uniform flow at Re =100?*
- *What are the optimal parameters for the grooves (for example groove size, and position) to effectively suppress VIV in a circular cylinder at low Reynolds numbers?*
- *How does the implementation of symmetric staggered grooves affect the amplitude of cylinder oscillations and the response frequency in the lock-in regime, compared to a smooth cylinder?*
- *What are the underlying physics governing the VIV suppression using symmetric staggered grooves and the associated impact on the lift and drag coefficients of the 2D cylinder?*

To address these research questions, a systematic investigation has been carried out using the computational fluid dynamics (CFD) package OpenFOAM where the fluid-structure interaction problem has been modeled. As no experimental or prior computational studies are available for direct comparison, the study is self-contained, focusing on modelling and simulation of passive VIV control techniques using 2D grooved cylinders. The research outcomes provide valuable insights into the effectiveness of passive VIV control techniques, contributing to the ongoing efforts to optimize engineering systems and structures and minimize the detrimental effects of VIV.

1.4. Research Approach

In this master's thesis, a comprehensive research approach is adopted to address the research questions and achieve the objectives. The methodology comprises the following key steps:

1. **Critical Review**: A thorough review of the existing literature has been conducted to understand the current state of knowledge on VIV, their suppression techniques, and the application of CFD in studying VIV phenomena. This step enables the identification of knowledge gaps and provides the necessary background to design and implement the numerical simulations. In addition to the review of existing literature, a comprehensive study of the VIV phenomenon and related parameters along with numerical modelling has been conducted and presented in this report.
2. **Numerical Model Development**: A robust and accurate CFD model has been set up using the OpenFOAM package to simulate the fluid-structure interaction (FSI) problem of the various circular cylinders with symmetric staggered grooves subjected to a uniform incoming flow. The model is based on the incompressible Navier-Stokes equations, using appropriate modifications based on Arbitrary Langaragian-Eulerian (ALE) to account for the movement of the cylinder and consequently the morphing of the mesh.
3. **Refinement studies**: A high-quality computational mesh has been generated, ensuring proper resolution in the regions of interest, such as the boundary layer, shear layers, and wake region. Mesh independence studies have been carried out to ensure the reliability of the simulation results. Additionally, a temporal refinement study has been conducted using the maximum specified Courant number (Co_{max}) since an adjustable timestep scheme has been applied in the present study.
4. **Validation and Simulation**: The developed numerical model has been validated against previous computational studies to assess the accuracy and reliability of the model. Then the model is executed to simulate the flow around the various grooved cylinders at Re = 100.
5. **Analysis and Interpretation**: The simulation results have been postprocessed to highlight the influence of groove depth, width, and position on the vortex-induced vibrations. This comprehensive analysis captures the alterations in vorticity fields, flow patterns, and oscillation amplitudes due to different groove parameters. The simulation results have been analyzed to gain insights into the underlying physics governing the VIV suppression using symmetric staggered grooves. The results are also compared with the smooth cylinder case (section 1.2) to systematically investigate the impact of grooves on the cylinder oscillation amplitude, response frequency, lift, and drag coefficients.
6. **Conclusion and Future Work**: Based on the findings of this research, conclusions have been drawn regarding the effectiveness of staggered grooves as a passive control strategy for VIV suppression. Recommendations for future research directions and potential improvements in the modelling approach have been provided.

The research approach outlined above ensures a systematic and rigorous investigation of the VIV suppression using staggered grooves, contributing to the advancement of knowledge in this area and providing valuable insights for the design and optimization of engineering systems and structures subjected to fluid flow.

1.5. Thesis Outline

The thesis report is divided into seven chapters, each contributing towards achieving the objectives discussed in section 1.3. A brief overview of these chapters is as follows:

- Chapter 1 outlines the motivation for this study, establishes the research objectives and details the research approach. It also provides an introduction to the previous work this thesis continues, along with a review of the respective results.

- Chapter 2 presents a thorough literature review, including an exploration of relevant topics that highlight the interconnections among them.

- Chapter 3 presents the numerical setup used in this study. Discussions in this chapter include aspects such as Fluid-Structure Interaction (FSI) modelling and meshing among others.

- Chapter 4 reports the results and discussion from a study conducted to validate the numerical model.

- Chapter 5 reports the results from the mesh convergence and temporal refinement studies. Furthermore, it presents analysis of the grooved cylinders, comparisons with the smooth cylinder case, and discussions around them. Special cases are visualized through the plotting of vorticity contours.

- Chapter 6 presents the conclusions drawn from the entire thesis work.

- Finally, Chapter 7 proposes potential future research directions that can extend and build upon the present study. It also suggests possible improvements to the current model.

2

Literature Review

In this chapter, an overview of the fundamental concepts and principles related to vortex-induced vibrations (VIV) and the flow around a circular cylinder are provided. The discussion covers the different flow regimes, the lock-in phenomenon, and the mechanisms driving VIV among other important topics. Various techniques and strategies that have been employed to control and mitigate VIV are also discussed, including passive and active approaches. Additionally, a review of work done on the VIV of an elastically mounted rigid cylinder is also presented. By understanding the underlying physics and the state-of-the-art in VIV research, this chapter sets the stage for the detailed investigation of VIV suppression at low Reynolds numbers.

2.1. Vortex-induced Vibration (VIV)

Vortex-induced vibration (VIV) is a self-excited vibration phenomenon that occurs when a structure interacts with the vortices shed in its wake as fluid flows around it. The shedding of vortices alternately from either side of the structure leads to fluctuating lift forces, which can cause the structure to vibrate. This section provides a comprehensive overview of VIV, including its underlying mechanisms, relevant parameters, and effects on engineering structures.

2.1.1. Mechanisms of Vortex Shedding and VIV

As fluid flows around a bluff body, such as a circular cylinder, it separates from the surface and creates alternating vortices in the wake. Vortex-induced vibrations (VIV) occur due to the interaction between the separated boundary layers and the free shear layers formed in the wake of a bluff body, such as a circular cylinder (Williamson, 1996).

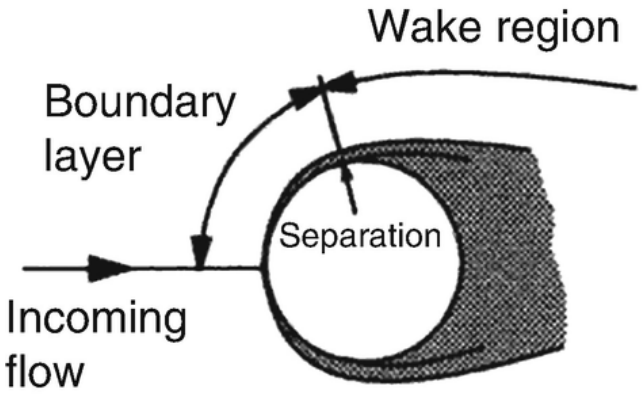

Figure 1: A sketch of flow separation

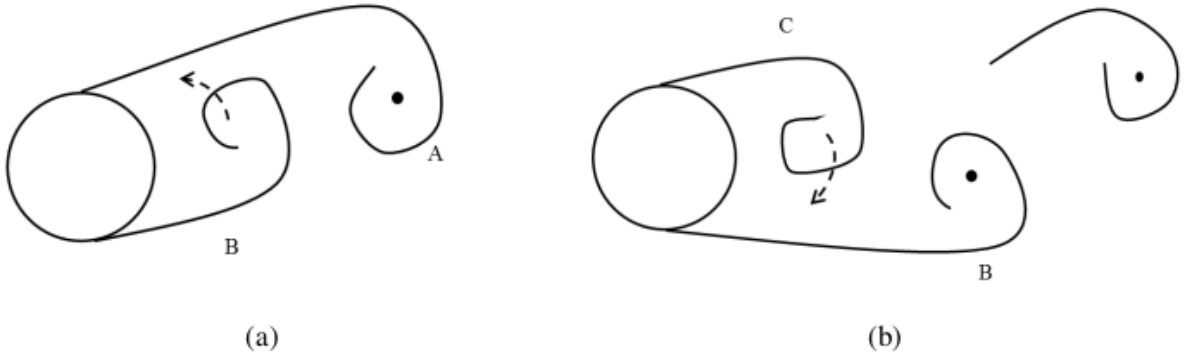

Figure 2: Vortex shedding mechanism

Two free shear layers emerge and define the near-wake as the boundary layer detaches from the cylinder's sides. The cylinder's presence slows the flow within these shear layers' inner portions, while the outer sections maintain pace with the undisturbed flow. This momentum disparity causes the shear layers to 'spin' into the wake, uniting into rotating vortices, as observed by (Williamson & Roshko, 1988). This action generates an alternating pressure distribution on the cylinder's surface, thus initiating the VIV phenomenon and forming a vortex pattern in the cylinder's wake. This pattern is known as the von Kármán vortex street (Williamson, 1996). The alternating shedding of vortices generates fluctuating lift forces, which can induce transverse vibrations in the structure. The interaction between the vibrating structure and the vortex shedding results in a self-sustaining cycle known as VIV. Figure 3 shows vortex street in the wake of a circular cylinder at Re = 140.

Figure 3: Kármán vortex street in the wake of a circular cylinder at Re = 140 (Van Dyke et al., 1983)

2.1.2. Relevant Parameters and Dimensionless Numbers

Several parameters and dimensionless numbers are crucial to understanding VIV, including the Reynolds number (Re), the Strouhal number (St), the reduced velocity (U*), and the mass-damping parameter (m*ζ).

Reynolds number

The Reynolds number (Re) characterizes the flow regime around a bluff body and is defined as:

$$Re = \frac{\rho_s U_\infty D}{\mu} \qquad \textit{(equation 1)}$$

where ρ_s is the fluid density, U_∞ is the free-stream velocity, D is the diameter of the cylinder, and μ is the dynamic viscosity of the fluid.

The Reynolds number represents the ratio between the inertial and the viscous forces (Anderson & Anderson, 2011). The behaviour of the flow around a cylinder is largely governed by the Reynold's number (Re). As the Reynolds number varies, distinct flow regimes with different vortex shedding patterns and flow structures can be observed (Anderson & Anderson, 2011; Blevins, 1994;

Lienhard et al., 1966). The following are the primary flow regimes observed around a circular cylinder:

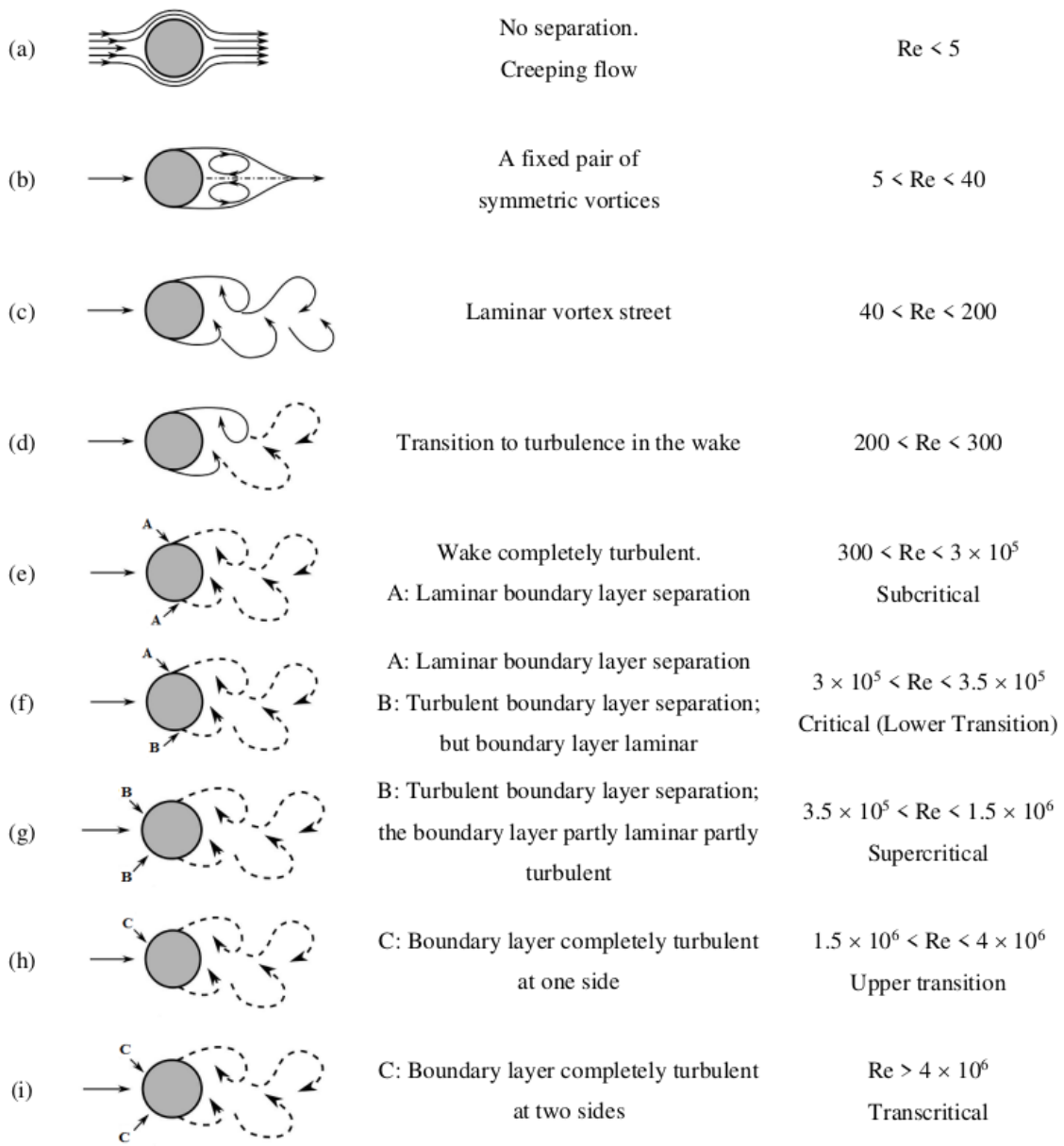

Figure 4: Flow regimes around a circular cylinder (Achenbach & Heinecke, 1981; Feng, 1968; Lienhard et al., 1966; Roshko, 1955; Sumer & Fredsøe, 2006; Van Dyke et al., 1983; Zdravkovich, 1997)

It is crucial to acknowledge, however, that the transition from laminar to turbulent flow is influenced by factors such as cylinder roughness, free-stream turbulence, and blockage ratio. Consequently, the ranges of Reynolds numbers provided here are merely approximations. Additionally, it's worth noting that the literature presents various different characterizations of the flow regimes, and the following discussion presents one such characterization.

1. **Steady flow regime (Re < ~40)**: At low Reynolds numbers, the flow around the cylinder is steady and symmetric. The flow separates smoothly from the cylinder surface, resulting in closed, symmetric recirculation bubbles behind the cylinder.
2. **Periodic vortex shedding (Re ~40 - ~3×10^5)**: As the Reynolds number increases, the flow becomes unsteady and exhibits periodic vortex shedding, known as the von Kármán vortex street. In this regime, alternating vortices are shed from the upper and lower sides of the cylinder, resulting in a wake with an oscillatory pattern. This phenomenon induces fluctuating lift and drag forces on the cylinder, which may lead to Vortex-Induced Vibrations (VIV).
3. **Three-dimensional transition (~1.7×10^5 < Re < ~3.5×10^5)**: As the Reynolds number further increases, the flow undergoes a three-dimensional transition due to the appearance of spanwise instabilities. The flow structure becomes more complex, with streamwise vortices developing along the span of the cylinder.
4. **Turbulent flow regime (Re > ~3.5×10^5)**: At high Reynolds numbers, the flow around the cylinder becomes fully turbulent. The boundary layer transitions to turbulence before flow separation, leading to a delay in separation and a narrower wake. The turbulent flow regime exhibits a wide range of spatial and temporal scales, making it challenging to simulate and analyse.

Understanding the different flow regimes around a circular cylinder and their dependence on the Reynolds number is crucial for predicting and controlling the flow-induced forces and VIV in engineering applications. This knowledge will also provide a foundation for exploring the effectiveness of passive control techniques, such as the use of staggered grooves, to suppress VIV at low Reynolds numbers.

Strouhal number

The Strouhal number (St) is a dimensionless parameter that describes oscillatory behaviors and vortex shedding phenomena. It is characterized as the ratio of inertial forces due to the unsteadiness of the flow or the local acceleration to inertial forces due to changes in velocity from one point in the flow to another.

$$U* = \frac{f_{shed} D}{U_\infty} \qquad \textit{(equation 2)}$$

where f_{shed} is the vortex shedding frequency.

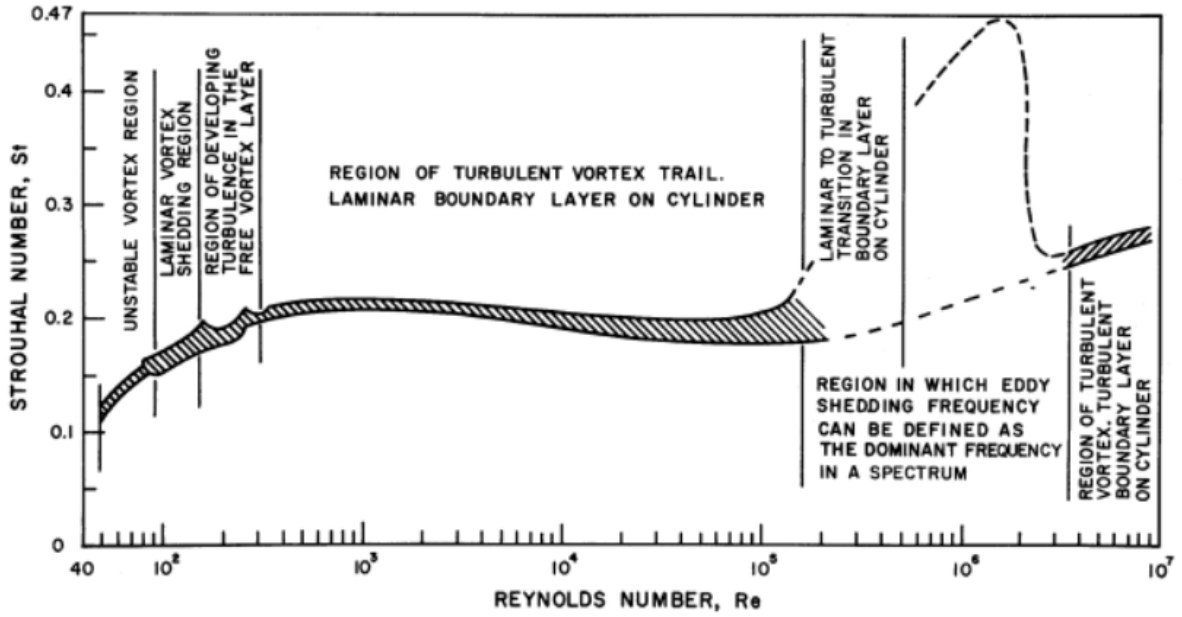

Figure 5: Variation of the Strouhal number with Re for smooth and rough cylinders (Lienhard et al., 1966)

For a smooth circular cylinder exposed to a uniform flow, the Strouhal number holds relatively constant, typically around 0.2, over a wide range of Reynolds numbers (from 100 up to 10^5). This almost constant value underlies the universal nature of the vortex shedding process in the wake of a bluff body, and it's known as the Strouhal regime. However, the value of the Strouhal number can vary under complex flow conditions or with non-standard geometrical configurations. For instance, surface roughness, cylinder rotation, flow turbulence, and cylinder's structural properties are known to affect the Strouhal number. Figure 5 illustrates curves representing the typical values for the Strouhal number for smooth and rough cylinders as function of Re.

Reduced Velocity

The reduced velocity (U*) is a non-dimensional parameter used to describe the relationship between the natural frequency (f_n) of the structure and the vortex shedding frequency:

$$U* = \frac{U_\infty}{f_n D} \qquad \textit{(equation 3)}$$

The critical significance of U* in relation to the vortex movement around the cylinder, which seemingly dictates the range of vibrational excitation, cannot be overstated. The Reduced Velocity directly influences the synchronization (or lock-in) condition (section 2.1.4) where the vortex shedding frequency f_{shed} is close to the structure's natural frequency f_n, leading to significant vibration amplitudes. The lock-in phenomenon typically occurs over a range of U* known as the synchronization range or lock-in band.

The interpretation of the Reduced Velocity is strongly connected to the Strouhal number (St) through the relation St = 1/U* during lock-in. Therefore, for a typical St = 0.2 for a smooth circular cylinder, the synchronization tends to occur around a U* = 5, which is the reciprocal of 0.2. However, the exact synchronization range can vary with changes in flow conditions, Reynolds number, mass ratio, damping ratio, and other factors, such as cylinder's surface properties or geometrical configurations.

Mass Ratio

The mass ratio is the ratio of the oscillating mass (m) to the mass of the displaced fluid (m_f):

$$m* = \frac{m}{m_f} = \frac{4\,m}{\rho \pi D^2 H} \qquad \textit{(equation 4)}$$

The mass ratio has a significant influence on the response characteristics of a body subjected to VIV. It determines the level of structural inertia relative to the fluid forces and directly affects the oscillation frequency and amplitude of the structure under fluid flow. Lower mass ratios typically result in larger oscillation amplitudes due to the reduced inertial resistance to fluid forces. High mass ratios can reduce the structural response due to the increased inertia of the body. However, a decrease in mass ratio might also extend the lock-in range, leading to sustained vibrations over a wider range of U* (Blevins & Coughran, 2009; Williamson & Govardhan, 2004).

Damping Ratio

The Damping Ratio is a dimensionless measure of the damping property of the system. In the context of VIV, it represents the system's inherent capability to dissipate vibrational energy (Bearman, 1984).

Mathematically, Damping Ratio is defined as the ratio of the actual damping to the critical damping, where critical damping is the minimum damping that will allow a displaced system to return to its original position without oscillating. Thus, the Damping Ratio gives an idea of how quickly the system will come to rest.

$$\zeta = \frac{c}{2\sqrt{k\,m}} \qquad \textit{(equation 5)}$$

where c is the damping coefficient, k is the stiffness of the structure, and m is the oscillating mass.

For fluid-structure interactions, a lower damping ratio means the structure will take longer to stop vibrating once set in motion by fluid flow. The structure will also tend to oscillate more significantly within the lock-in range. On the other hand, a higher damping ratio helps to suppress the vibration amplitudes and shortens the lock-in range, providing an effective means to control the adverse effects of VIV (Khalak & Williamson, 1999).

Moreover, the Damping Ratio also affects the phase relationships between the lift forces and the structure's motion in VIV, leading to different vortex shedding modes and flow patterns around the structure (Govardhan & Williamson, 2000).

In the present study, however, the damping coefficient is set to zero. This decision allows the cylinder to oscillate freely, particularly in conditions where lock-in occurs. By minimizing external damping, the study aims to explore the pure interactions between the fluid and the structure.

Other influencing parameters

Though the Strouhal and Reynolds numbers play a big part in VIV, there are other factors that can affect the flow dynamics around a bluff body. Figure 6, based on the compilation by (Zdravkovich, 1997), shows these additional factors. However, their effect on VIV isn't as strong as the Reynolds and Strouhal numbers.

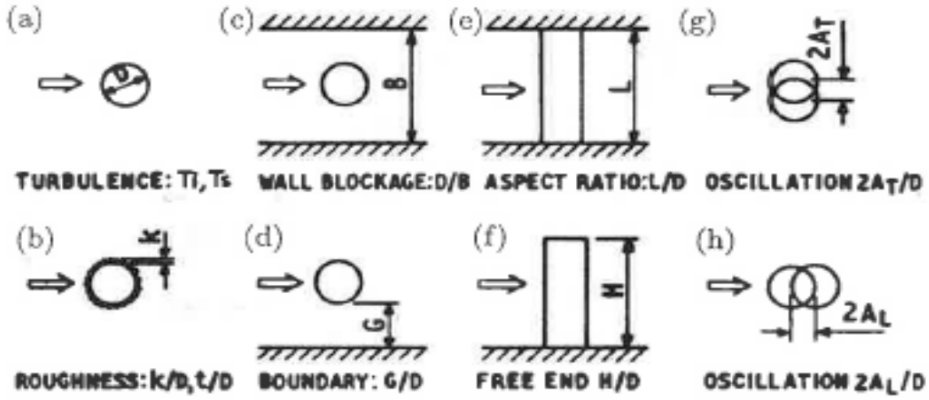

Figure 6 Typical disturbances impacting VIV

2.1.3. VIV Effects on Engineering Structures

Vortex-Induced Vibrations (VIV) represent a major concern in engineering, particularly in structures with significant exposure to fluid flow such as offshore platforms, marine risers, cables, and bridge piers. The self-excited, resonant oscillations induced by VIV can lead to stress concentration and fatigue damage, accelerating the wear and tear of these structures (Blevins, 1990). In some cases, the persistent cyclical forces can result in catastrophic failure, endangering both human lives and environmental safety.

Besides structural integrity, VIV also presents challenges in efficiency and performance. Noise and increased drag, for example, are side effects of VIV that can impair the operational efficiency of marine vessels or wind turbines. The resulting vibrations can also lead to wear of mechanical parts, resulting in additional maintenance requirements and shortened operational lifetimes of these structures.

2.1.4. Lock-in phenomenon

The lock-in phenomenon, also known as synchronization, is a critical aspect of VIV. This phenomenon occurs when the shedding frequency of the vortices f_{shed} approaches the natural frequency of the structure f_n, resulting in a strong coupling between the two. During lock-in, as the vortex shedding frequency synchronizes with the structure's oscillation frequency, large-amplitude oscillations occur in the structure. This synchronization can significantly increase the structural response, causing fatigue and potential damage to the structure. The lock-in phenomenon is typically observed in a specific range of reduced velocities (U*). The range of reduced velocities

where lock-in occurs is often referred to as the lock-in region or synchronization region. The precise boundaries of this region can vary depending on factors such as the structural damping, fluid properties, and geometry of the structure. Understanding and mitigating the lock-in phenomenon is crucial in the design of structures subjected to VIV, as it can significantly impact their performance and long-term durability.

Figure 7 illustrates the classical self-excited oscillation plot showing the lock-in nature of the cylinder oscillation in self-excited conditions. The two features of the plot show the reduced velocity (Vr=U/fD) plotted against both the amplitude-to-diameter ratio (Ay/D) and the ratio of vortex- shedding frequency to natural frequency (fs/f). The plot shows the sudden increase in oscillation amplitude at Vr ≅ 5. This lock-in continues to Vr ≅ 7.

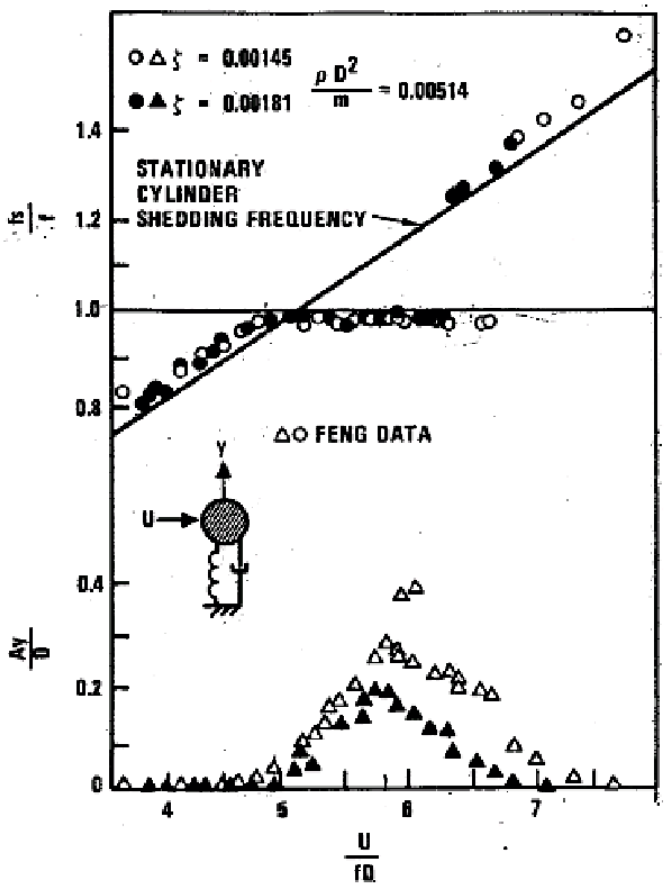

Figure 7: Vortex-induced vibration of a spring-supported, damped circular cylinder (Feng, 1968)

Note that in the figure 7 the abbreviations used are different from the present study and, therefore, the aforementioned explanation also uses the same nomenclature. They are, however, clearly explained and are not expected to cause any confusions.

2.2. VIV Suppression Techniques

Various techniques have been developed to suppress or mitigate the effects of vortex-induced vibrations (VIV) on engineering structures. These VIV suppression techniques can be broadly classified into two categories: active and passive. This section provides an overview of the different VIV suppression methods, including their principles, advantages, and disadvantages.

2.2.1. Active VIV Suppression Techniques

Active VIV suppression techniques involve the use of external energy sources to control or modify the response of the structure to vortex shedding. These methods typically involve sensors, actuators, and control algorithms to monitor and adaptively adjust the structural behavior in real-time. Some examples of active VIV suppression techniques include:

Feedback control: This method uses sensors to measure the vibrations of the structure and actuators to apply forces in response to the measured vibrations, effectively canceling out the VIV forces (Smogeli et al., 2003).

Flow control: This technique involves modifying the flow around the structure to reduce vortex shedding and its associated forces. Examples include the use of synthetic jets, plasma actuators, or piezoelectric devices to manipulate the flow separation and reattachment points (Gad-el-Hak, 2001).

While active techniques can be highly effective in suppressing VIV, they often require complex control systems, are energy-intensive, and can be challenging to implement and maintain, particularly in harsh environments.

2.2.2. Passive VIV Suppression Techniques

Passive VIV suppression techniques do not require external energy sources and rely on the inherent properties of the structure or additional devices to mitigate the effects of vortex shedding. These methods are typically simpler and more robust than active techniques, making them more suitable for a wide range of applications. Some examples of passive VIV suppression techniques include:

Strakes: Helical strakes are spiral-shaped devices mounted on the surface of the structure, disrupting the vortex shedding and reducing VIV (Bearman, 1984). Strakes can be very effective in suppressing VIV, but they may also increase the drag on the structure.

Fairings: Fairings are streamlined coverings that alter the geometry of the structure to minimize vortex shedding and VIV (Sarpkaya, 2004). While fairings can be effective in reducing VIV, they may add significant weight and complexity to the structure.

Surface modifications: Modifications to the surface of the structure, such as dimples, riblets, or grooves, can alter the flow characteristics and reduce VIV (Hao et al., 2022). This approach can be advantageous due to its simplicity and minimal impact on the overall structure.

Figure 8 illustrates a few passive VIV suppression devices including the aforementioned techniques.

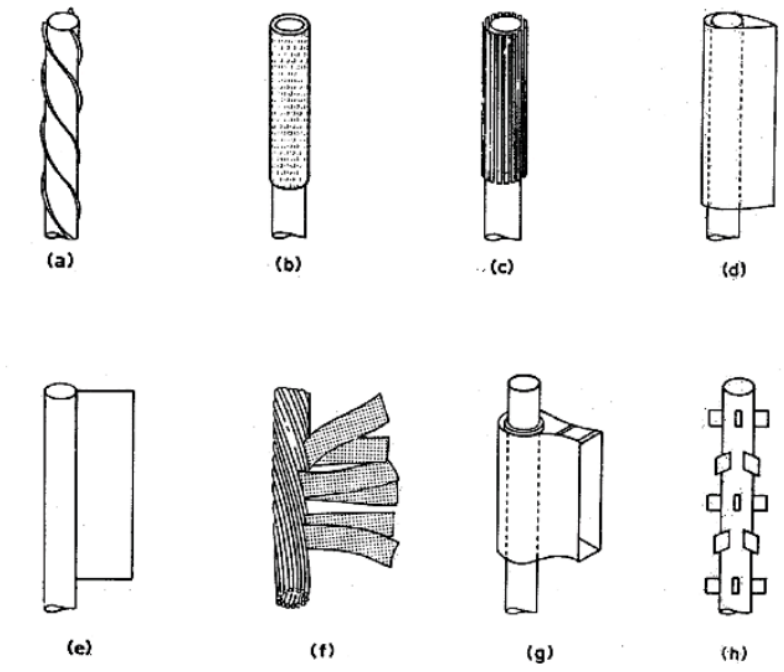

(a) helical strake; (b) shroud; (c) axial slats; (d) streamlined fairing; (e) splitter; (f) ribboned cable; (g) pivoted guiding vane; (h) spoiler plates.

Figure 8: Examples of passive VIV-suppression devices

In conclusion, various VIV suppression techniques, both active and passive, have been developed to mitigate the effects of vortex-induced vibrations on engineering structures. While active techniques can offer precise control and high effectiveness, passive methods are often simpler, more robust, and more suitable for a wide range of applications. The use of staggered grooves as a passive VIV suppression technique will be the focus of this thesis, aiming to optimize their parameters for maximum suppression performance.

2.3. Review of previous studies conducted on VIV of an elastically mounted rigid circular cylinder

(Williamson & Govardhan, 2004) conducted a review of the work done within VIV modelling. The paper stated that the vast majority of numerical models for VIV only allow the cylinder motion in the transverse direction (Facchinetti et al., 2004; Farshidianfar & Zanganeh, 2010; Govardhan & Williamson, 2000; Khalak & Williamson, 1999; Sarpkaya, 1995), and the results from those, being a large part of the domain, make the backbone of the literature accumulated on VIV. However, (Sarpkaya, 1995) concluded from his work that bodies allowed both transverse and in-line degrees of freedom do not exhibit surprising changes in the expected maximum resonant amplitudes compared to bodies allowed to move only in the transverse direction. Additionally, (Williamson & Govardhan, 2004) state that numerical investigations conducted at low Reynolds numbers (for example, by (Blackburn & Karniadakis, 1993; Newman & Karniadakis, 1997)) show that forces are not influenced significantly if the streamwise body motion is also allowed. This means that the results obtained from the majority of the investigations conducted on only-transverse motion bodies, and therefore the general understanding that emerged from the same around VIV, hold. (Williamson & Govardhan, 2004), however, note that significant changes can be observed when comparing the two cases where the mass ratios drop below $m^* = 6$ (Blevins & Coughran, 2009; J. M. Dahl et al., 2006, 2007, 2010; Jauvtis & Williamson, 2004). That is, however, out of scope for the present work as the current setup has $m^* = 31.41$ (chapter 3) and, also, both x and y degrees of freedom are allowed.

Moreover, research conducted by (Tognarelli et al., 2004; Vandiver & Jong, 1987; Wang & Xiao, 2016) have substantiated that in-line vortex-Induced vibrations may inflict equal, if not more, fatigue damage to structures compared to Cross-Flow (CF) VIV, primarily due to the doubled oscillation frequency. As a result, the body of research around 2 Degrees of Freedom (2DOF) VIV

has been steadily expanding, as evidenced by studies from (Bai & Qin, 2014; Kang & Jia, 2013; Srinil et al., 2013; Srinil & Zanganeh, 2012; Wu et al., 2016; Zanganeh & Srinil, 2014).

A considerable portion of the research mentioned comprises experimental studies or semi-empirical models. However, alongside these, there has been a surge of studies focusing on the VIV of an elastically mounted circular cylinder utilising CFD tools. A significant majority of these prior CFD analyses employed 2D models. (Guilmineau & Queutey, 2004) showcased the results of their simulations concerning 1 Degree of Freedom (1DOF) VIV of a circular cylinder. While they successfully captured the response in the initial and lower branches, the upper branch response deviated from experimental findings. (Singh & Mittal, 2005) delved into the hysteresis behaviour of 2 Degrees of Freedom (2DOF) VIV at low Reynolds numbers. They observed hysteresis at both low and high extremes of the lock-in range and notably identified the P + S vortex shedding mode in free vibration for the first time. (Leontini et al., 2006) probed into the branching behaviour of 1DOF VIV at Re = 200. Their numerical investigation unveiled two response branches mirroring the upper and lower branches at higher Re. Both 2D and 3D flow behaviours showed similarities, hinting that the 3D flow branching behaviour could originate from the 2D flow. In another study, (Lucor & Triantafyllou, 2008) conducted a 2D simulation of 2DOF VIV of a circular cylinder across a broad spectrum of in-line to cross-flow natural frequency ratios ($f^* = fn_x/fn_y$). They discovered that the vibration amplitude amplifies, and the peak amplitude transitions to a higher U^* as f^* increases. (Zhao & Cheng, 2011) conducted a simulation of 2DOF VIV of a circular cylinder by solving the 2D Reynolds-averaged Navier-Stokes (RANS) equations. They successfully reproduced the 2T vortex shedding mode and the response in the super-upper branch.

It is well-established that the wake of a circular cylinder transitions to a three-dimensional flow when Reynolds numbers surpass 200 (Williamson, 1988, 1989). A sharp decline in the spanwise correlation of the wake and forces near the mode transition between the upper and lower branches was presented by (Lucor et al., 2005) using direct numerical simulation (DNS) for 1DOF VIV.

On the other hand, (Pontaza & Chen, 2007) applied large eddy simulation (LES) and overset (Chimera) grids to explore 2DOF VIV of a circular cylinder at $U^* = 6$ and $Re = 10^5$. The response showed a figure-eight pattern, and the vortex shedding took on a 2S mode. By utilizing detached eddy simulation (DES), (Saltara et al., 2011) simulated 1DOF VIV of a circular cylinder with a low mass-damping parameter at $Re = 10^4$. While their simulation results aligned with the experimental data of (Khalak & Williamson, 1997), they noted an over-prediction of vibration amplitudes and force coefficients for $U^* > 6$.

A study by (Kondo, 2011) shed light on the different excitation mechanisms in the IL and CF directions using results from a 3D computation, revealing the first and second excited vibrations of the IL direction in the U* range of 1.7 – 3.5. Meanwhile, (Navrose & Mittal, 2013) delved into the transition of responses of 2DOF VIV in the three branches, noting beats in the cylinder responses and force coefficients in the initial branch.

Exploring the transition from 2D to 3D for 1DOF VIV of a circular cylinder, (Zhao & Cheng, 2014) found that the three-dimensionality of the flow was most prominent in the upper branch and weakest in the initial branch. They also discovered the coexistence of 2S and 2P vortex shedding modes in the upper branch. (Gsell et al., 2016) confirmed the large-amplitude VIV and the shape of the responses by simulating 2DOF VIV of a circular cylinder at Re = 3900 with direct numerical simulation of the 3D Navier-Stokes equations, aligning with experimental results from (Jauvtis & Williamson, 2004).

3

Numerical Setup

The numerical setup employed in this study corresponds to the lock-in condition identified in a previous study (Section 1.2), providing a valuable point of reference. A brief summary of the setup is as follows:

The setup is designed to effectively evaluate the impact of different groove configurations by retaining the original conditions used in the previous study to locate the lock-in regime. The initial configuration featured a smooth cylinder elastically mounted on two springs. These springs allowed freedom of motion in both the in-line and cross-flow directions. It's important to note that the stiffness coefficients for both springs were identical, and damping was set to zero, ensuring unrestricted vortex-induced movements. Figure 10 provides a schematic diagram illustrating the elastic mounting for the smooth cylinder case.

As previously mentioned, all grooved cylinders were mounted using the same method. Table 1 lists the parameters defining the setup. This consistency in setup between the smooth cylinder and grooved cylinders aids in a more streamlined comparison and analysis of the results.

Parameter [units]		**Description**	**Value**
D	[m]	Diameter of the 2D cylinder	0.0016
U_∞	[m/s]	Inflow velocity	0.0656
H	[m]	Height of the 2D cylinder	0.12
ν	[m^2/s]	Kinematic viscosity of the fluid	1.05×10^{-6}
Re	[-]	Reynolds number {$Re = U_\infty D/\nu$}	100
$k = k_1 = k_2$	[N/m]	Spring stiffness constant	78.42
m	[kg]	Mass of the cylinder	0.03575
f_n	[Hz]	Natural frequency of the cylinder {$f_n = \sqrt{(k/m)}/2\pi$}	7.4541
U*	[-]	Reduced velocity {$U^* = U_\infty/(f_n D)$}	5.5
ρ	[kg/m^3]	Density of the cylinder	14817
m_f	[kg]	Mass of fluid occupied by the cylinder	4.55×10^{-3}
m*	[-]	Non-dimensional mass {$m^* = m/m_f = 4m/(\rho D^2 H)$}	31.416

Table 1: Values and definitions of parameters used in the numerical setup

Additionally, it's vital to note that certain parameters remain consistent for all cases, smooth and grooved, to ensure a fair comparison. Specifically, the mass of the cylinder (m) and the density (ρ) and therefore the natural frequency (f_n), the reduced velocity (U*), and the non-dimensional mass (m*) are unchanged. Although the grooved cylinders should, in reality, have a reduced volume compared to the smooth cylinder, these parameters remain constant to exclusively study the impact of groove parameters.

In this study, the aim is to isolate the effect of groove configurations; hence, other parameters remain unchanged. This approach ensures that any observed differences in the results can be directly attributed to the groove configurations.

3.1. Governing equations

For this fluid-structure interaction (FSI) problem involving VIV, a set of equations governs the fluid dynamics while another set describes the structural dynamics. A crucial aspect of FSI problems is the coupling between the fluid and the solid: the motion of the solid influences the fluid flow, and reciprocally, the forces exerted by the fluid induce motion in the solid.

This section provides an overview of the governing equations used in this study: the Navier-Stokes equations that dictate the fluid flow, and the equations of motion governing the structural response. The description of how these sets of equations are coupled to simulate the interaction between the fluid and the cylinder is also discussed.

3.1.1. Fluid Modelling

The computational model of the fluid flow is based on the incompressible Navier-Stokes equations, which are the fundamental partial differential equations for describing the motion of fluids. These equations, derived from the basic principles of conservation of mass (continuity equation) and momentum, are applicable to laminar flows considered in the present study.

The continuity equation, expressing the conservation of mass, can be written as:

$$\frac{\partial U}{\partial x} = 0 \qquad \textit{(equation 6)}$$

The conservation of momentum can be written in the following vector form:

$$\rho\left(\frac{\partial U}{\partial t} + (U \bullet \nabla) U\right) = -\nabla p + \mu \nabla^2 U \qquad \textit{(equation 7)}$$

Where U is the fluid velocity, p denotes the pressure, μ is the dynamic viscosity of the fluid, and t represents time. The term on the left-hand side of the equation signifies the inertial forces, whereas the terms on the right represent the pressure forces and viscous forces, respectively.

For this work, since the problem here deals with laminar flows, the turbulence terms are absent from the equations.

3.1.1.2. Arbitrary Lagrangian-Eulerian (ALE) Method

The modelling of fluid-structure interactions around a moving body requires a special approach due to the mesh deformation induced by the motion.

The Arbitrary Lagrangian-Eulerian (ALE) method is used to describe the movement of the fluid and the solid body. This method allows the fluid domain (grid) to deform according to the motion of the body (Lagrangian approach), while still solving the fluid equations relative to this deforming grid (Eulerian approach) (Donea et al., 1982).

In the ALE formulation, the Navier-Stokes equations take on a modified form that accounts for the relative motion between the grid and the fluid. The continuity equation and the convective term in the momentum equation are modified to include a grid velocity component (W). The modified Navier-Stokes equation, therefore, become:

$$\frac{\partial(U-W)}{\partial x}=0 \qquad \textit{(equation 8)}$$

$$\rho\left(\frac{\partial U}{\partial t}+((U-W)\bullet\nabla)U\right)=-\nabla p+\mu\nabla^2 U \qquad \textit{(equation 9)}$$

This adjustment allows the morphing mesh to follow the movement of the fluid-structure system accurately, ensuring a high-quality solution for the flow around the deforming cylinder.

3.1.2. Rigid body motion solver

The motion of a rigid body, when attached to a spring mass damper system and immersed in a fluid flow field, is governed by the following equation:

$$m\ddot{x}_s = d\dot{x}_s + kx_s + \oint n\,p dS + \oint n.\tau_{vis}\,dS \qquad \textit{(equation 10)}$$

where *m*, *k* and *d* represent the mass of the solid, the spring constant, and the damping constant respectively in a spring-mass system. The additional two terms are added to include the effects of the fluid forces on the motion of the solid. Here τ_{vis}, represents the viscous stress tensor.

Equation 10 is integrated using the Symplectic integration scheme which is a 2nd order explicit time-integrator for 6 degrees of freedom solid-body motion.

3.1.3. Fluid-Structure Interaction model

In the present study, a partitioned approach is applied to model the fluid-structure interaction (FSI). This involves alternating between the fluid field and the structural system at each timestep. The partitioned approach is preferred over the monolithic approach due to its flexibility in accommodating a wide range of FSI scenarios. Additionally, the monolithic approach may be computationally expensive due to the need to solve fluid and structural systems simultaneously.

Partitioned algorithms are classified into explicit, semi-explicit, and implicit categories based on their coupling strategies. In the present FSI model, both explicit and implicit FSI schemes are utilised as Pimplefoam has the capability to work with both.

3.1.3.1. Fluid-Structure Interaction Scheme

The following block diagram illustrates the solver, which is based on the Pimplefoam solver used within the OpenFOAM CFD package (Devolder et al., 2015):

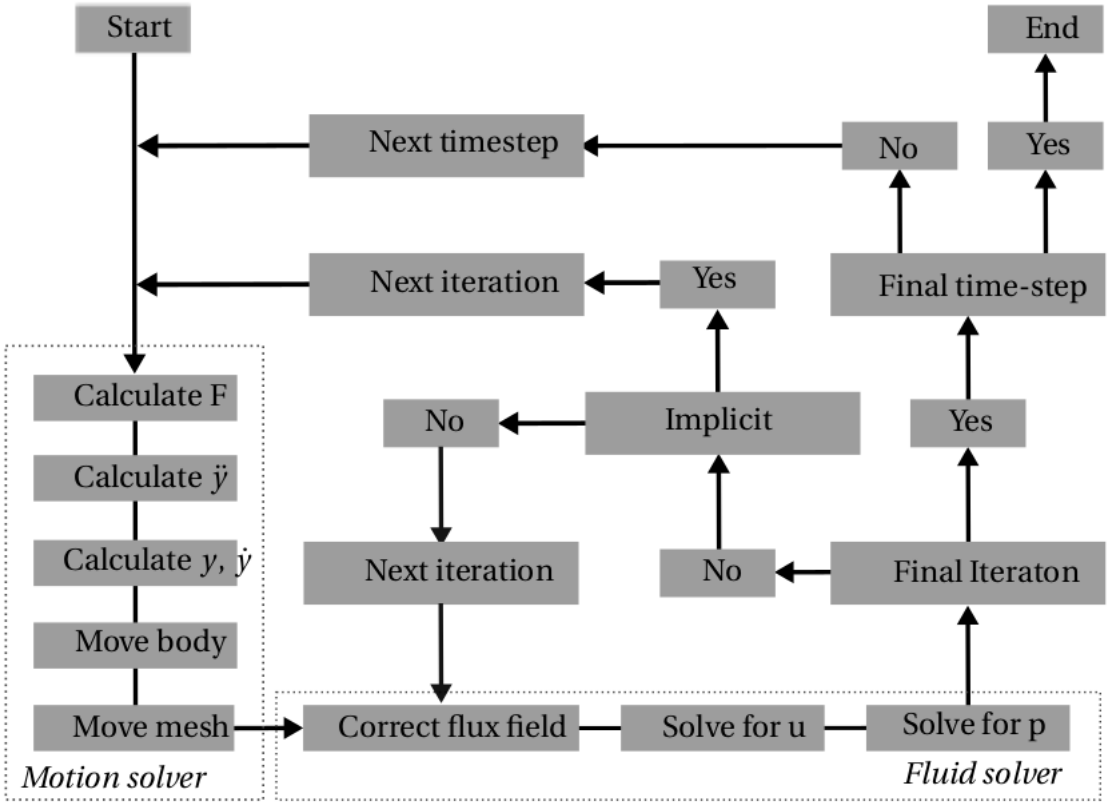

Figure 9: Block diagram for Pimplefoam solver

At the beginning of each timestep, the structural motion is solved first. Upon obtaining the displacement value from the motion solver, the geometry is moved accordingly. The new dynamic mesh is then evaluated, with the new position of the body imposed as a boundary condition. OpenFOAM ensures no mass flows through the solid structure, enforcing a relative fluid velocity of zero at the solid wall. The mesh diffusion is then calculated based on the SLERP (Spherical Linear intERPolation) interpolation (Shoemake, 1985), which takes into account the motion of the structure. With the newly computed mesh velocity field, the Navier-Stokes equations are modified using the Arbitrary Lagrangian-Eulerian (ALE) formulation, handling the mesh motion. The velocity and pressure are then solved.

If the final iteration has not been reached, the behaviour of the next iteration depends on the FSI scheme in use. For the weakly-coupled scheme, the fluid solver reuses the same modification of Navier-Stokes equations from the previous iteration. The motion is only solved once per timestep, and the mesh only moves once in each timestep. In contrast, the strongly-coupled scheme starts the next iteration with the motion solver again. This results in the motion being solved and the mesh moving multiple times within a single timestep. These iterations are referred to as sub-iterations.

Both weakly-coupled and strongly-coupled solvers repeat this process until the final PIMPLE iteration is reached, after which the complete solver reruns for each timestep until the simulation concludes.

3.2. Domain

In the context of this investigation involving a FSI analysis around grooved cylinders in the lock-in regime, computational domain size selection becomes a crucial task. The lock-in condition is characterized by enhanced wake interaction which necessitates a more careful domain size selection. These flow phenomena significantly influence the structural responses and the overall dynamics of the system, emphasizing the importance of an appropriately defined computational domain.

In this investigation, the computational domain is defined as a rectangular region. The circular cylinder is positioned such that the upstream, top, and bottom boundaries lie at a distance of 20D from the cylinder, while the downstream boundary is situated 40D away from the cylinder's center (figure 10).

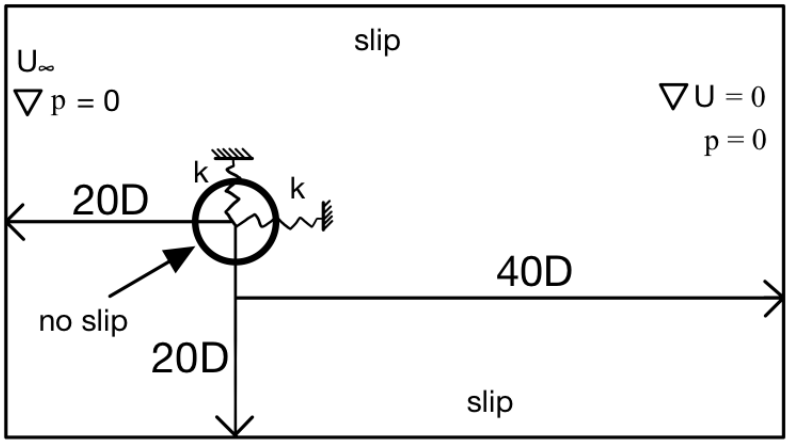

Figure 10: The numerical setup of the FSI model

This domain size has been chosen to ensure an accurate representation of the flow characteristics while minimizing computational needs due to domain truncation. The downstream boundary is set

further away to provide ample space for the development and evolution of the wake, which typically extends a significant distance downstream from the cylinder.

The choice of domain dimensions is backed up by prior research in the field. (Prasanth & Mittal, 2008) conducted a study on the vortex-induced vibrations of a circular cylinder at low Reynolds numbers using a similar blockage ratio. The researchers found these dimensions adequate for capturing the important flow features without noticeable influence from the domain boundaries. The aforementioned study also demonstrated that this domain size offers a balance between reliability and computational efficiency. Smaller domain sizes may result in artificial feedback from the boundaries, leading to inaccurate predictions of the flow dynamics.

Consequently, the domain size chosen for this study is not only a strategic decision aimed at optimizing computational efficiency but is also supported by empirical evidence from previous research. It ensures the flow field is adequately resolved while keeping the required computational resources and time for the simulations to a minimum.

Moreover, this domain configuration is not just suitable for the case of a smooth circular cylinder but is also expected to be appropriate for the grooved cylinder configurations under investigation. The core flow physics and vortex shedding mechanisms in the wake of a grooved cylinder do not deviate drastically from those of a circular cylinder. In summary, the chosen domain size for the present study, based on the review of the previous work and the nature of the flow physics involved, is expected to provide accurate results for the cases of both circular and grooved cylinders.

3.3. Meshing

In this study, a structured meshing approach is adopted to discretize the computational domain for the numerical simulations. The use of structured meshes is justified by several factors that are important to the specific characteristics of the problem at hand.

Firstly, structured meshes offer superior control over the mesh distribution, which is critical in accurately capturing the flow characteristics around the grooved cylinder, especially around the grooves themselves. The ability to enforce fine resolution in regions of interest, such as near walls or in areas of high flow gradients, ensures a higher fidelity representation of the flow physics.

Furthermore, structured meshes offer advantages in terms of computational efficiency. Given their regularity and simpler topology, calculations involving geometric properties and spatial derivatives become more straightforward, reducing computational overhead and thus leading to faster simulations (Versteeg & Malalasekera, 2007).

However, it's important to note that the generation of a structured mesh can be more time-consuming and challenging, particularly for complex geometries. In this case, the geometry of the grooved cylinder has been carefully designed to ensure a high-quality structured mesh could be generated with relative ease. The resultant mesh quality, in terms of aspect ratio, skewness, and orthogonality, meets the recommended standards for the employed numerical schemes.

Overall, the choice of a structured mesh aligns well with the demands of this study, providing an appropriate balance between numerical accuracy, computational efficiency, and the need to adequately represent the problem's geometry.

Additionally, as already mentioned in the previous sections, a morphing mesh technique is utilized to track the motion of the cylinder geometry and re-adjust at every timestep.

3.4. Boundary conditions

The implementation of boundary conditions is a critical step in the numerical modelling of any CFD problem. The prescribed boundary conditions in this study are chosen as to accurately simulate the physical characteristics of the fluid flow around the cylinder.

Table 2 provides an overview of the applied boundary conditions on the numerical domain.

Boundary	**Velocity**	**Pressure**
Inlet	$u = U_\infty$, $v = 0$	$\partial p/\partial x = 0$, $\partial p/\partial y = 0$
Outlet	$\partial u/\partial x = 0$, $\partial v/\partial x = 0$, $\partial u/\partial y = 0$, $\partial v/\partial x = 0$	$p = 0$
Cylinder	$u = 0$, $v = 0$	$\partial p/\partial x = 0$, $\partial p/\partial y = 0$
Top and bottom	$\partial u/\partial y = 0$, $v = 0$	$\partial p/\partial x = 0$, $\partial p/\partial y = 0$
Front and back	*Empty*	*Empty*

Table 2: Summary of applied boundary conditions

The 'Inlet' boundary is characterized by a uniform velocity field and a zero pressure gradient, ensuring a consistent inflow into the computational domain. The 'Outlet' boundary is set to zero pressure and zero velocity gradient, aiming to reduce any artificial influence on the exiting flow. For the 'Top' and 'Bottom' boundaries, a slip condition allows for an undisturbed flow along these edges, reducing the influence of these far field boundaries on the flow around the cylinder. The 'Cylinder' surface, as the primary area of interest, is assigned a “no-slip” condition to account for the viscous nature of the fluid at the solid boundary. Given the two-dimensionality of the problem, the 'Front' and 'Back' boundaries are treated with an “empty” condition, simplifying the computational requirements and showcasing the axisymmetric nature of the problem.

The physical conditions are translated into OpenFOAM by assigning specific boundary types. 'Patch' is used for inflow, outflow, and top and bottom boundaries, while the cylinder surface is defined as 'wall'. The front and back boundaries, due to their symmetric nature, are defined as 'empty'.

3.5. Grooved Cylinders

In this study, several grooved cylinder geometries are examined and their results are compared with those of the smooth cylinder obtained during the previous study (section 1.2). The grooves are of staggered type and symmetric along the x-axis. Therefore, for all the configurations, except the “p180” cases (groove at the front of the cylinder, see figure 10) there are two symmetric staggered grooves. To showcase an example, figure 9 shows a grooved cylinder configuration at 90° to the flow with width 15° and depth 0.075D (see section 3.5.1). Figure 10 illustrates a grooved cylinder with a single groove at 180°.

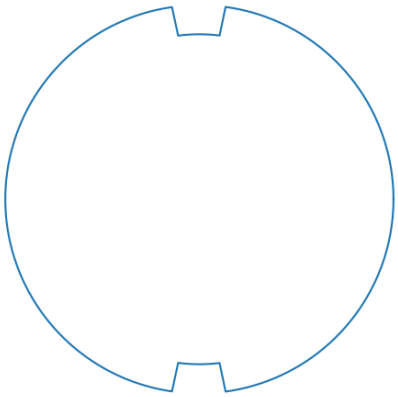

Figure 11 p90w15d0.075 case

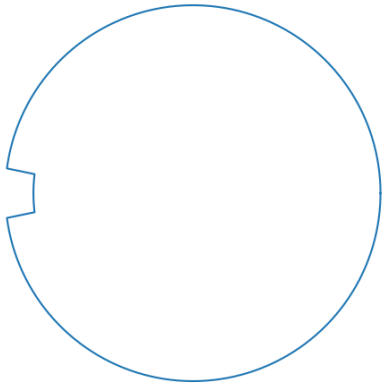

Figure 10: p180w15d0.075

A total of 36 grooved-cylinders are investigated where the groove position, width and depth are the parameters that are varied to achieve unique geometries. Each configuration is illustrated in sections 9.3 and 9.4.

3.5.1. Nomenclature of cases

Given the large number of grooved cylinder geometries studied, a straightforward naming scheme is used for clear identification of these cases.

Each grooved cylinder geometry is described by three main parameters: the Position (p) of the grooves on the cylinder, the Width (w) of the grooves, and the Depth (d) of the grooves. These parameters are the basis of the naming scheme, making it easier to distinguish between the different geometries.

The position (p) is defined as the point on the cylinder surface from which if a line is drawn through the center, it would make the angle of p degrees (°) with the incoming flow in the anti-clockwise direction. Figure 12 shows the values of p used in the present investigation. The depth (d) of the groove is simply defined as the total depth of the groove as a function of the cylinder diameter (D = 0.0016m). Therefore, for example, a groove depth of 0.1D means that the groove's actual depth is 0.1 x 0.0016 = 0.00016 m. Additionally, the width of the groove (w) is defined as the total angular

width of the groove in degrees (°). Figure 13 illustrates the definition of the groove depth (d) and width (w) at a 90° symmetric grooves position.

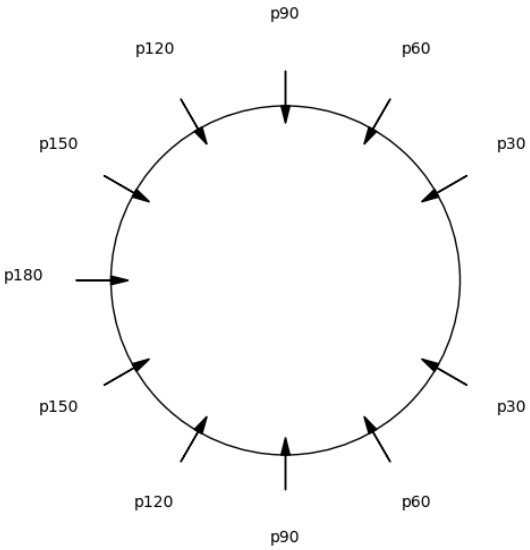

Figure 12: Definition of groove positions

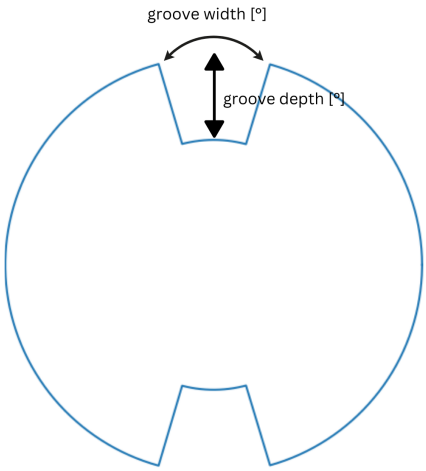

Figure 13: Definition of groove width and depth

The naming scheme follows the format pxwydz, where 'x', 'y', and 'z' represent the values for the groove position, width, and depth, respectively. For example, the name p60w15d0.075 refers to a grooved cylinder where the grooves are located at an angular position of 60°, have a width of 15°, and a depth of 0.075 times the cylinder diameter, i.e. 0.075D (see figure 14).

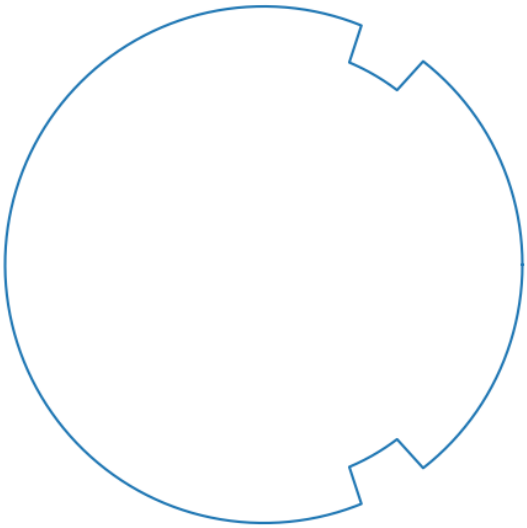

Figure 14: p60w15d0.075 case

This clear and simple naming scheme is designed to make it easier for readers to understand the various grooved cylinder geometries discussed throughout this thesis.

4

Validation study

Currently, there are no precise analytical solutions that can define the fluid dynamics around a stationary cylinder accurately. However, benchmarking against existing CFD studies in the literature serves as a viable alternative to demonstrate the efficacy of the current CFD model. Notably, a lot of CFD studies simulating VIV in a low Re regime (corresponding to laminar flow) are available in the literature. Given the validated results of an elastically mounted smooth 2D cylinder from a preceding study (see section 1.2) against (Alletto, 2022; Singh & Mittal, 2005), coupled with the existing research gap in the field of elastically mounted 2D cylinders with staggered grooves at low Reynolds numbers, there is a compelling case to explore the unique effects induced by a groove.

Therefore, to provide a benchmark for the current model, the study by (Priyadarsan & Afzal, 2023), which investigated a fixed rigid 2D circular cylinder with a single square groove, has been selected. Even though this study does not involve displacement due to VIV or consequently, mesh morphing, it remains a crucial step in the validation process. It is worth noting that the research focus of this thesis is on elastically mounted 2D circular cylinders with grooves operating in a laminar regime characterized by low Reynolds numbers. However, owing to the lack of directly comparable studies in the literature, a precise validation and verification of the developed model requires creative approaches.

In the study by (Priyadarsan & Afzal, 2023), a single square groove is located on a 2D circular cylinder at a 90° position, perpendicular to the inlet flow velocity (see figure 15). Both the width

and the depth of the groove are set to be equal to 0.1D where D is the diameter of the circular cylinder. The flow is subjected to an uniform flow of Re = 100.

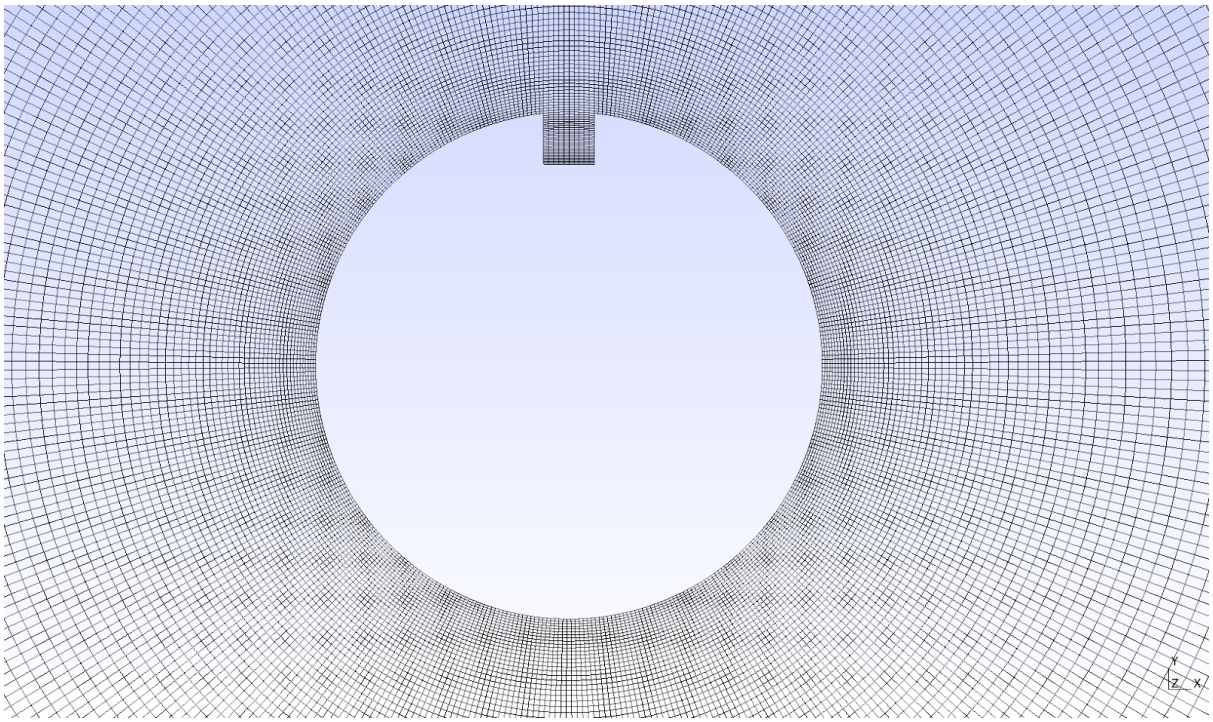

Figure 15: Mesh constructed for the validation study: zoomed at the cylinder

	(Priyadarsan & Afzal, 2023)	Present study	**Relative error [%]**
St	0.163	0.162	**-0.6135**
$C_{D,avg}$	1.3222	1.3229	**0.0529**
$C_{L,rms}$	0.2235	0.2213	**-0.9843**

Table 3: Results and comparison from the validation study

Table 3 illustrates the lift and drag coefficients and the comparison between the study conducted by (Priyadarsan & Afzal, 2023) and the present study. As can be seen, the results from the present study show very good agreement with the reference study, showing a deviation of only around 0.05% for $C_{D,avg}$ and around 0.98% for $C_{L,rms}$.

5

Results

5.1. Convergence studies

5.1.1. Mesh convergence study

The mesh convergence study has been performed for mesh ranging from 30 000 to 105 000 cells. Figures 16 through 21 show the different mesh refinements with varying densities around one of the grooved cylinders (p90w10d0.05 case), along with corresponding zoomed views to showcase the mesh around the grooves and the boundary layer. Note that similar mesh has been created for other grooved-cylinder configurations too. Table 4 shows the relative error for the different field parameters obtained from the study to the subsequently finer version of the mesh. The exact values for the result parameters for these three meshes are tabulated in Table 4.

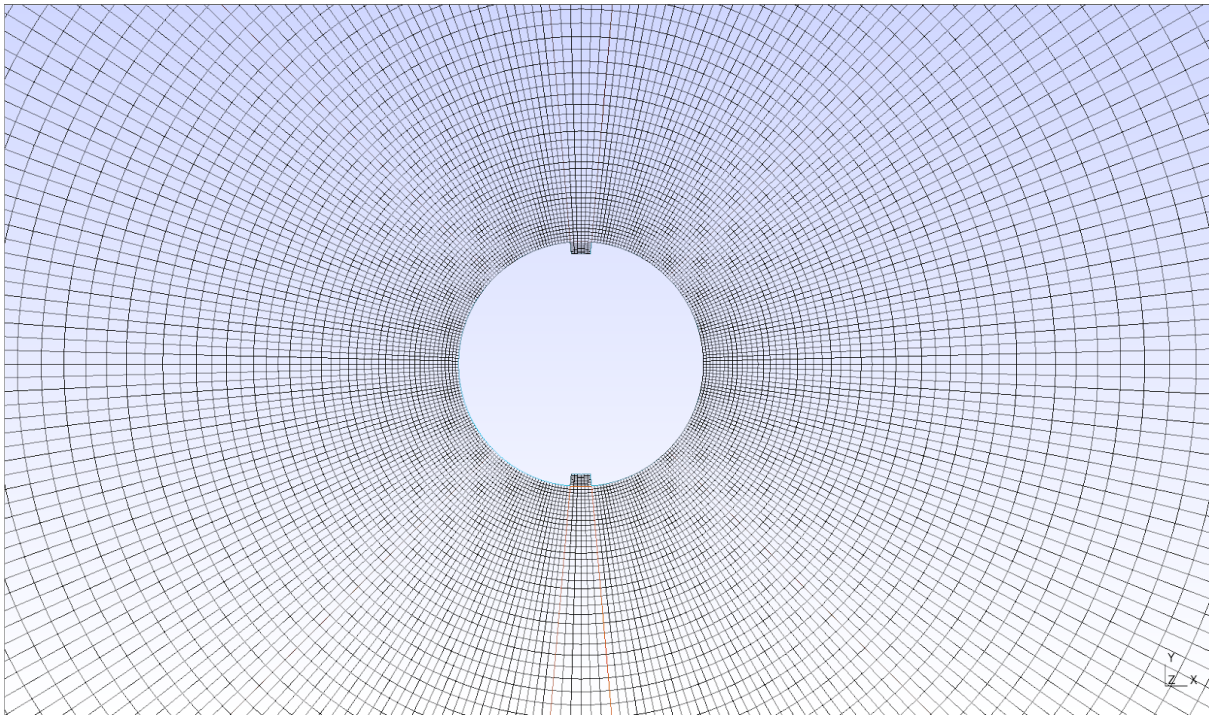

Figure 16: Mesh with 30 000 cells

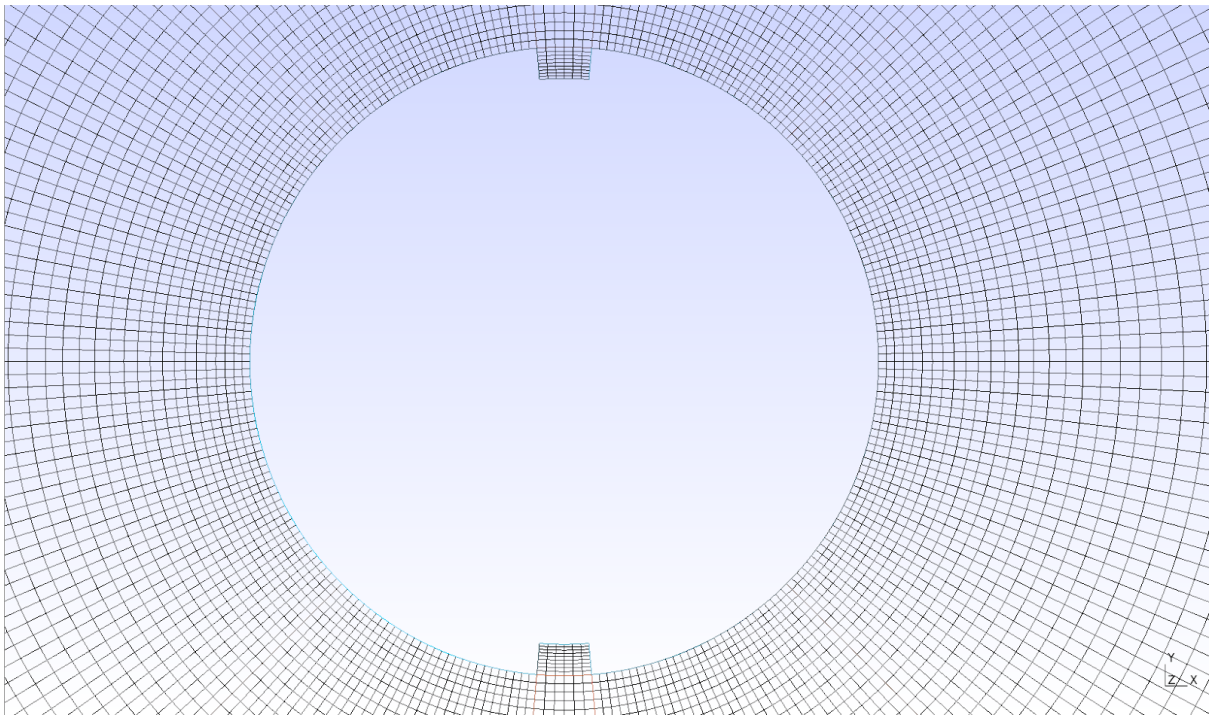

Figure 17: Mesh with 30 000 cells; zoomed version

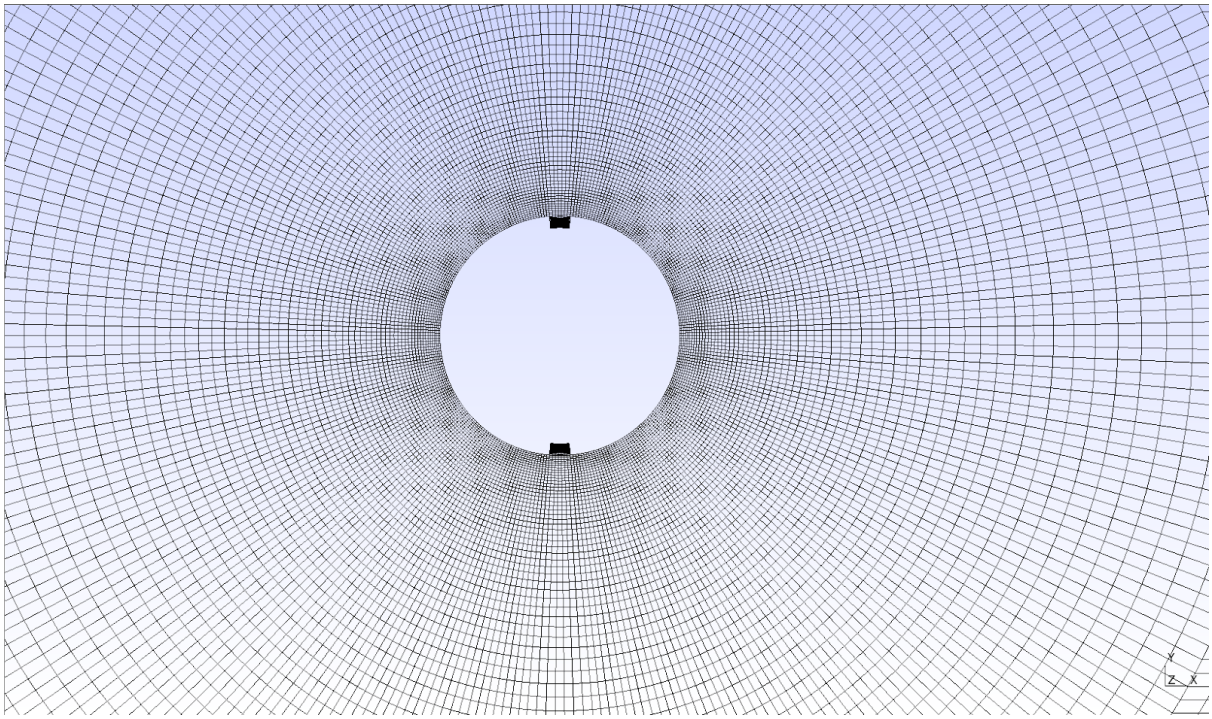

Figure 18: Mesh with 39 000 cells

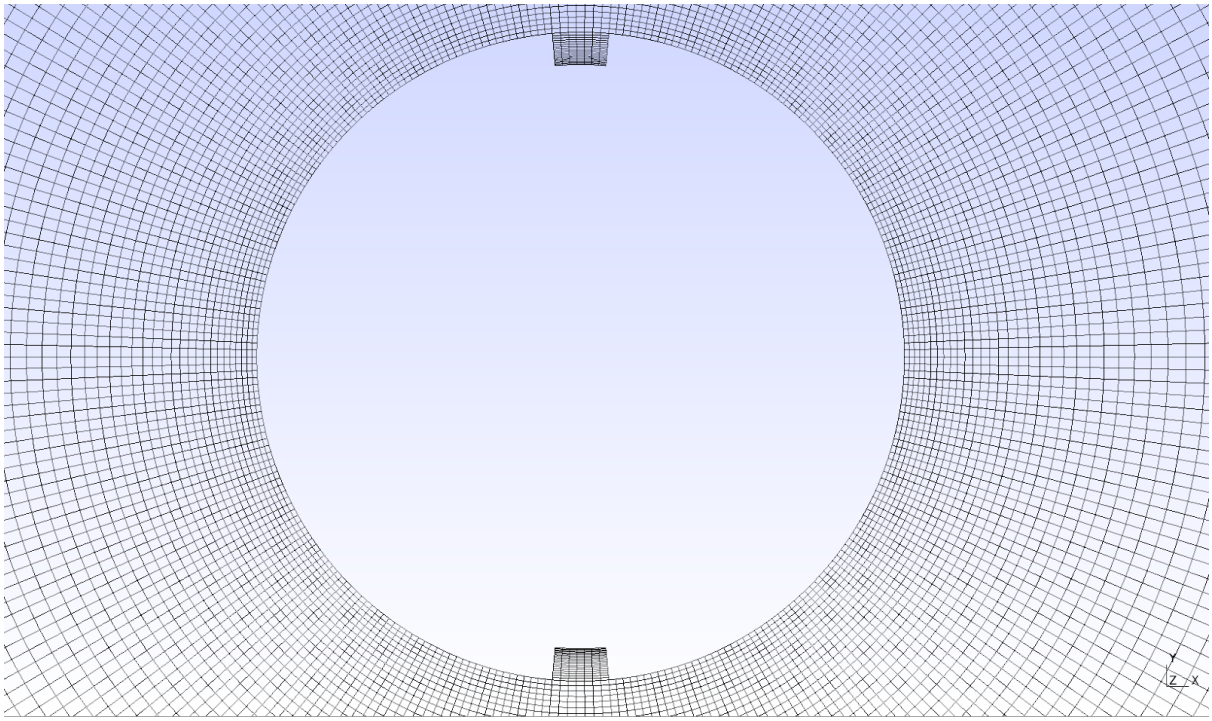

Figure 19: Mesh with 39 000 cells; zoomed version

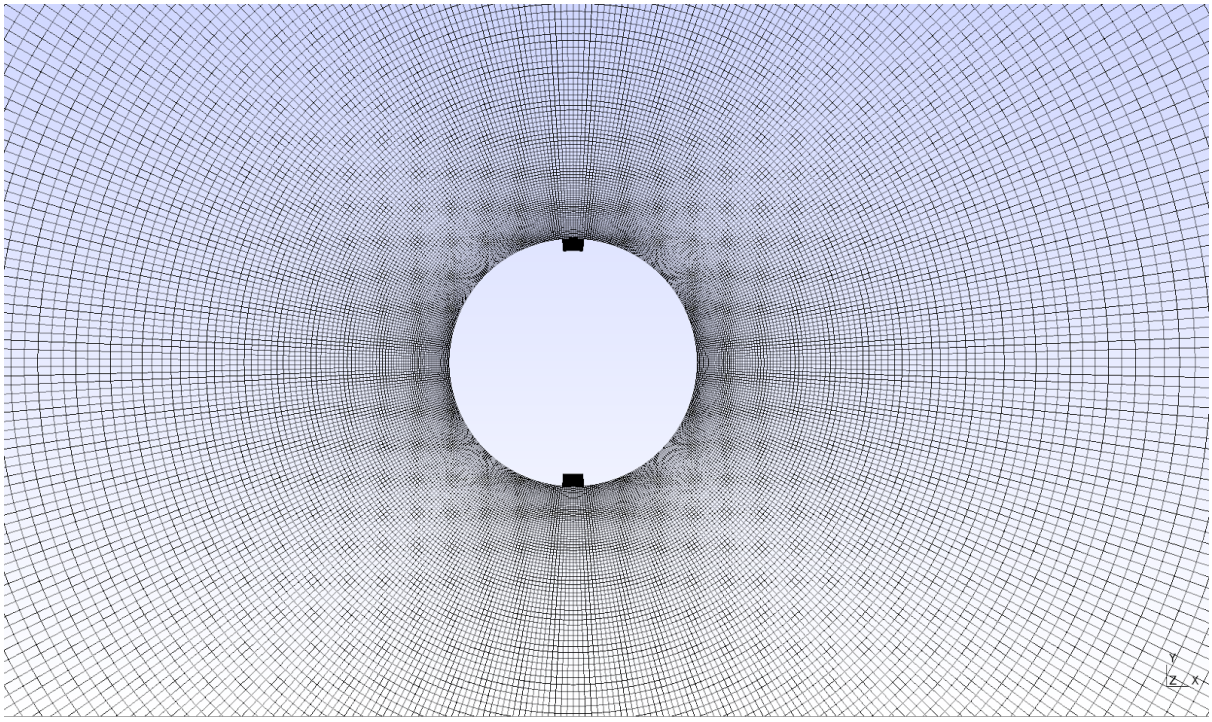

Figure 20: Mesh with 105 000 cells

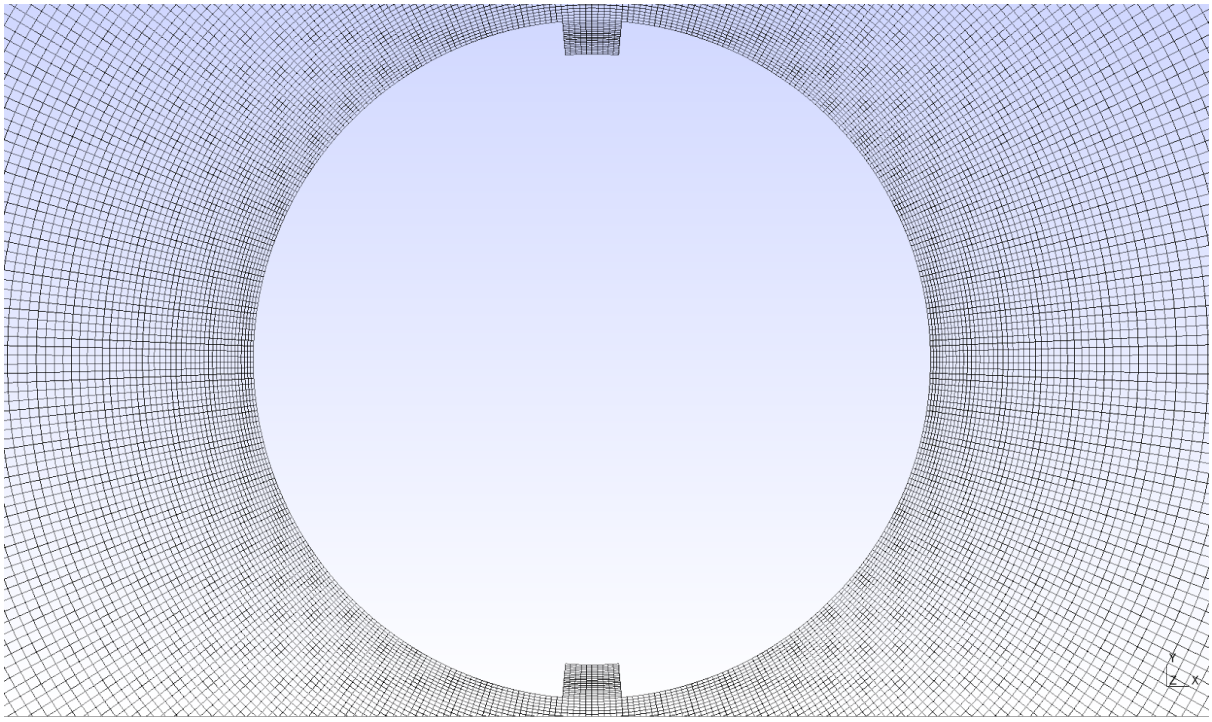

Figure 21: Mesh with 105 000 cells; zoomed version

Mesh	y_{max}/D [%]	x_{rms}/D [%]	$C_{D,rms}$ [%]	$C_{L,rms}$ [%]
105 000 cells	-	-	-	-
39 000 cells	0.2201	-0.0356	2.3307	-0.1311
30 000 cells	-0.6296	-1.2830	-1.7050	-1.3249

Table 4: Relative error values from the mesh convergence study

It is evident from the results presented in Table 4 that the mesh consisting of 30 000 cells results in values with sufficient accuracy. Therefore, this mesh is used for further investigation of the grooved-cylinders.

5.1.2. Temporal refinement study

In addition to the grid refinement study, a temporal refinement study is conducted to assess the impact of the timestep size on the accuracy of the solution. This investigation is done using the 30 000 cells mesh. As with the spatial discretization, temporal discretization can introduce errors into the numerical simulation. Therefore, it's important to ensure that the chosen time step size is small enough to accurately capture the temporal evolution of the flow, but not so small as to make the simulation computationally prohibitive.

For this study, an adjustable timestep scheme is deployed. This scheme alters the timestep size dynamically in response to local flow conditions, thereby ensuring the maximum Courant number (Co_{max}) remains within specified boundaries.

In a previous investigation of the smooth cylinder case, a Co_{max} of 0.75 was established after a similar temporal refinement study. The temporal refinement study for grooved cylinders was, therefore, initially started with this value of $Co_{max} = 0.75$. However, the solution exhibited notable numerical instabilities, as illustrated by Figure 22 which displays the lift force for the p90w10d0.05 case. By decreasing the Co_{max} to 0.5, these instabilities were eradicated, resulting in a stable solution.

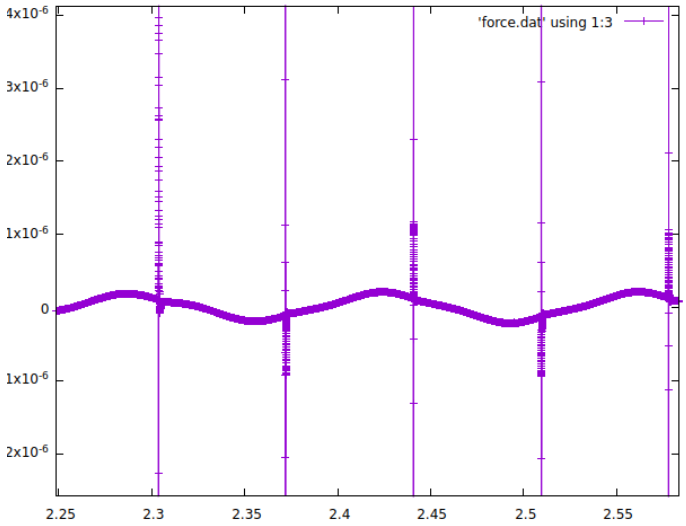

Figure 22: Peaks observed in the lift force plot against time - zoomed version

It is likely that the solver was unable to capture the amplified dynamics around the groove regions with a Co_{max} = 0.75. This is particularly pertinent for the case used in this investigation (grooves positioned at 90°), given that the separation point was found to be near that position in the smooth cylinder case (section 9.2).

A further decrease in the Co_{max} to 0.2 was investigated and compared to the 0.5 case. The differences in the results are summarized in Table 5.

	Co_{max} = 0.2 [%]	**Co_{max} = 0.5 [%]**
y_{max}/D [-]	-	0.1540
x_{rms}/D [-]	-	0.0614
$C_{D,rms}$ [-]	-	0.0337
$C_{L,rms}$ [-]	-	0.5770

Table 5: Relative error in temporal convergence study

Given that the discrepancies are less than 1%, the subsequent simulations in this study utilized a Co_{max} = 0.5. While the instability at Co_{max} = 0.75 may or may not have been observed at other groove positions, it was particularly evident at the 90° and 60° positions due to the complex flow dynamics. Thus, it was of utmost importance to choose a Co_{max} that was sufficiently low to provide stable solutions for these challenging cases. By setting the Co_{max} = 0.5, stable and accurate solutions were obtained for all grooved-cylinder scenarios.

5.2. Analysis of the smooth cylinder case

Before the discussion of results for the grooved-cylinder cases is presented, it can be worthwhile to present a brief analysis of the flow around the smooth cylinder that was investigated during a previous study (section 1.2). This review serves as a foundation, providing the necessary context to more effectively comprehend the modifications in flow dynamics and cylinder responses when transitioning from smooth to various grooved-cylinder configurations.

In Figure 23, the vorticity contours for one cycle of the cross-flow oscillation for the smooth cylinder are shown at progressing time instances where T is the time-period of the oscillation[1]. Attention is particularly paid to the areas of low vorticity around the cylinder's edge because these mark the separation points. Pinpointing the exact separation points on the top and bottom of the moving cylinder is more challenging compared to a stationary one, but the regions of low vorticity around the cylinder's edges are key.

1 Note that the colour scheme of the vorticity contours is inverted here compared to that of the grooved cylinders discussed in chapter 5. This because of inconsistency in the coordinate system between the two cases.

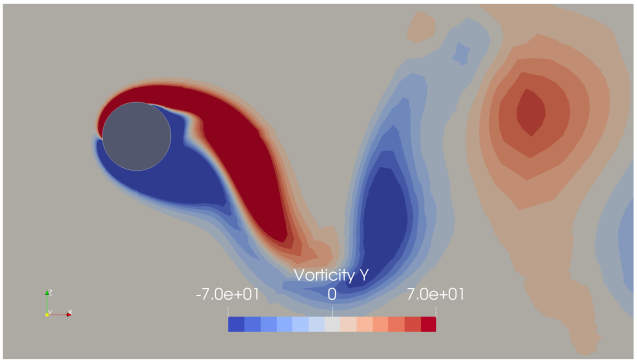

a) t = T/10

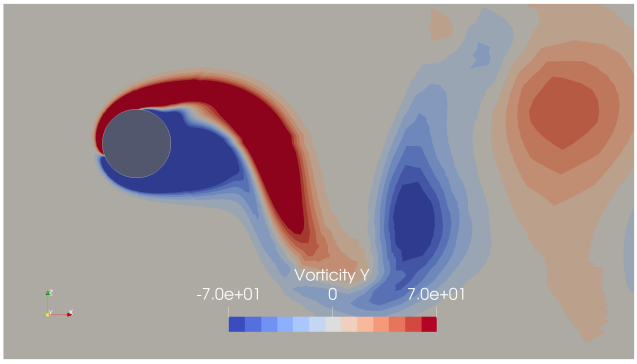

b) t = 2T/10

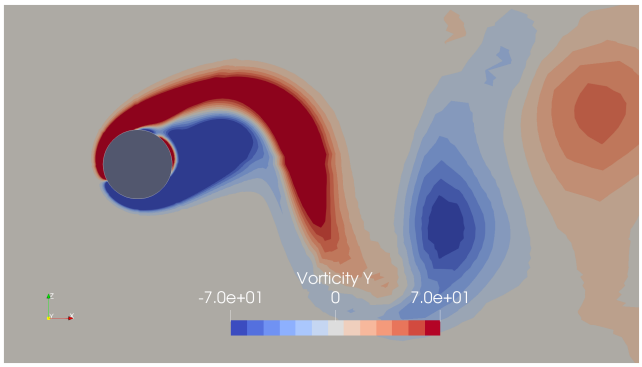

c) t = 3T/10

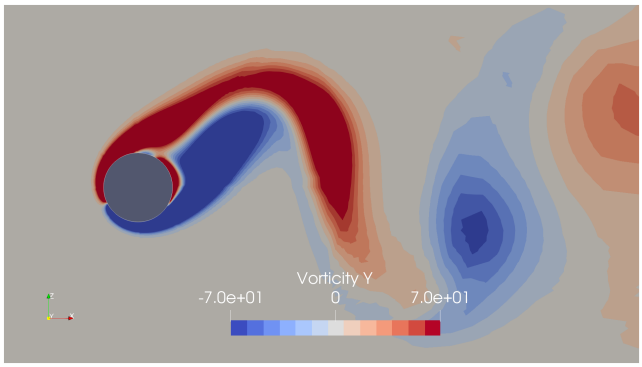

d) t = 4T/10

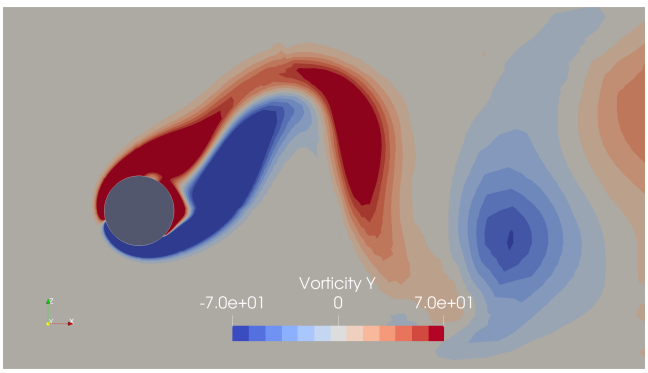

e) t = 5T/10

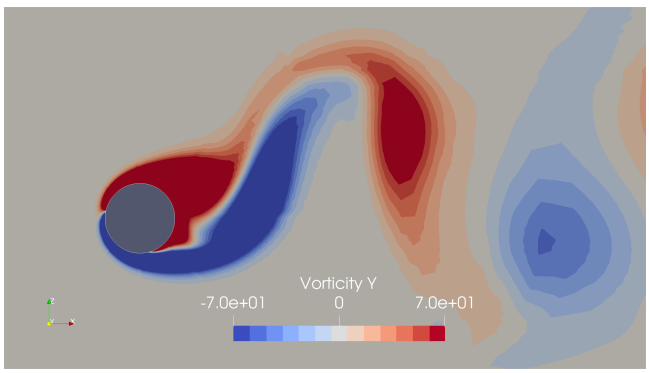

f) t = 6T/10

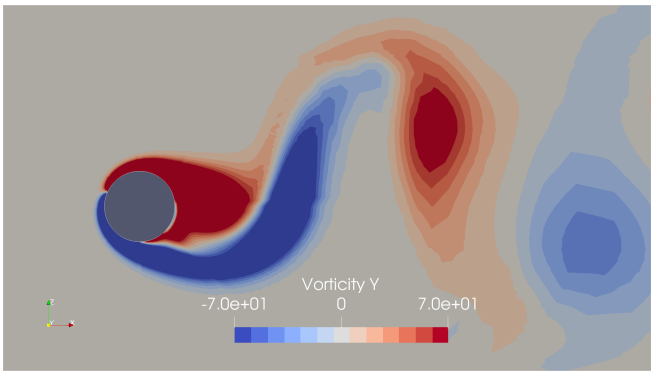

g) t = 7T/10

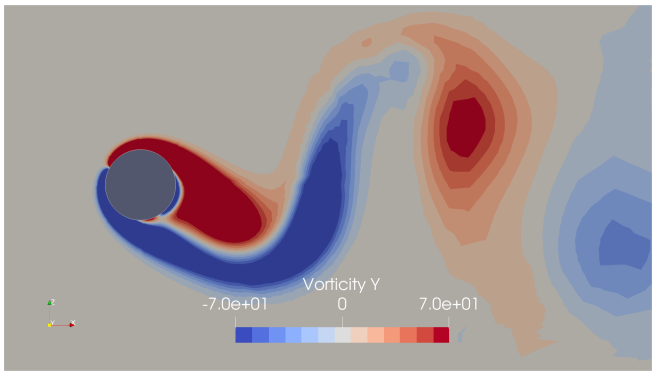

h) t = 8T/10

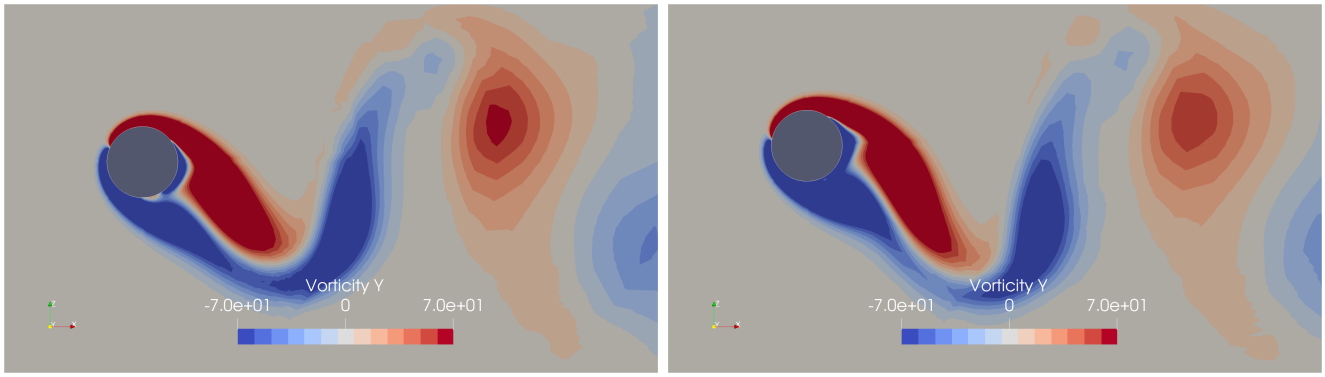

i) t = 9T/10 j) t = T

Figure 23: vorticity contours at progressing time instances around the cylinder

When the cylinder is at the highest point of the oscillation, a low vorticity area can be seen close to 90° from the incoming flow at the top of the cylinder. The vorticity before that area (upstream) on the top half is towards the opposite direction as in the downstream. This change in vorticity direction supports the idea that the low vorticity area is indeed the separation point.

As the cylinder begins to move down, a small region of positive vorticity forms near the rear of the cylinder's top half. This area is enclosed on one side by the cylinder's surface and on the other side by a region of negative vorticity. Importantly, this positive vorticity area appears where the negative vorticity region meets the surface of the cylinder. Due to the change in vorticity direction, a thin layer of low vorticity forms at the boundary between the negative and positive vorticity areas, extending to the cylinder surface on either side.

With further downward movement, this positive-vorticity area expands and pushes the adjacent low-vorticity areas apart until it combines with the low-vorticity area on the top of the cylinder, resulting in the disappearance of that low-vorticity region. At the same time, the low-vorticity area that moves down to the bottom half of the cylinder up to the cylinder's circumference at about -60° position ('-' indicates the position is on the bottom half of the cylinder). This low-vorticity area keeps moving down until it lands at around a -90° position when the cylinder is at its lowest point. As the cylinder starts moving up, the same dynamics occur again, just in the opposite direction.

This observation of the smooth cylinder case is a major reason for the special focus on the 90° and 60° groove-positions when analyzing different groove configurations, as discussed in section 9.4.

5.3. Cases investigated

The initial cases that have been run and investigated involve symmetric grooves located at angular positions ranging from 30° to 150° (see figure 12), in intervals of 30°. Additionally, a case where a single groove is positioned at 180°, i.e, where the inflow first interacts with the cylinder, has been run and investigated. In all instances, the groove width (w) remained a constant 10°, while the depth of the grooves (d) was systematically altered between 0.05D, 0.075D, and 0.1D. Here, 'D' denotes the diameter of the 2D circular cylinder under consideration. Therefore, the total number of these initial cases that are run and analysed is 6 positions x 3 depths x 1 depth = 18 cases.

A series of visualizations illustrating the cylinder geometries for the preliminary cases are presented in figures 24: a to r. Each figure corresponds to a unique combination of groove placement and depth, clearly showcasing the variations under study.

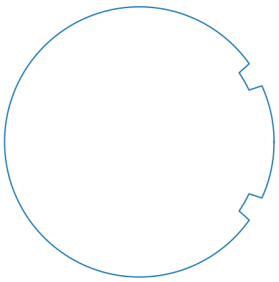

a) p30w10d0.05

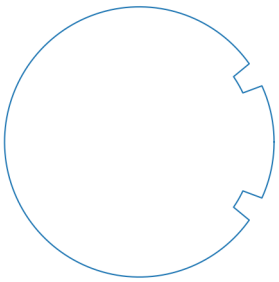

b) p30w10d0.075

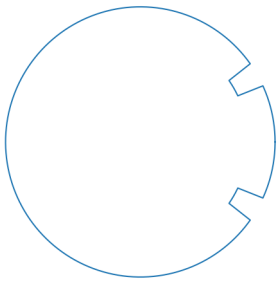

c) p30w10d0.1

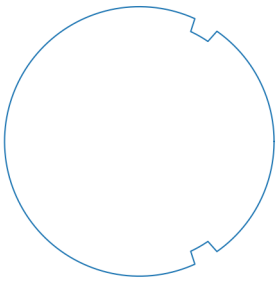

d) p60w10d0.05

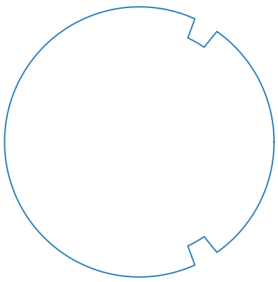

e) p60w10d0.075

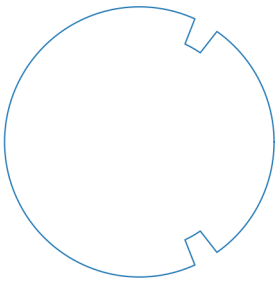

f) p60w10d0.1

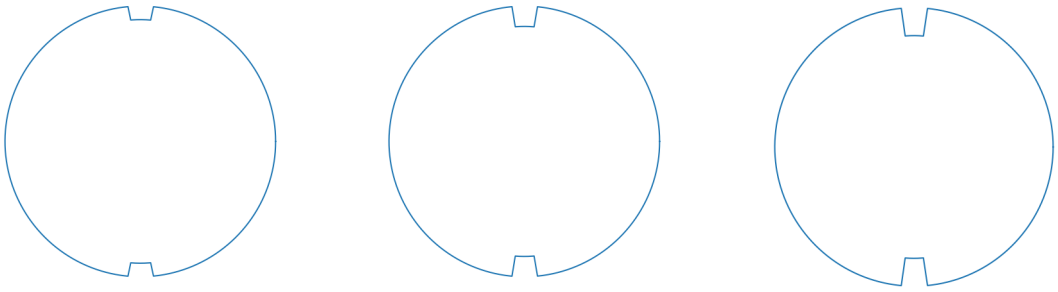

g) p90w10d0.05 h) p90w10d0.075 i) p90w10d0.1

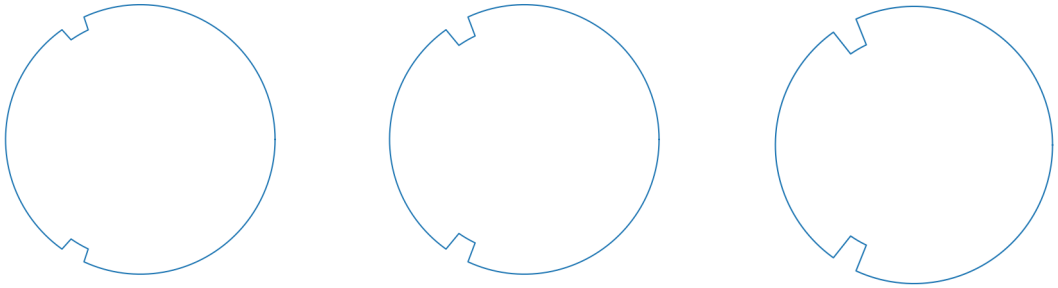

j) p120w10d0.05 k) p120w10d0.075 l) p120w10d0.1

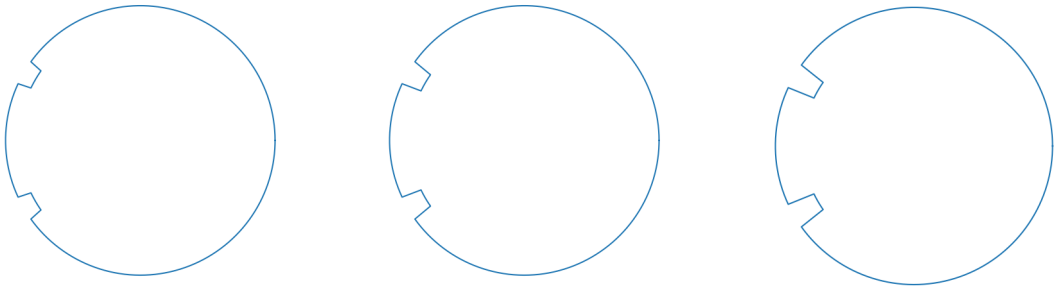

m) p150w10d0.05 n) p150w10d0.075 o) p150w10d0.1

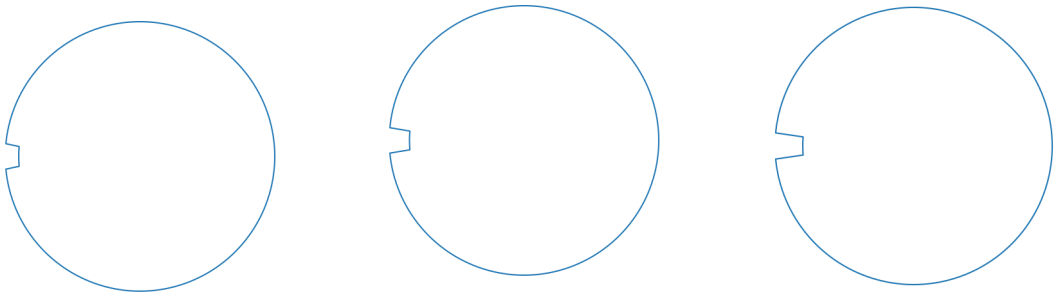

p) p180w10d0.05 q) p180w10d0.075 r) p180w10d0.1

Figure 24: Initial groove configurations investigated

5.4. Cross-flow and in-line displacement amplitude values

It can be argued that the cross-flow displacement of the cylinder is perhaps the most important parameter that can be used to study the VIV of a circular cylinder and compare the effects of the grooves. Vortex-induced vibrations lead to cyclical stresses on the structure (like a cylinder or pipe). These stresses cause material fatigue, which over time can lead to structural failure. The displacement amplitude in the cross-flow direction is a direct measure of these stresses, as larger displacements result in larger stress cycles and faster fatigue. The vortex shedding process drives the VIV mechanism. As vortices are shed alternatively from both sides of the structure, they induce a lift force which results in motion in the cross-flow direction. Hence, measuring the cross-flow displacement gives direct information about the intensity of vortex shedding. Grooves aim to disrupt the vortex shedding process, thereby reducing or increasing the resulting vibrations. Therefore, comparing the cross-flow displacement amplitude for different groove configurations directly indicates their relative effectiveness. Hence, it is only reasonable to start the investigation by looking at these values.

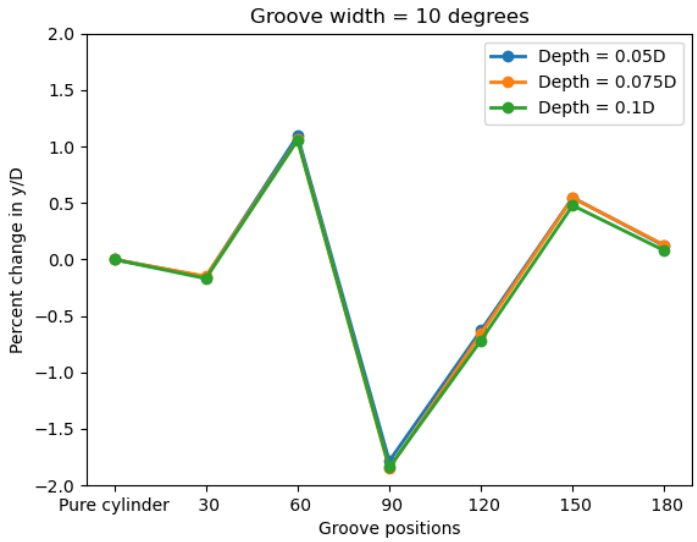

Figure 25: Percentage variation in cross-flow displacement amplitude values

Figure 25 shows a plot of the relative change in the cross-flow oscillation amplitudes for different grooved configurations, compared to that of the smooth cylinder case that was investigated earlier. The actual values for the amplitudes are tabulated in Appendix 1. Also, note that the “Pure cylinder” in this and the following plots refer to the smooth cylinder case (section 1.2).

The plot initially reveals a notable observation: the data points for different groove depths nearly coincide. This indicates that within the range investigated in this study, groove depth does not significantly influence the amplitude of cross-flow oscillations. A similar observation was reported in a previous numerical study conducted by (Hu et al., 2023), where the effect of staggered grooves on VIV suppression was examined in a 3D flexible tensioned riser under turbulent flow conditions. In that study, groove depths of 0.8D and 0.12D yielded minimal differences. However, expanding the depth to 0.16D resulted in a distinct and favourable suppression effect.

With varying angular position of the grooves, not much variation is seen for the given width of 10°. A maximum of around 1.85% reduction in the VIV amplitude compared to a smooth cylinder is observed for the case with grooves at p90. Other than that, a reduction in VIV amplitudes is also observed for the p30 and p120 cases showcasing a maximum reduction of around 0.17% and 0.72% respectively. On the other hand, the remaining cases showcase slight increments in the VIV oscillations, the p60 case with the most increment of around 1.1% and the p150 and p180 cases with a maximum of around 0.55% and 0.13% increment compared to that of the smooth cylinder respectively.

Figure 26 shows the percentage variations in the in-line oscillation amplitudes compared to the smooth cylinder case. The general trend of the curves follow a similar trajectory as for the cross-flow amplitude curves. Similar to what has been observed for the cross-flow oscillation amplitudes, with change in the groove depth, no significant variation in in-line amplitudes is observed. As for the cross-flow amplitudes, a maximum suppression is seen at p90 for in-line amplitude values, with a maximum reduction of 3.66% compared to the smooth cylinder case. The p60 case results in the maximum increment of 1.43%. Other cases did not report any significant deviation either. The actual values are tabulated in Appendix 1.

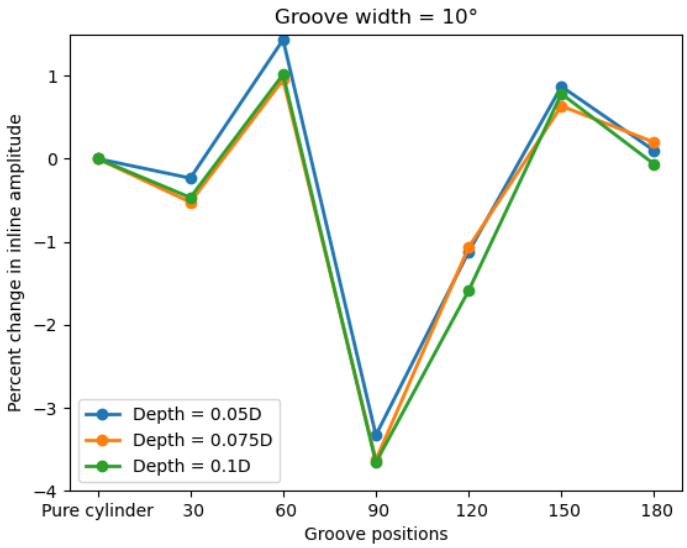

Figure 26: Percentage variation in in-line displacement amplitude values

Thus far, the investigations have primarily focused on varying two parameters of the grooves: the angular position and the depth, while keeping the radial width at a constant 10°. Despite these alterations, the VIV oscillations have shown no significant deviations, neither increasing nor decreasing, compared to the oscillations of a smooth cylinder at Re = 100. The most systematic progression appears to be influenced by the variation in groove widths. It is noteworthy that further changes in groove depth could yield improved suppression, as discussed earlier in this section, referencing the study conducted by (Hu et al., 2023). However, due to constraints in time and computational resources, the present study primarily analyses the impact of groove width, leaving the further investigations on the influence of groove depth for future research.

From the analysis of the smooth cylinder case, it was predicted that the highest variations in VIV might be observed for p90 and p60 cases due to the position of the separation points (section 5.2). Additionally, from the results presented above, these two cases show the greatest variations. Keeping this argument in mind, further cases are run and investigated with a variation in the width of the grooves for the p90 and p60 cases. The width of the grooves is varied between 10°, 15°, and 20°. Also, the cases with the groove positioned at p180 might be interesting to investigate further since the incoming flow first interacts with the cylinder geometry at this position. So, the study with the variation of the width is also conducted for the p180 case, although not much variation was observed for this case with a groove width of 10°. All the aforementioned cases are conducted for

all three depth variations as before. Therefore, in total, 3 positions x 2 new widths x 3 depths = 18 additional cases are run and investigated. Figure 27 illustrates the additional 18 cases that are aforementioned.

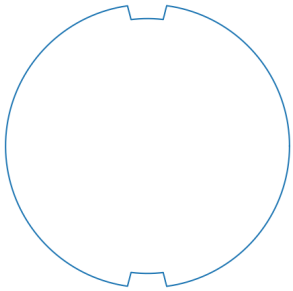

a) p90w15d0.05

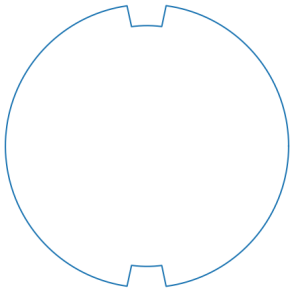

b) p90w15d0.075

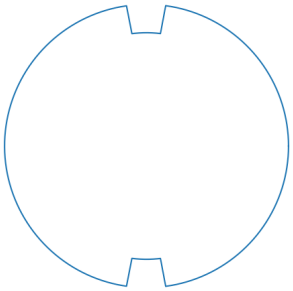

c) p90w15d0.1

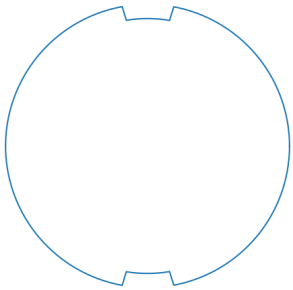

d) p90w20d0.05

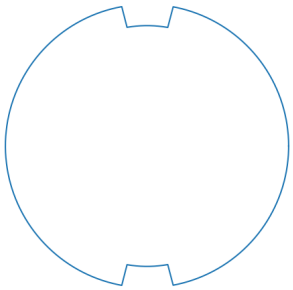

e) p90w20d0.075

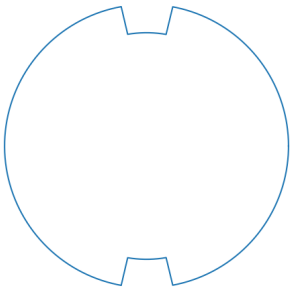

f) p90w20d0.1

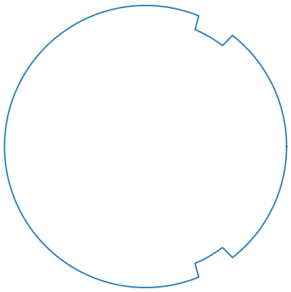

g) p60w15d0.05

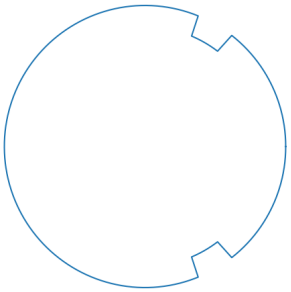

h) p60w15d0.075

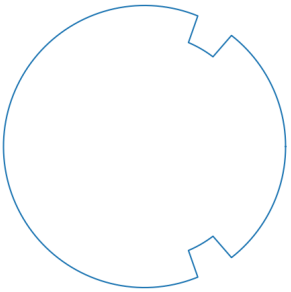

i) p60w15d0.1

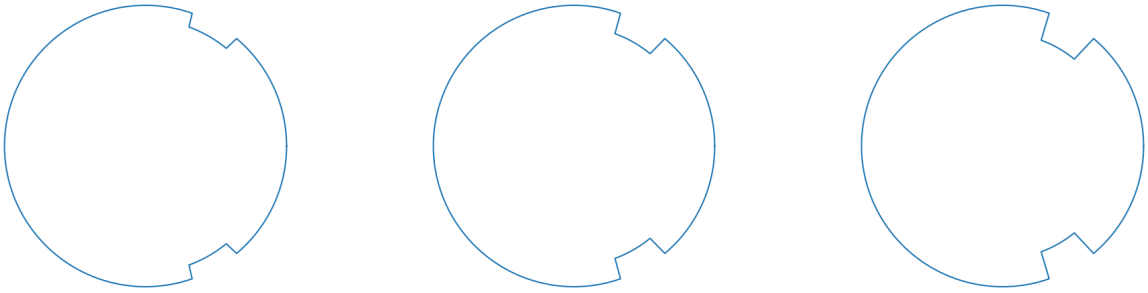

j) p60w20d0.05 k) p60w20d0.075 l) p60w20d0.1

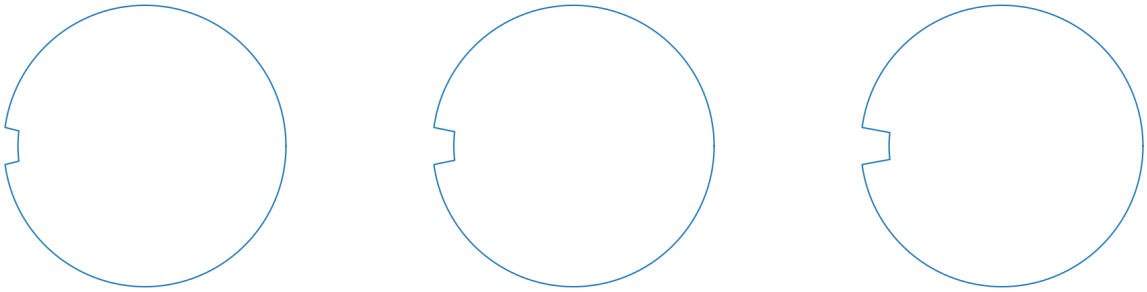

m) p180w15d0.05 n) p180w15d0.075 o) p180w15d0.1

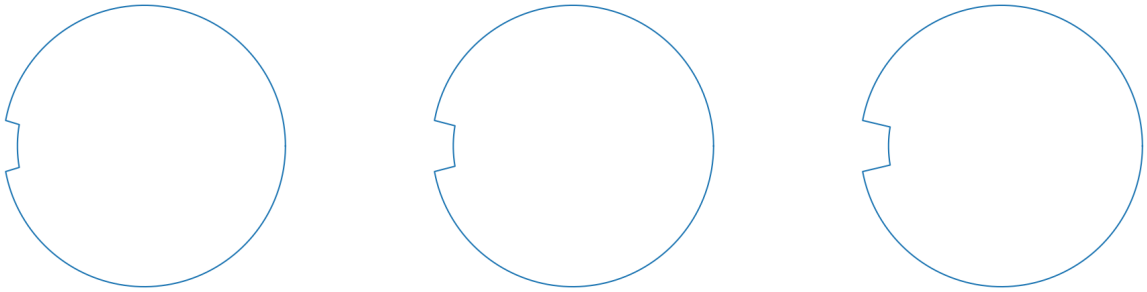

p) p180w20d0.05 q) p180w20d0.075 r) p180w20d0.1

Figure 27: Additional groove configurations investigated

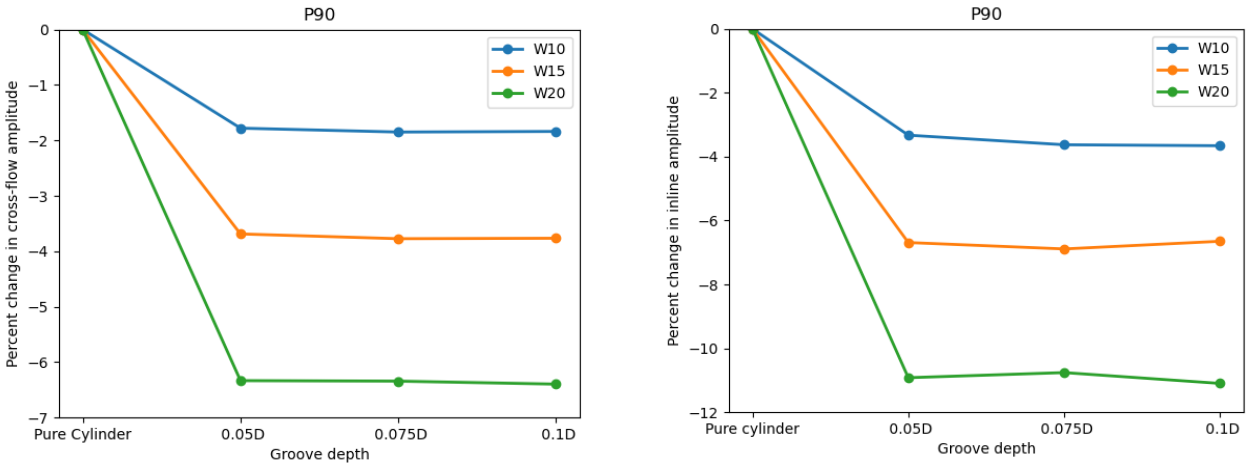

Figure 28: Transverse and in-line osciallation amplitudes for p90 cases

Figure 28 shows the percentage variation of the cross-flow oscillation amplitudes and the in-line amplitudes for the additional cases compared to the smooth cylinder case respectively. As can be seen, the trends observed in the initial study continued with an increment in the groove width. The p90 case initially showed a 1.85% amplitude reduction, and with an increment in groove width, the same showed an increment of around 3.8% and 6.4% for groove widths of 15° and 20° respectively. As for the solutions observed from the 10° width cases, varying groove depths hardly contributed to a significant variation in neither the cross-flow oscillation amplitude values nor the in-line amplitude values. This holds for all the additional cases: with grooves positioned at p90, p60, and p180. Concerning the in-line oscillation amplitudes at p90, the maximum variation was observed at a groove width of 20° with an 11.1% reduction compared to the smooth cylinder case. Whereas, the the grooves with a 15° width reported a maximum of 6.89% reduction.

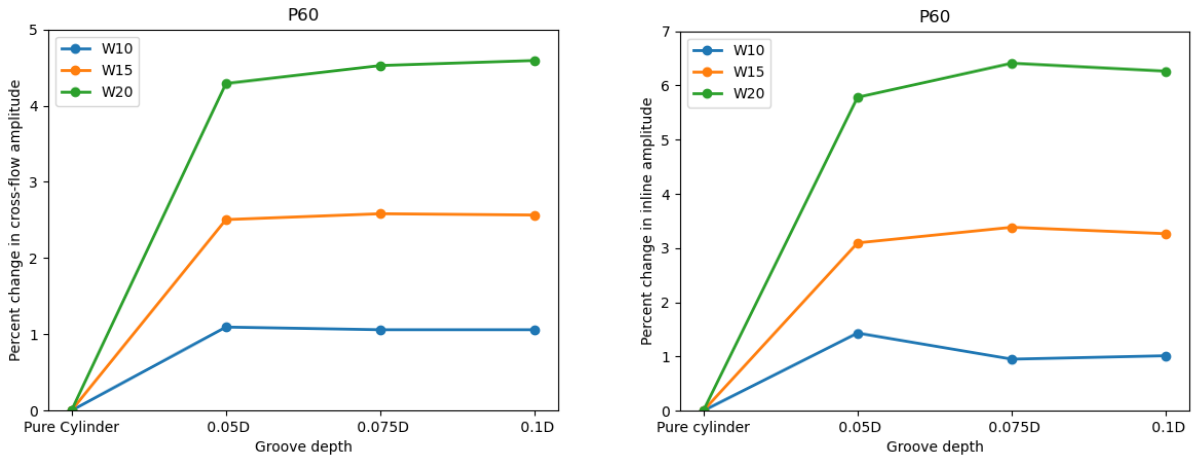

Figure 29: Transverse and in-line osciallation amplitudes for p60 cases

For the p60 cases (figure 29), with an increment in the groove width, the cross-flow oscillation amplitudes increased to around 2.6% and 4.6% for groove widths of 15° and 20° respectively compared to that of the smooth cylinder. As for the in-line oscillation amplitudes, maximum increments of 3.38% and 6.41% are observed for grooved widths of 15° and 20° respectively.

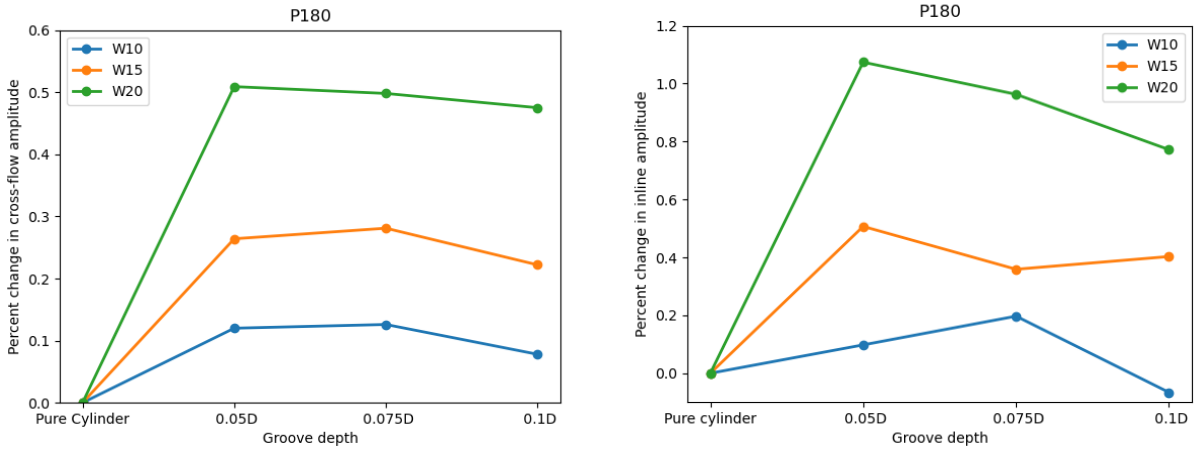

Figure 30: *Transverse and in-line osciallation amplitudes for p180 cases*

The p180 cases (figure 30) reported somewhat lesser variations in the cross-flow amplitude, of around 0.13%, with a groove width of 10°. Although, with the increment in the width the cross-flow amplitudes followed the trend and increased, the values were still quite low to regard the variation compared to the smooth cylinder case significant. Maximum amplitude increments of around 0.28% and 0.5% for the groove widths of 15° and 20° respectively were observed. The maximum increments in in-line oscillation amplitudes for groove widths of 15° and 20° were found to be 0.4% and 1.1% respectively.

Extreme Cases: The p90w20d0.1 and p60w20d0.1 configurations showed the most significant deviations from the smooth cylinder case among the various setups investigated. The p90w20d0.1 configuration recorded the maximum suppression of VIV oscillation amplitude at 6.4%, while the p60w20d0.1 configuration showed an increase in vibration amplitudes by 4.6%. These two cases display significant variations from each other, exhibiting a difference of 11.3% in the cross-flow amplitudes and 19.5% in the in-line amplitudes. Given these differences, it may be valuable to contrast the flow dynamics for these two extreme cases. A more detailed discussion has been provided in Section 5.8. Figure 31 visualizes the cross-flow oscillation curves for the extreme cases along with the smooth cylinder case. Note that in the figure the displacement values illustrated are the coefficients of the cylinder diameter D.

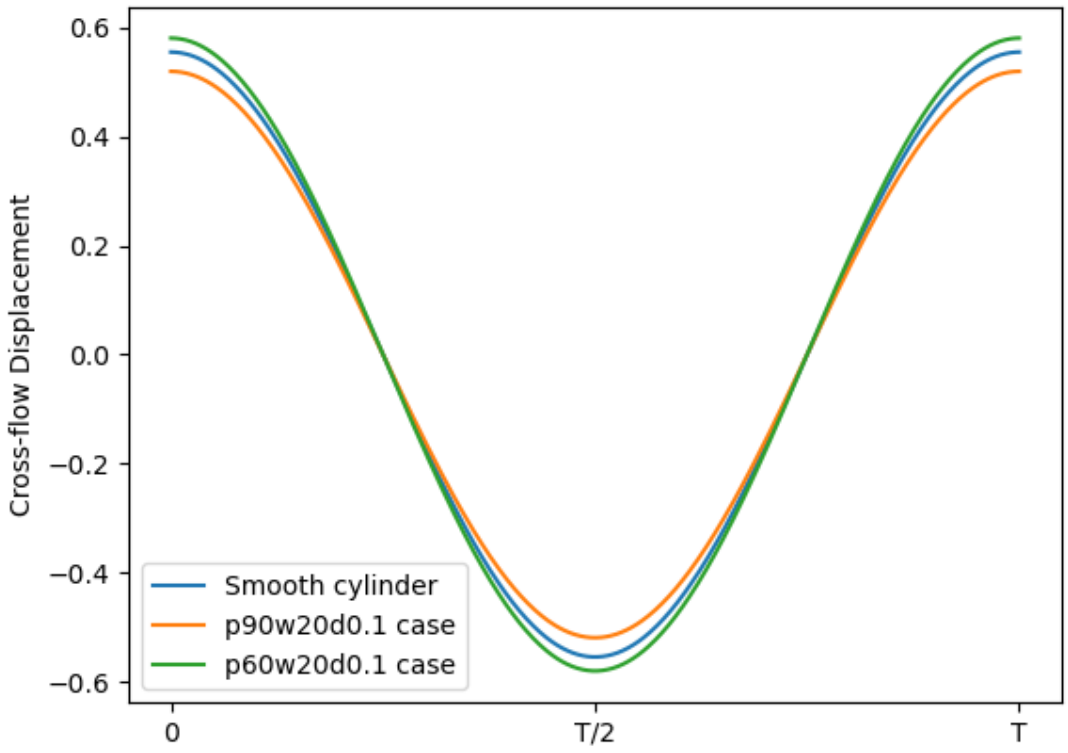

Figure 31: Cross-flow displacements of the extreme cases compared with the smooth cylinder

5.5. Orbital Trajectories

(J. Dahl et al., 2014) underscored the significance of the cylinder's orbital shape in determining the amplitude and frequency of the hydrodynamic forces. Additionally, (Bourguet et al., 2013), asserted that the direction of the orbital motion plays a significant role in the energy transfer between the fluid and the structure.

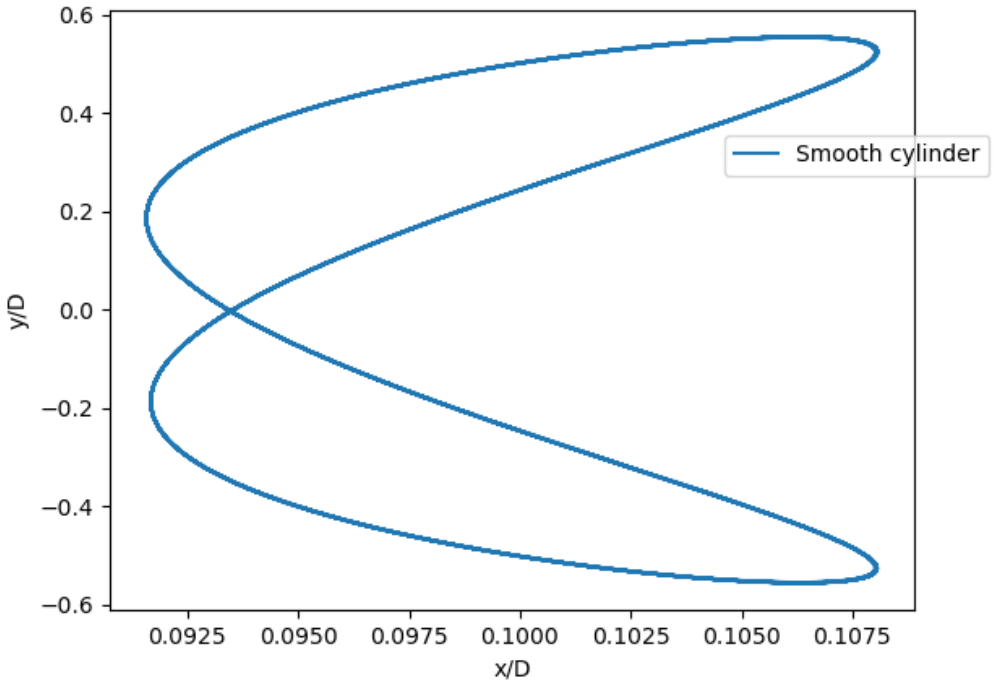

Figure 32: Orbital trajectory of the smooth cylinder case

As already mentioned, the various 2D circular cylinder geometries are allowed to vibrate in both the transverse and the in-line directions of the fluid flow. The initial cases analysed with the 10° wide grooves positioned at p30, p60, p90, p120, p150 and p180 (18 cases) offered very little deviation compared to the smooth cylinder case, and therefore, the orbital trajectories for these cases almost overlap with the orbital trajectory of the smooth cylinder case. Figure 33 illustrates the trajectories of these 18 cases in comparison with the smooth cylinder case. It can be seen that the p90w10d0.1 case offers the most suppression in the VIV in both transverse and in-line directions.

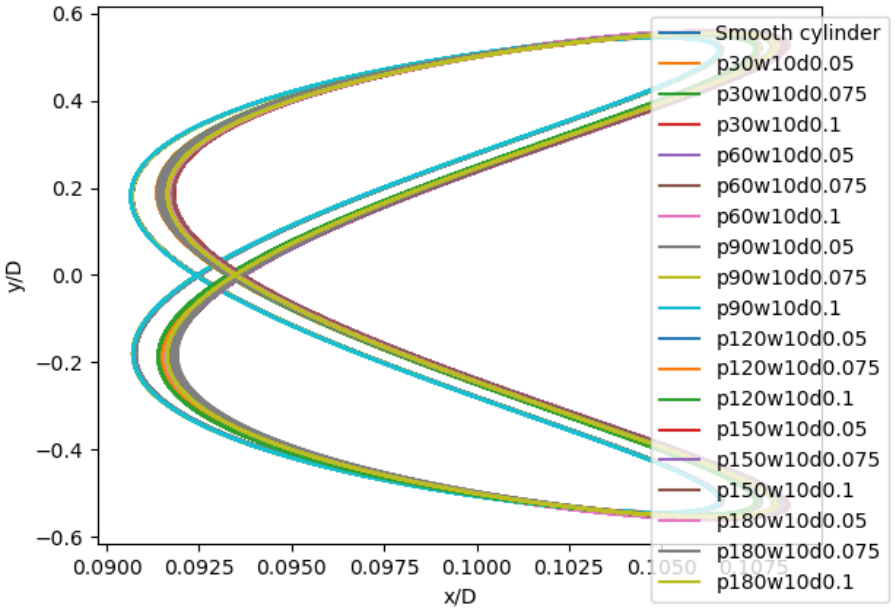

Figure 33: Orbital trajectories of the initial 18 cases with groove width 10°

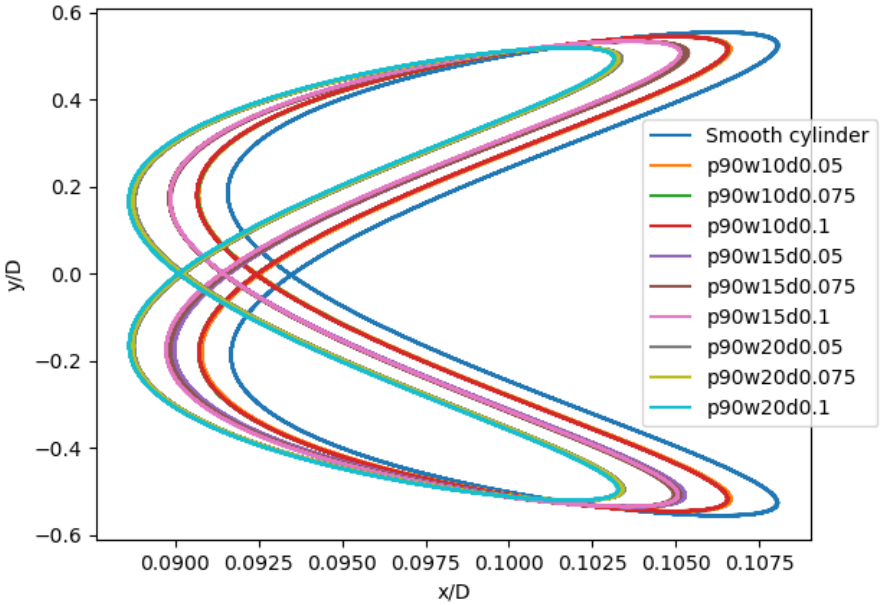

Figure 34: Orbital trajectories of all p90 cases

Figure 34 illustrates the orbital trajectories of all the p90 cases along with the smooth cylinder case normalised by the cylinder diameter D. Firstly, as it has been generally reported from studies conducted on VIV at low Reynolds numbers, an expected figure-eight trajectory is observed for the smooth cylinder as well as for the grooved cases in the lock-in region (J. M. Dahl et al., 2010). As it can be seen, with an increment in the width of the grooves, the trajectories shift leftwards and also shrink. The shrinking of the trajectories refer to the decrease in the transverse oscillation amplitude for the p90 cases which is already presented (section 5.4). The leftward movement points towards the reduction in the in-line oscillation amplitude with an increase in groove width.

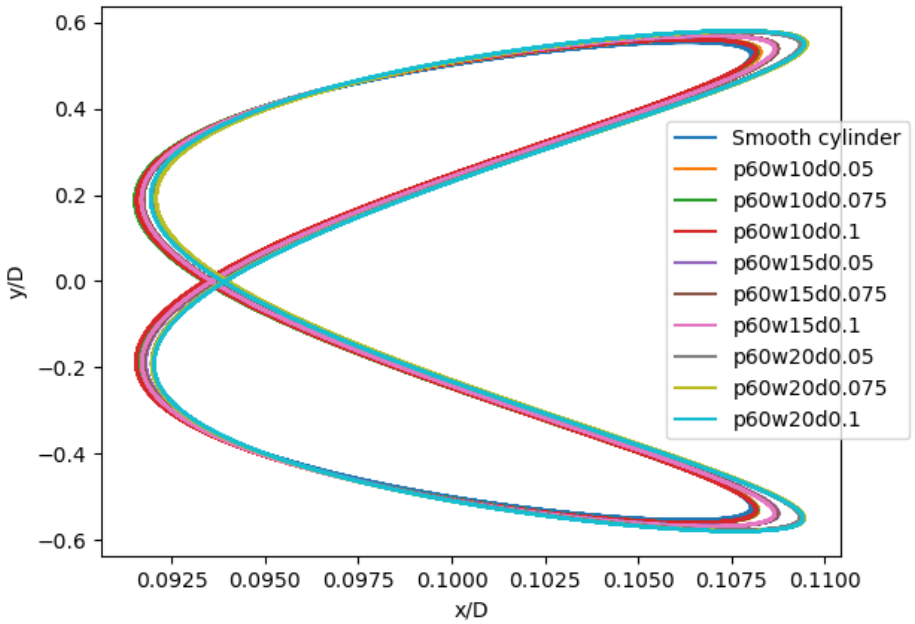

Figure 35: Orbital trajectories of all p60 cases

For the p60 cases, it can be seen from the plot in figure 35, the trajectories shift rightwards and expand with increase in width. As already presented in section 5.4, the transverse amplitude rises for this case with an increase in the width. Additionally, the in-line amplitude also increases for the p60 cases with increase in groove width.

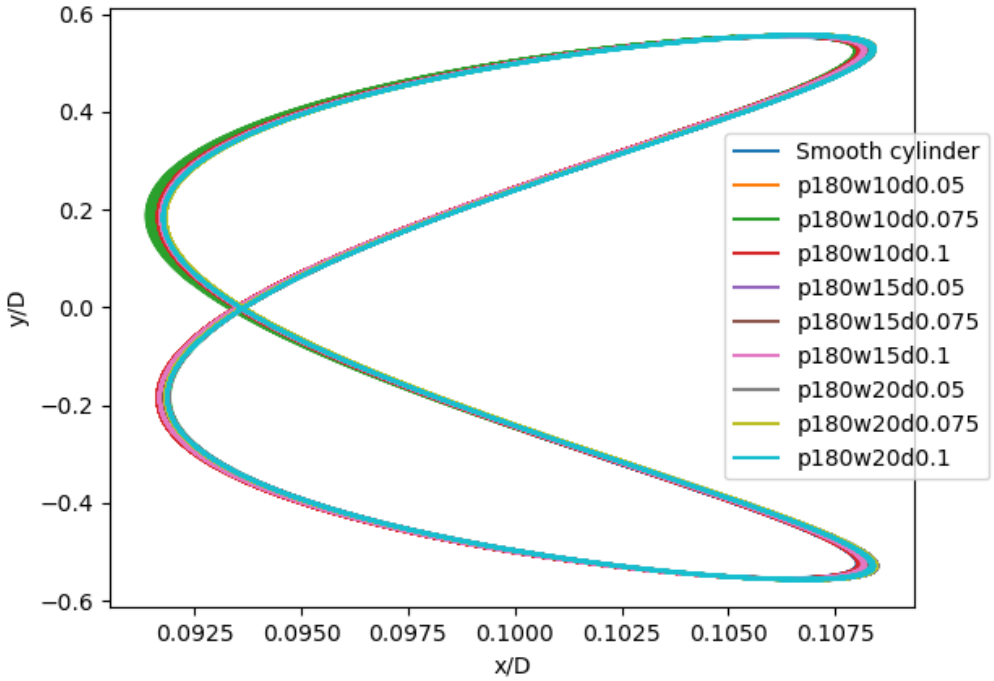

Figure 36: Orbital trajectories of all p180 cases

The p180 case shows a slight shift in the orbital trajectories towards the right and upwards with an increment in the groove width. As already presented, the transverse magnitudes indeed increased, although not significantly.

5.6. Lift and Drag coefficients

The evaluation of force coefficients plays an essential role in understanding the interaction dynamics between the fluid flow and the grooved cylinder. Figure 37 illustrates the lift and drag coefficients reported by the smooth cylinder case.

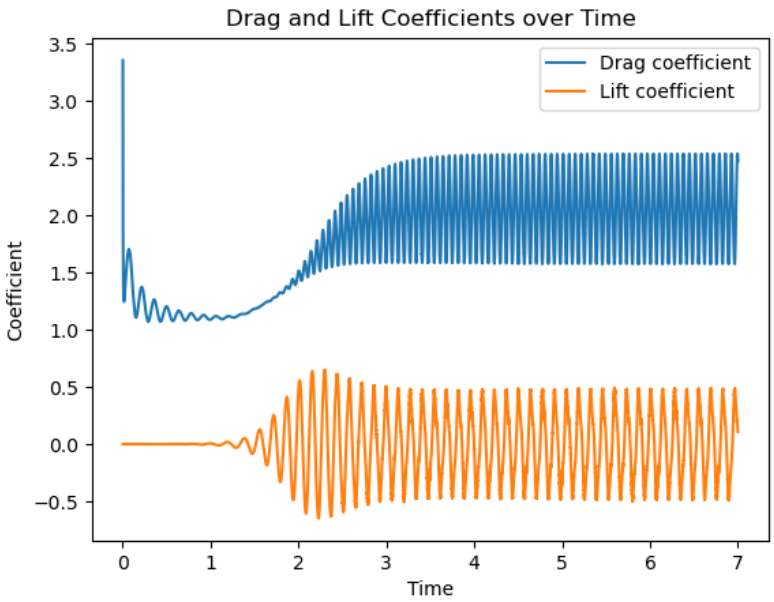

Figure 37: Drag and lift coefficients over time for the smooth cylinder case

Figures 38 and 40 illustrate the plots for the rms lift and drag coefficients for the initial 18 cases (w10). The exact values are tabulated in Appendix 1.

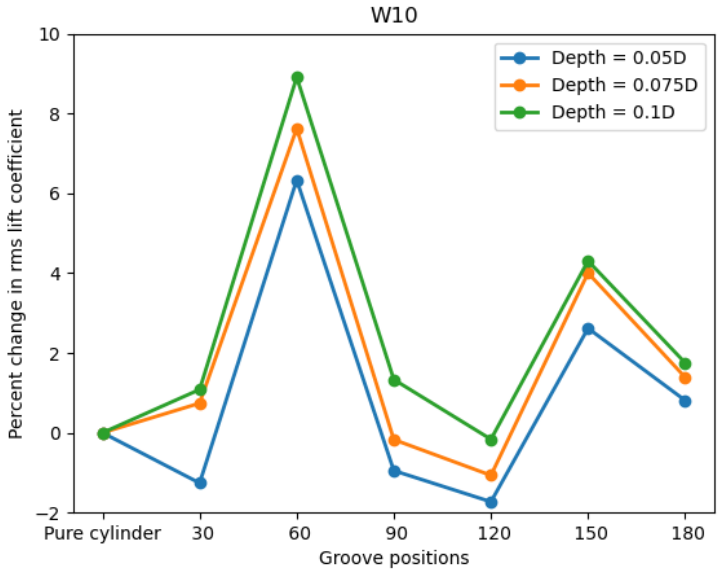

Figure 38: Percentage variation in the rms lift coefficient for all initial cases with groove width of 10°

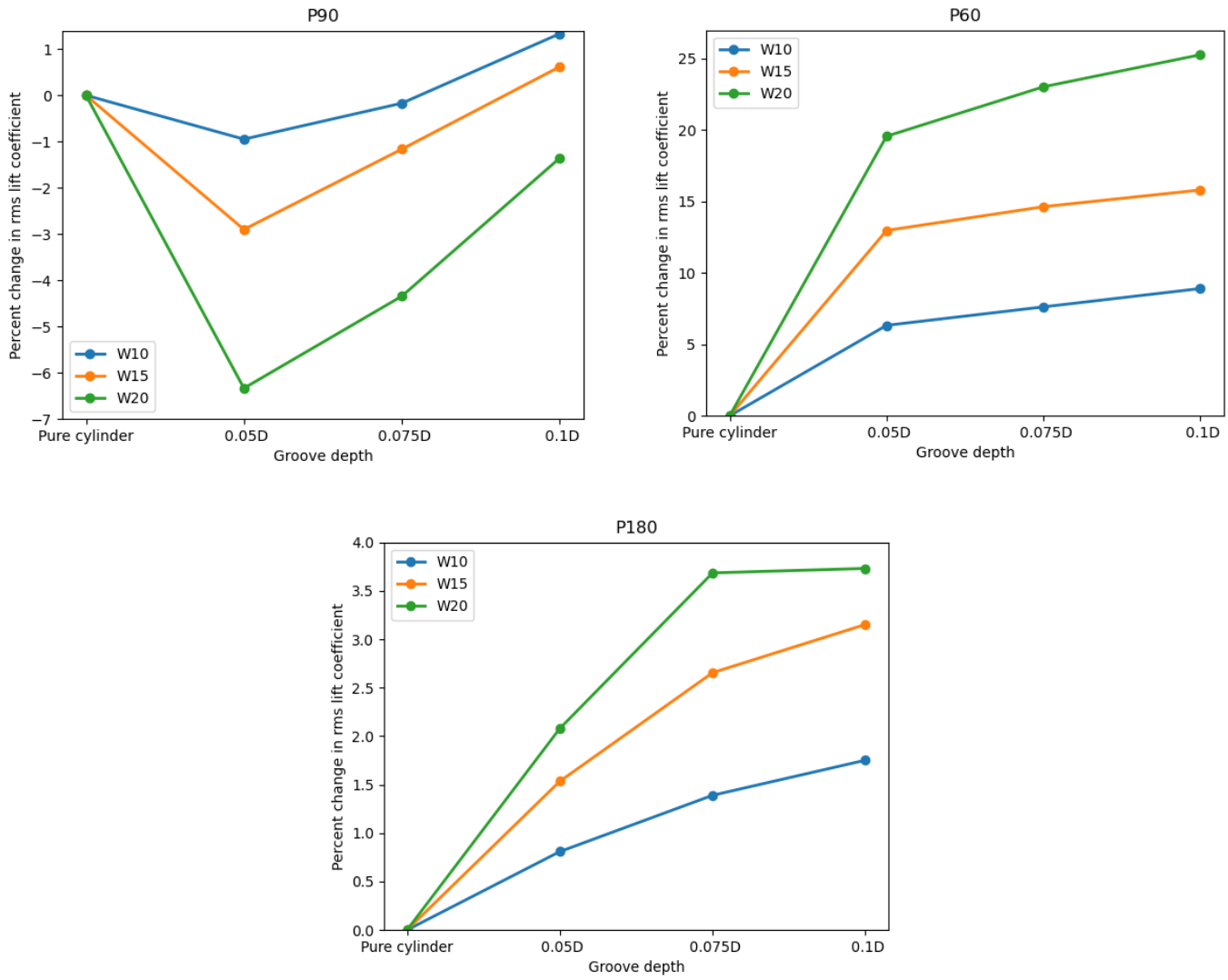

Figure 39: Percentage variation in the rms lift coefficient for all p90, p60 and p180 cases

Lift coefficient ($C_{L,rms}$): The variation in the groove depth shows more effect than for the displacement amplitudes, especially for the lift coefficient values. The grooves at p60 reported the highest lift coefficients with as high as 8.9% increment for the d0.1 case. The p90 case did not report significantly lower values as expected, given the reduction in the cross-flow amplitudes. For all positions, with an increase in groove depth, an increase in the lift coefficient is observed.

Figure 39 shows the lift coefficients for all the p90, p60, and p180 cases. With increment in the groove width, the lift coefficient for the p90 cases reduces by a maximum of 6.5%. This aligns with the reduction in the cross-flow amplitudes observed. Also, as expected, the p60 cases reported an

increment in the lift coefficient values with increasing groove width with a maximum increment of 25.27%. This increment is significantly higher than what was observed for the cross-flow displacement amplitude. This should be reasoned for with further analysis and observations. The p180 cases also reported increment in the lift coefficients with increasing groove width with a maximum of 3.73% increment compared to the smooth cylinder case.

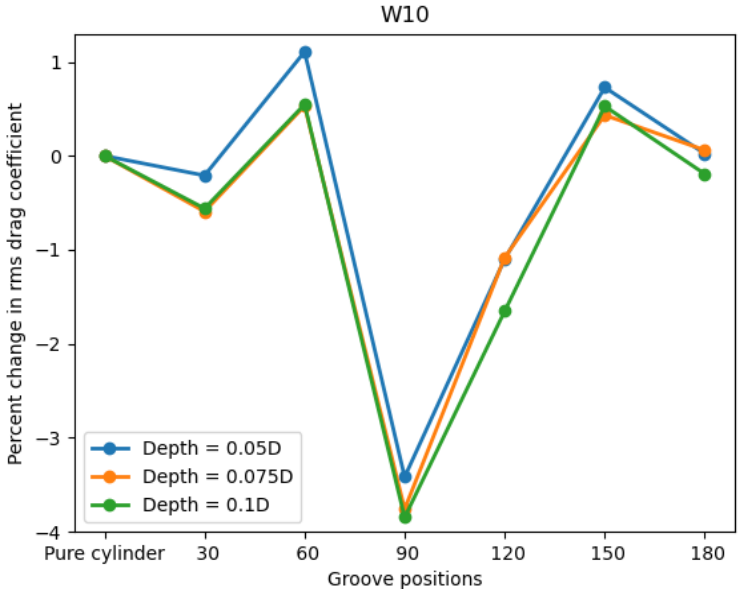

Figure 40: Percentage variation in the rms drag coefficient for all initial cases with groove width of 10°

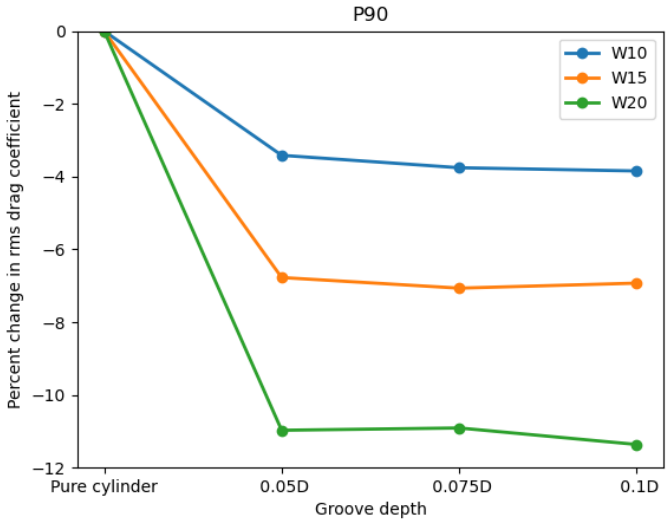

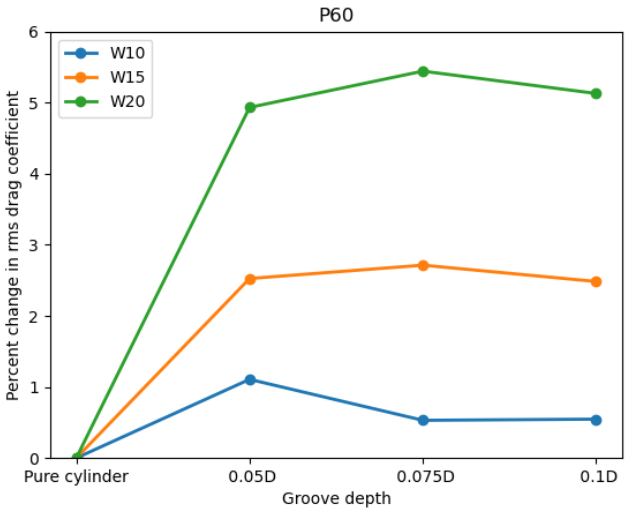

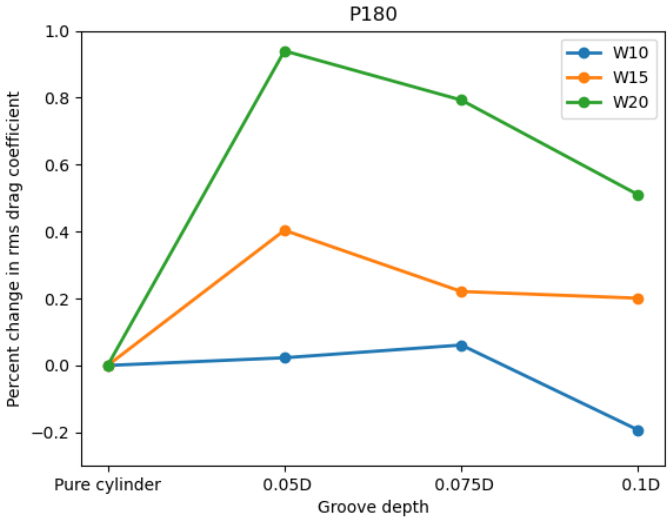

Figure 41: Percentage variation in the rms lift coefficient for all p90, p60 and p180 cases

Drag coefficient ($C_{D,rms}$): The variation in groove depth did not show any significant variations in the drag coefficient values, unlike for the lift coefficient. The maximum deviation was reported by the p90 cases with a decrement of 3.85% compared to the smooth cylinder. The p60 case reported increased values but not more than 1.1%.

Figure 41 illustrates the plots for the drag coefficient for the p90, p60, and p180 cases with varying groove width. With increment in the groove width, the drag coefficient values decrease reaching a maximum deviation of -11.4% compared to the smooth cylinder case. Whereas, for the p60 cases, the drag increases with the increment in groove width, leading to a maximum deviation of 5.4%. Additionally, for the p180 cases, as observed for other parameters, the deviations were not significant but generally increased with increment in the groove width, reaching to a maximum value of 0.94%.

5.7. Shedding frequency

One of the notable results from the investigations conducted on both the smooth and grooved cylinder configurations was the consistency in the shedding frequency. In the case of the smooth cylinder, the shedding frequency was determined to be 7.56 Hz.

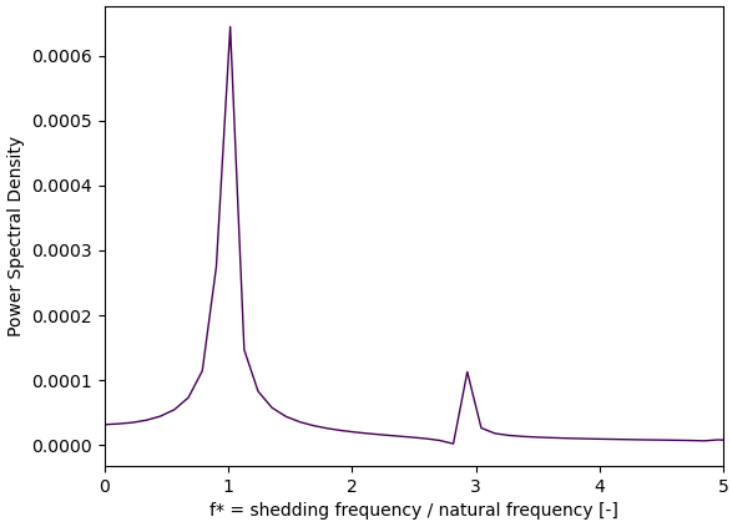

*Figure 42: Power Spectral Density of the frequency ratio f**

Interestingly, this shedding frequency did not change when the cylinder configuration was altered to include the staggered grooves. Despite the modifications in the groove parameters, including angular position, depth, and radial width, the shedding frequency remained constant at 7.56 Hz for all grooved-cylinder cases. This indicates that the different grooved cylinders still matched the lock-in stage of the smooth cylinder. The reason for this might be this simple speculation: changing the cylinder from a smooth to a grooved one didn't involve any change in the cylinder's mass or the stiffness of the springs in the setup, making for a fair comparison (chapter 3).

This consistency suggests that the groove modifications imposed on the cylinder did not significantly affect the vortex shedding dynamics, at least in terms of frequency. This observation further underlines the complexity of the vortex-induced vibrations and the nuanced impact of geometric modifications on the fluid-structure interaction phenomena.

Further investigations might be required to fully comprehend the subtle interactions between the staggered grooves and vortex shedding dynamics. However, these findings contribute to a better understanding of the VIV suppression mechanisms and provide valuable insights for future research efforts in the field.

5.8. Vortex shedding

The purpose of this study is, in part, to examine vortex shedding and its variations in different configurations of grooved cylinders. To achieve this, it is beneficial to scrutinise the vorticity contours of these cylinders over one cross-flow cycle. In the context of this study, which investigated 36 distinct grooved-cylinder configurations, it proves constructive to concentrate on the most significant cases. The configurations that yielded the most substantial outcomes were p90w20d0.1, which demonstrated the greatest suppression of VIV, and p60w20d0.1, which conversely exhibited the most substantial increase in VIV. These two distinct scenarios diverged considerably, with an 11.73% difference in cross-flow amplitudes and a 19.53% variation in in-line displacement amplitudes.

Comparing these specific cases and scrutinising the vorticity contours surrounding the cylinders, within their wake, and around the grooves, may provide valuable insights. Figure 43, displays the vorticity contours of these two notable cases side by side, each marked at 0.1T intervals. Here, T is the time period of one cross-flow oscillation, equivalent to 0.132 seconds. As it has already been mentioned that the vortex shedding frequency for all the grooved-cylinder cases remains the same as for the pure cylinder case, it is easier to compare the two extreme cases at each time instance.

Firstly, it can be noted that the vortices in the wake of both the grooved cylinders presented in figure 43, as well as for the pure cylinder case, display the 2S modes. This is reasonable and expected as the Reynolds number is set to 100 in the present study which implies that the flow is laminar. Numerous studies have documented the 2S modes for the flow at low Reynolds number (Williamson & Roshko, 1988).

For the sake of simplicity and clarity, in this section the p90w20d0.1 is referred to as “p90” whereas the p60w20d0.1 case is referred to as “p60”.

The series of snapshots presented in figure 43 start from the oscillation crest, i.e the highest positive cross-flow displacement. At this instance, it is interesting to focus on the region of low vorticity on the cylinders’ circumference, which is the separation point. For the p90 case, this point lies a little downstream of the top groove where it goes all the way to the inside of the top groove for the p60 case. For the p90 case, high positive vorticity can be seen towards the edges of the top groove. On the other hand, for the p60 case, regions of high positive vorticity are seen around the outer corners

of the top grooves. In both cases, the bottom groove is majorly a region of low vorticity. However, the high positive vorticity region extended further for the bottom groove in the p90 case than for the p60 case. As the cylinder starts moving downwards, more regions of high positive vorticity are observed around the top groove in the p60 case than for the p90 case. Meanwhile, the lower groove in both cases gradually transforms into a high vorticity region. The downward movement of the separation point is fairly similar in both cases except the early interaction in the p90 case with the lower groove. Once the cylinder reaches to the trough of the cycle, the conditions are the same as at the crest but flipped about the centerline. Same dynamics come into play when the cylinder continues the movement upwards.

There are no significant variations observed for the two cases at each time instance. Therefore, it might be more worthwhile to analyse the vorticity contours closer to the cylinder walls and within the grooves.

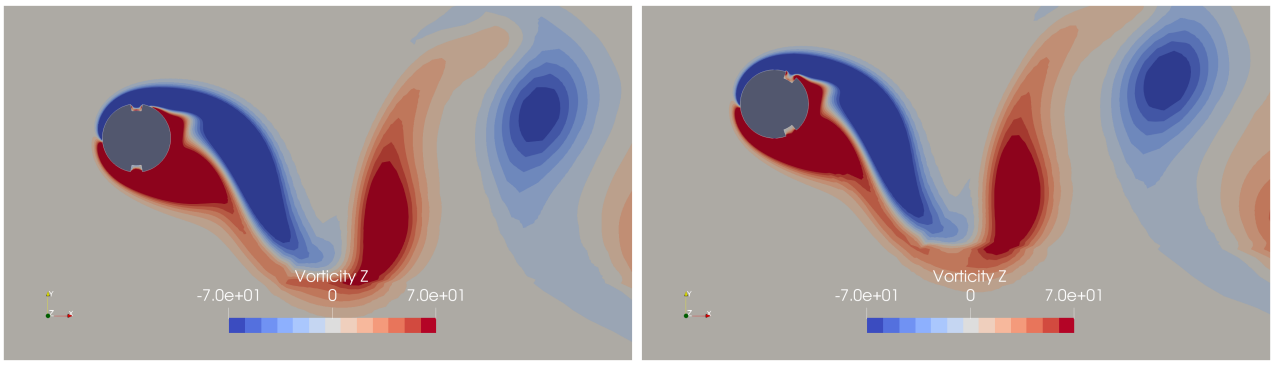

a) t = T/10

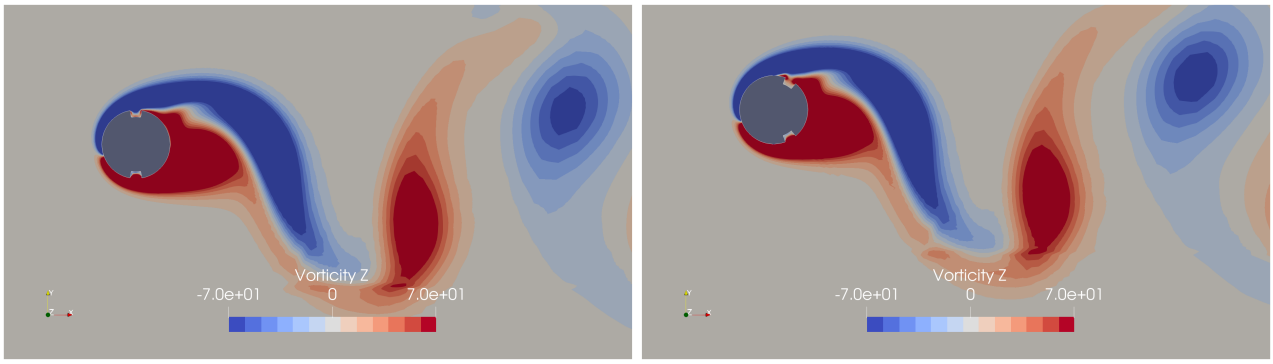

b) t = 2T/10

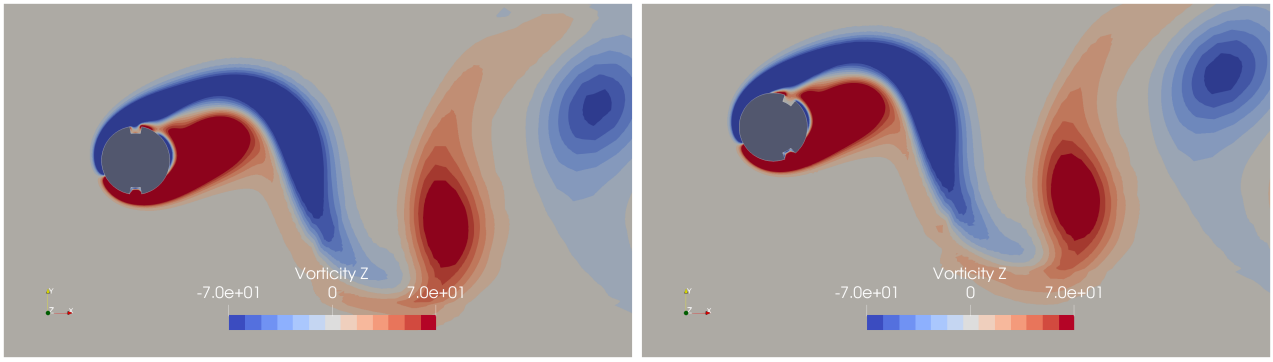

c) t = 3T/10

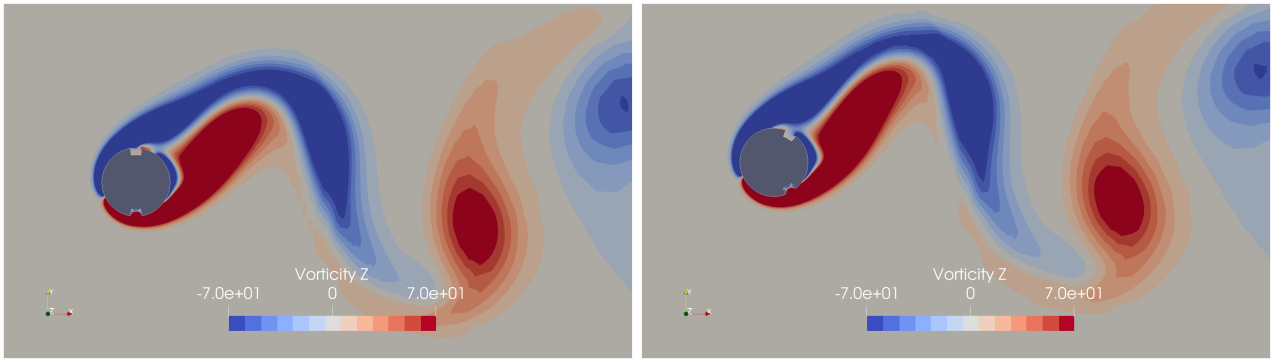

d) t = 4T/10

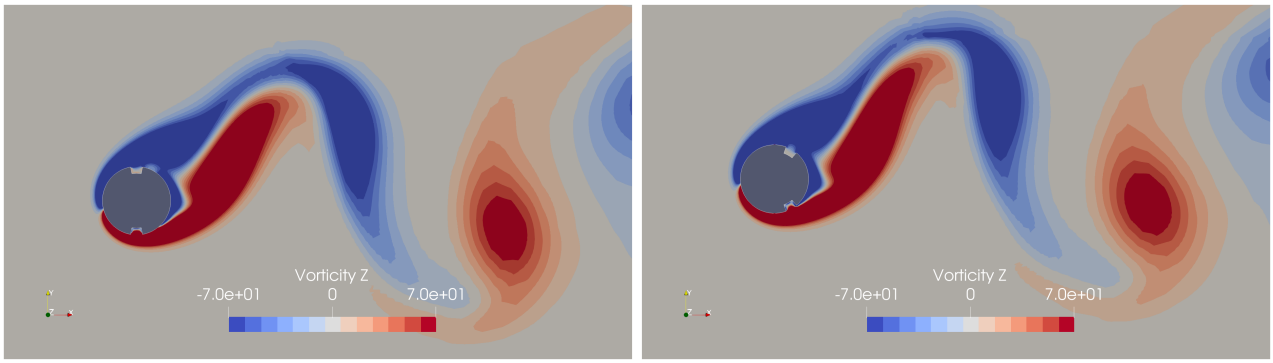

e) t = 5T/10

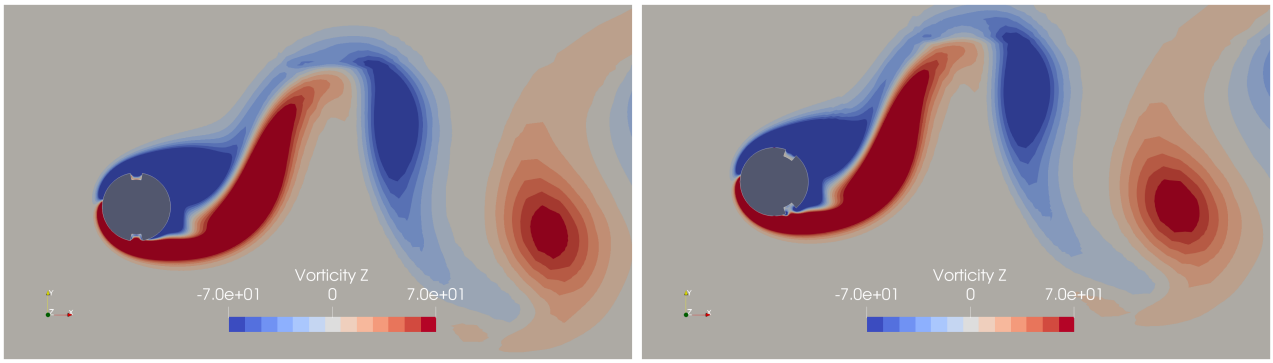

f) t = 6T/10

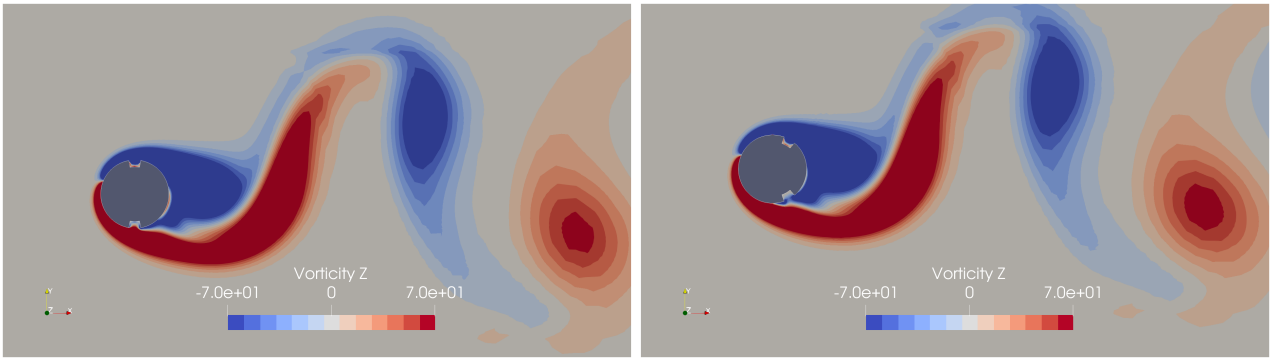

g) t = 7T/10

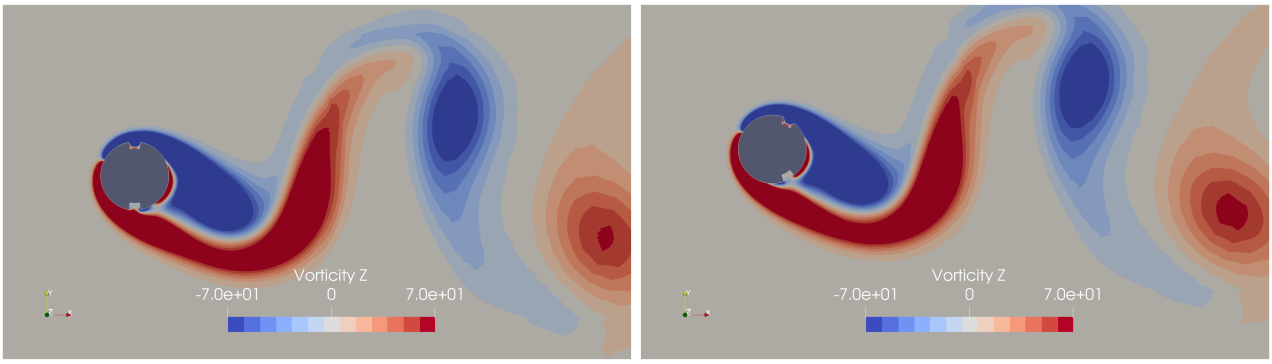

h) t = 8T/10

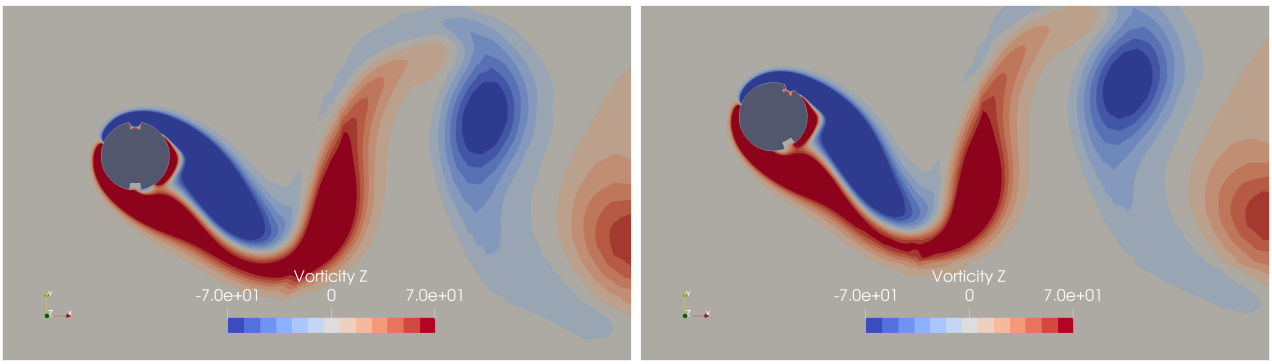

i) t = 9T/10

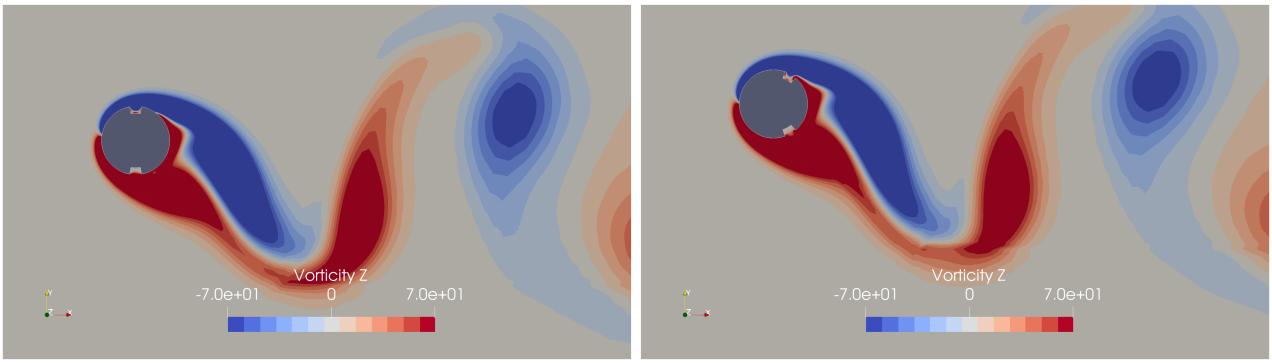

j) t = T

Figure 43: Vorticity contours for the p90w20d0.1 and p60w20d0.1 cases over one cross-flow oscillation

Figure 44 shows the snapshots of the same time instances as figure 43 but zoomed in to capture the flow dynamics in and around the grooves in both the cases.

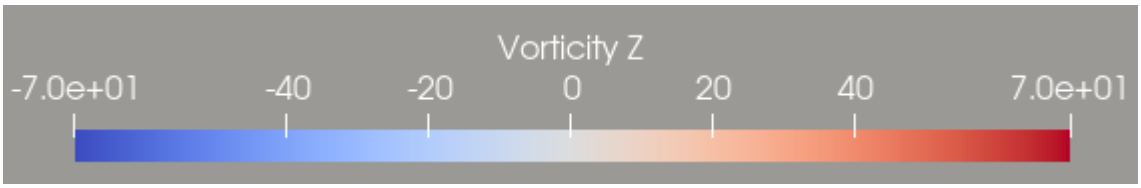

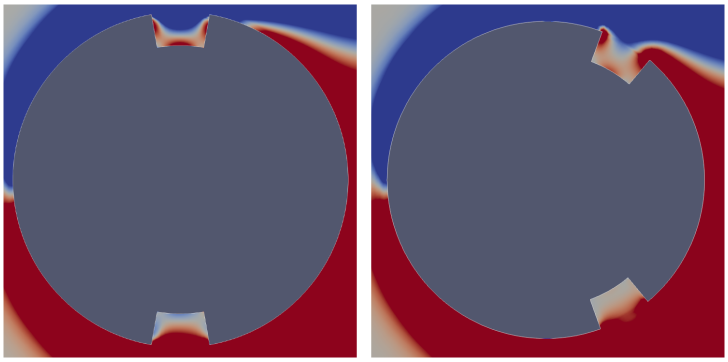

a) t = T/10

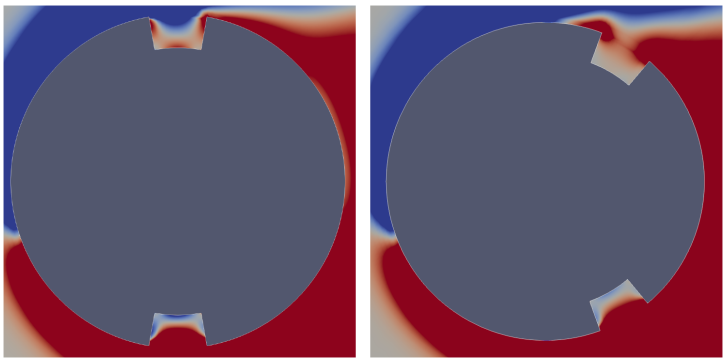

b) t = 2T/10

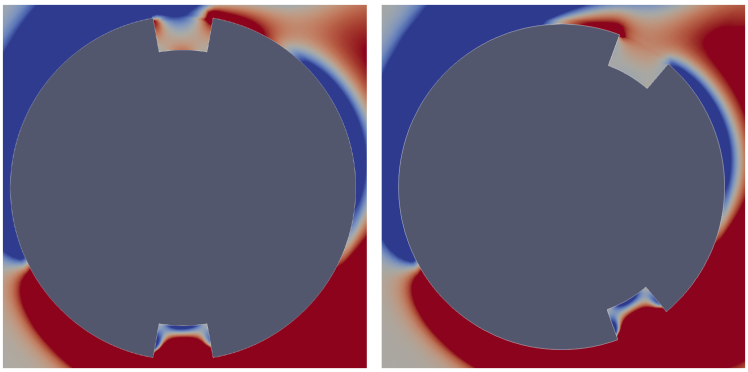

c) t = 3T/10

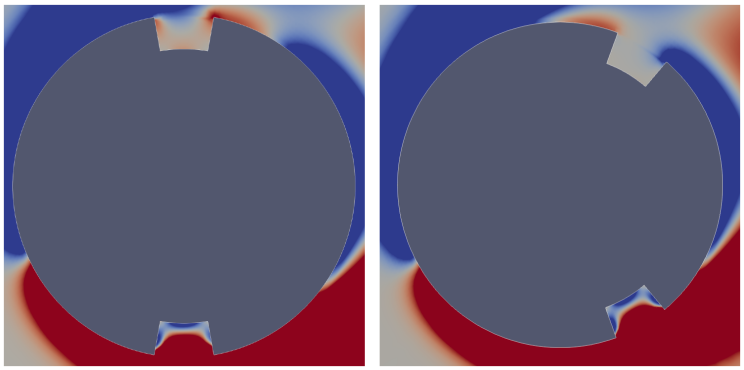

d) t = 4T/10

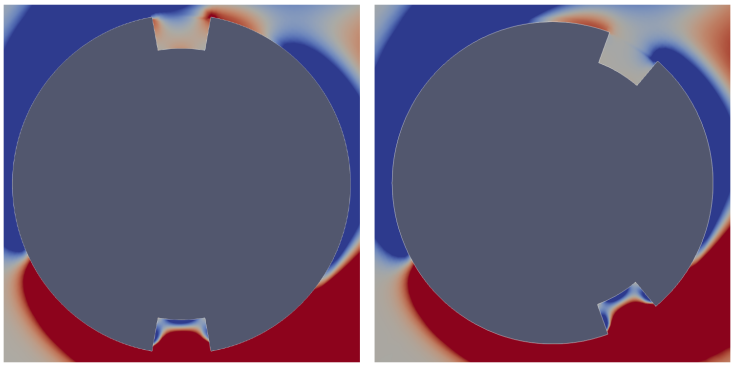

e) t = 5T/10

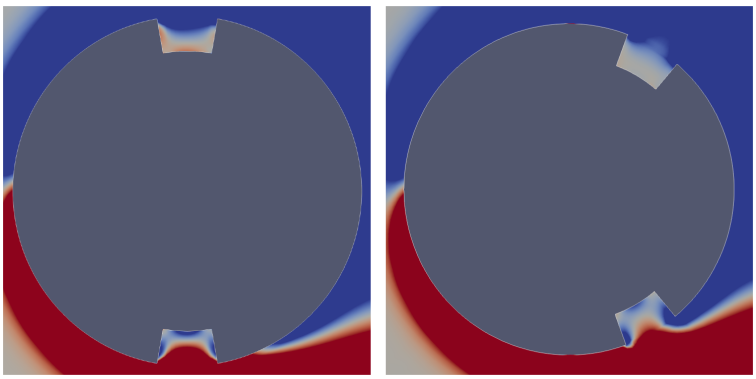

f) t = 6T/10

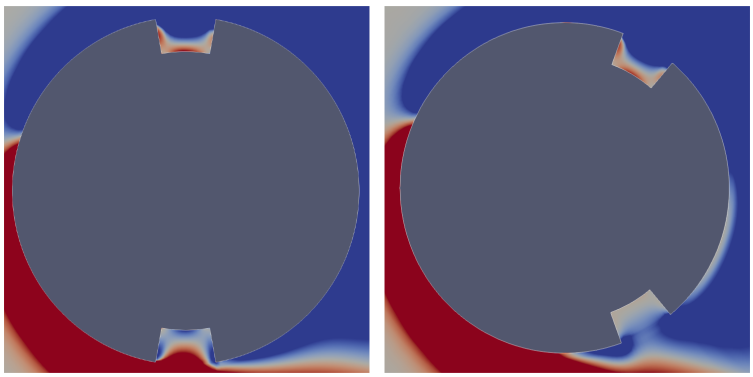

g) t = 7T/10

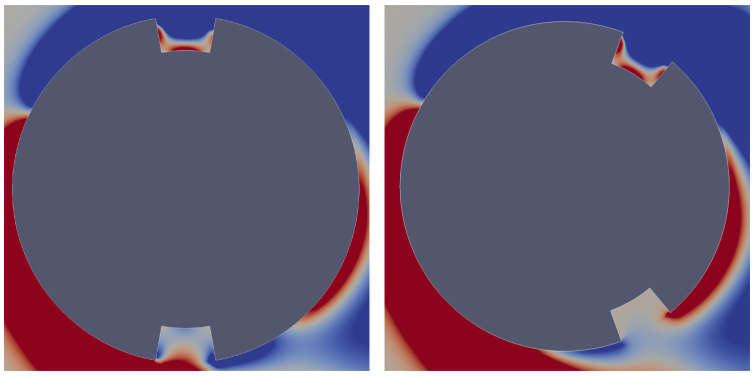

h) t = 8T/10

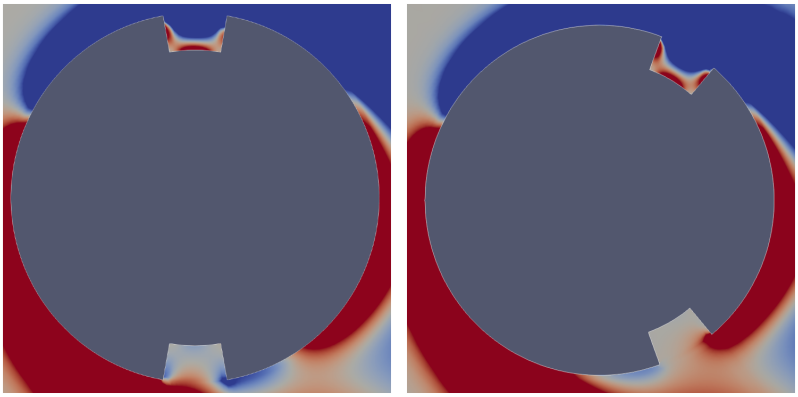

i) t = 9T/10

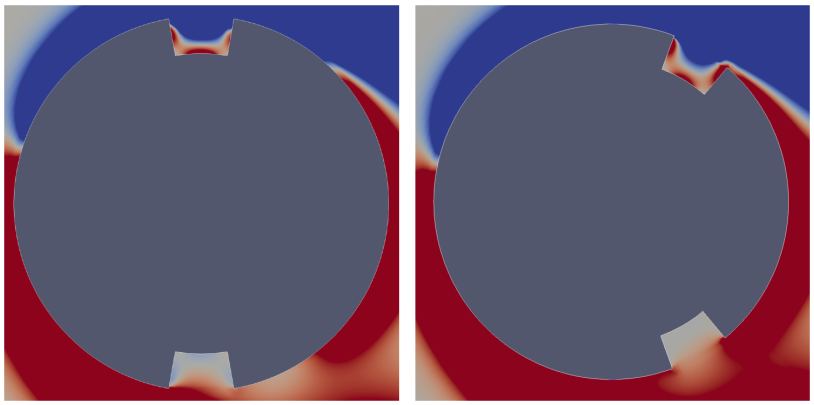

j) t = T

Figure 44: Vorticity contours for the p90w20d0.1 and p60w20d0.1 cases over one cross-flow oscillation: zoomed on the grooves

The comparison outlined above makes it clear that the key difference between the flow dynamics of these two cases stems from the interaction of the separation point, or the region of low vorticity. For the p60 cases, the region of low vorticity can readily enter the grooves, since these grooves are located further downstream compared to the p90 case. In the p90 case, the low-vorticity regions

need to move more significantly upstream towards areas with more positive pressure gradients. Because of this consistent interaction with the grooves in the p60 case, a greater lift is produced. On the other hand, the p90 case, which sees less interaction with the grooves, produces a smaller lift. Although a thorough theoretical study is required to fully understand the fluid-flow dynamics in both these cases, it's important to note that this current study was constrained by time, preventing a more detailed investigation. Despite these constraints, valuable insights have been gained, setting a direction for future, more comprehensive studies.

6

Conclusion

In conclusion, this research extensively examined the impact of staggered groove configurations on Vortex-Induced Vibrations (VIV) of a two-dimensional circular cylinder at Reynolds number (Re) of 100 under lock-in conditions. Employing OpenFOAM, an open-source Computational Fluid Dynamics (CFD) tool, the study comprehensively analyzed 36 distinct grooved-cylinder configurations, characterized by the grooves' position, width and depth, and compared the findings with a reference smooth cylinder case.

The cylinders were elastically mounted on springs permitting both in-line and cross-flow degrees of freedom for cylinder movement. The absence of damping allowed high-amplitude oscillations to occur. A fluid-structure interaction setup was replicated by adopting a partitioned approach linking a CFD solver with a rigid body motion solver. Mesh movement resulting from cylinder motions was handled using a morphing mesh technique.

Notably, it became evident that groove width variations (between 10°, 15°, and 20°) had a significantly larger impact on the cylinder's VIV characteristics than groove depth variations (between 0.05D, 0.075D, and 0.1D, where D is the cylinder diameter). The depth of the grooves may offer further insights, but exploring this was beyond the scope of the current study.

From the analyses of the various grooved-cylinder cases, results and discussions were presented around the transverse and cross-flow displacements, orbital trajectories, force coefficients and the shedding frequencies.

Among the cases studied, the greatest VIV suppression was observed in the p90w20d0.1 case with a decrease of 6.4% in cross-flow and 11.1% in in-line amplitude values relative to the smooth

cylinder case. Conversely, the p60w20d0.1 case presented an increase in VIV with cross-flow and in-line amplitude values growing by 4.6% and 6.4% respectively. The cylinder cases reporting the extreme values were visualized and analyzed, studying the vorticity contours around the cylinder and grooves.

This study provides a promising base for further investigation into the impact of cylinder modifications on VIV characteristics, ultimately guiding engineering design for structures exposed to fluid flows.

7

Further work

While this thesis has addressed a specific aspect of Vortex-Induced Vibrations (VIV) modelling and prediction, it certainly opens doors for further research in this critical area of fluid dynamics. Based on the results and findings, it can be stated that the present work should create a solid groundwork for future research endeavors. With these insights in mind, several promising avenues for future studies can be highlighted.

1. The present study focused on a certain number of combinations of the groove positions, depths and widths. As for the groove positions, mostly symmetric configurations were used except for the p180 cases. A future work could investigate different groove positions as well as groove sizes. In the present work, not much deviation was observed with the variation of the groove depths. As (Hu et al., 2023) reported from their analysis of a 3D flexible riser with staggered grooves in turbulent flows, significant variations might be observed for groove depths exceeding 0.16D.

2. Staggered grooves are used in the present study to investigate VIV suppression. In a future work, other types of grooves, for example dimples, squares, triangular, etc. can be used and the results can be compared to find the most efficient groove shape.

3. The 2D cylinder configurations are subjected to a laminar flow (Re = 100) within this thesis work. However, in order to replicate real-life VIV, the cylinder must be subjected to much higher values of Re. This would introduce turbulence which is a 3D effect. Therefore, the geometry must be 3D as well to capture the turbulent flow around it. Both rigid and flexible 3D cylinders might be modeled. Additionally, to accurately model turbulence, choices must

be made around the selection of appropriate closure models which also require selection of appropriate values of model-specific parameters.

4. The present study considers the cylinder being subjected to a uniform streamlined flow. A future study might subject the geometry to non-uniform flow or even try to replicate ocean waves to model VIV around a marine riser or an offshore structure.

5. Constant VIV of cylindrical structures lead to fatigue damage over time. A fatigue analysis might be introduced to an extension of the present study to investigate the reliability of the structure.

6. In the present work, the structural damping is neglected. In practical cases, however, especially for the structures subjected to the marine environment, the inclusion of a proper non-linear damping model might be necessary to predict realistic VIV responses.

References

- Achenbach, E., & Heinecke, E. (1981). On vortex shedding from smooth and rough cylinders in the range of Reynolds numbers 6×103 to 5×106. *Journal of Fluid Mechanics*, *109*, 239–251. https://doi.org/10.1017/S002211208100102X

- Alletto, M. (2022). Comparison of Overset Mesh with Morphing Mesh: Flow Over a Forced Oscillating and Freely Oscillating 2D Cylinder. *OpenFOAM® Journal*, *2*, 13–30. https://doi.org/10.51560/ofj.v2.47

- Anderson, J. D., & Anderson, J. D. (2011). *Fundamentals of aerodynamics* (5th ed). McGraw-Hill.

- Bai, X., & Qin, W. (2014). Using vortex strength wake oscillator in modelling of vortex induced vibrations in two degrees of freedom. *European Journal of Mechanics - B/Fluids*, *48*, 165–173. https://doi.org/10.1016/j.euromechflu.2014.05.002

- Bearman, P. W. (1984). Vortex Shedding from Oscillating Bluff Bodies. *Annual Review of Fluid Mechanics*, *16*(1), 195–222. https://doi.org/10.1146/annurev.fl.16.010184.001211

- Blackburn, H. M., & Karniadakis, G. E. (1993). *Two-and Three-Dimensional Simulations of Vortex-Induced Vibration Or a Circular Cylinder*. ISOPE-I-93-317.

- Blevins, R. D. (1990). *Flow-induced vibration* (2nd ed). Van Nostrand Reinhold.

- Blevins, R. D. (1994). *Flow-induced vibration* (2. ed., repr. ed. w/updating and new preface). Krieger.

- Blevins, R. D., & Coughran, C. S. (2009). Experimental Investigation of Vortex-Induced Vibration in One and Two Dimensions With Variable Mass, Damping, and Reynolds Number.

- *Journal of Fluids Engineering*, *131*(10), 101202. https://doi.org/10.1115/1.3222904

- Bourguet, R., Karniadakis, G. E., & Triantafyllou, M. S. (2013). Phasing mechanisms between the in-line and cross-flow vortex-induced vibrations of a long tensioned beam in shear flow. *Computers & Structures*, *122*, 155–163. https://doi.org/10.1016/j.compstruc.2013.01.002

- Dahl, J., Hover, F., & Triantafyllou, M. (2014). *High Harmonic Forces and Predicted Vibrations from Forced In-line and Cross-flow Cylinder Motions*.

- Dahl, J. M., Hover, F. S., & Triantafyllou, M. S. (2006). Two-degree-of-freedom vortex-induced vibrations using a force assisted apparatus. *Journal of Fluids and Structures*, *22*(6–7), 807–818. https://doi.org/10.1016/j.jfluidstructs.2006.04.019

- Dahl, J. M., Hover, F. S., Triantafyllou, M. S., Dong, S., & Karniadakis, G. E. (2007). Resonant Vibrations of Bluff Bodies Cause Multivortex Shedding and High Frequency Forces. *Physical Review Letters*, *99*(14), 144503. https://doi.org/10.1103/PhysRevLett.99.144503

- Dahl, J. M., Hover, F. S., Triantafyllou, M. S., & Oakley, O. H. (2010). Dual resonance in vortex-induced vibrations at subcritical and supercritical Reynolds numbers. *Journal of Fluid Mechanics*, *643*, 395–424. https://doi.org/10.1017/S0022112009992060

- Devolder, B., Schmitt, P., Rauwoens, P., Elsäßer, B., & Troch, P. (2015). *A Review of the Implicit Motion Solver Algorithm in OpenFOAM to Simulate a Heaving Buoy*.

- Donea, J., Giuliani, S., & Halleux, J. P. (1982). An arbitrary lagrangian-eulerian finite element method for transient dynamic fluid-structure interactions. *Computer Methods in Applied Mechanics and Engineering*, *33*(1–3), 689–723. https://doi.org/10.1016/0045-7825(82)90128-1

- Facchinetti, M. L., De Langre, E., & Biolley, F. (2004). Coupling of structure and wake oscillators in vortex-induced vibrations. *Journal of Fluids and Structures*, *19*(2), 123–140. https://doi.org/10.1016/j.jfluidstructs.2003.12.004

- Farshidianfar, A., & Zanganeh, H. (2010). A modified wake oscillator model for vortex-induced vibration of circular cylinders for a wide range of mass-damping ratio. *Journal of Fluids and Structures*, *26*(3), 430–441. https://doi.org/10.1016/j.jfluidstructs.2009.11.005

- Feng, C. C. (1968). *The measurement of vortex induced effects in flow past stationary and oscillating circular and D-section cylinders*. https://doi.org/10.14288/1.0104049

- Gad-el-Hak, M. (2001). Flow Control: The Future. *Journal of Aircraft*, *38*(3), 402–418. https://doi.org/10.2514/2.2796

- Govardhan, R., & Williamson, C. H. K. (2000). Modes of vortex formation and frequency response of a freely vibrating cylinder. *Journal of Fluid Mechanics*, *420*, 85–130. https://doi.org/10.1017/S0022112000001233

- Gsell, S., Bourguet, R., & Braza, M. (2016). Two-degree-of-freedom vortex-induced vibrations of a circular cylinder at Re=3900. *Journal of Fluids and Structures*, *67*, 156–172. https://doi.org/10.1016/j.jfluidstructs.2016.09.004

- Guilmineau, E., & Queutey, P. (2004). Numerical simulation of vortex-induced vibration of a circular cylinder with low mass-damping in a turbulent flow. *Journal of Fluids and Structures*, *19*(4), 449–466. https://doi.org/10.1016/j.jfluidstructs.2004.02.004

- Hao, Z., Sun, C., Lu, Y., Bi, K., & Zhou, T. (2022). Suppression of Vortex-Induced Vibration and Phase-Averaged Analysis of the Wake Generated by a Circular Cylinder Covered with Helical Grooves. *Fluids*, *7*(6), 194. https://doi.org/10.3390/fluids7060194

- Hu, H., Pan, Z., Zhao, W., & Wan, D. (2023). Numerical investigation of vortex-induced vibrational responses to a flexible tensioned riser with symmetric grooves in uniform currents. *Ocean Engineering*, *271*, 113780. https://doi.org/10.1016/j.oceaneng.2023.113780

- Jauvtis, N., & Williamson, C. H. K. (2004). The effect of two degrees of freedom on vortex-induced vibration at low mass and damping. *Journal of Fluid Mechanics*, *509*, 23–62. https://doi.org/10.1017/S0022112004008778

- Kang, Z., & Jia, L. (2013). An experiment study of a cylinder's two degree of freedom VIV trajectories. *Ocean Engineering*, *70*, 129–140. https://doi.org/10.1016/j.oceaneng.2013.05.033

- Khalak, A., & Williamson, C. H. K. (1997). FLUID FORCES AND DYNAMICS OF A HYDROELASTIC STRUCTURE WITH VERY LOW MASS AND DAMPING. *Journal of Fluids and Structures*, *11*(8), 973–982. https://doi.org/10.1006/jfls.1997.0110

- Khalak, A., & Williamson, C. H. K. (1999). MOTIONS, FORCES AND MODE TRANSITIONS IN VORTEX-INDUCED VIBRATIONS AT LOW MASS-DAMPING. *Journal of Fluids and Structures*, *13*(7–8), 813–851. https://doi.org/10.1006/jfls.1999.0236

- Kondo, N. (2011). Three-dimensional computation for flow-induced vibrations in in-line and cross-flow directions of a circular cylinder: FLOW-INDUCED VIBRATIONS IN IN-LINE AND CROSS-FLOW DIRECTIONS. *International Journal for Numerical Methods in Fluids*, n/a-n/a. https://doi.org/10.1002/fld.2682

- Leontini, J. S., Thompson, M. C., & Hourigan, K. (2006). The beginning of branching behaviour of vortex-induced vibration during two-dimensional flow. *Journal of Fluids and Structures*, *22*(6–7), 857–864. https://doi.org/10.1016/j.jfluidstructs.2006.04.003

- Lienhard, J. H., Washington State University Technical Extension Service, & Washington State University College of Engineering Research Division. (1966). *Synopsis of lift, drag, and vortex frequency data for rigid circular cylinders*. Technical Extension Service, Washington State University.

- Lucor, D., Foo, J., & Karniadakis, G. E. (2005). Vortex mode selection of a rigid cylinder subject to VIV at low mass-damping. *Journal of Fluids and Structures*, *20*(4), 483–503. https://doi.org/10.1016/j.jfluidstructs.2005.02.002

- Lucor, D., & Triantafyllou, M. S. (2008). Parametric study of a two degree-of-freedom cylinder subject to vortex-induced vibrations. *Journal of Fluids and Structures*, *24*(8), 1284–1293. https://doi.org/10.1016/j.jfluidstructs.2008.06.001

- Navrose, & Mittal, S. (2013). Free vibrations of a cylinder: 3-D computations at Re=1000. *Journal of Fluids and Structures*, *41*, 109–118. https://doi.org/10.1016/j.jfluidstructs.2013.02.017

- Newman, D. J., & Karniadakis, G. E. (1997). A direct numerical simulation study of flow past a freely vibrating cable. *Journal of Fluid Mechanics*, *344*, 95–136. https://doi.org/10.1017/S002211209700582X

- Pontaza, J. P., & Chen, H.-C. (2007). Three-Dimensional Numerical Simulations of Circular Cylinders Undergoing Two Degree-of-Freedom Vortex-Induced Vibrations. *Journal of Offshore Mechanics and Arctic Engineering*, *129*(3), 158–164. https://doi.org/10.1115/1.2746396

- Prasanth, T. K., & Mittal, S. (2008). Effect of blockage on free vibration of a circular cylinder at low *Re*. *International Journal for Numerical Methods in Fluids*, *58*(10), 1063–1080. https://doi.org/10.1002/fld.1771

- Priyadarsan, A., & Afzal, M. S. (2023). Numerical investigation of flow past a circular cylinder modified with a single groove at low Reynolds number. *Physics of Fluids*, *35*(2), 027125. https://doi.org/10.1063/5.0137530

- Roshko, A. (1955). On the Wake and Drag of Bluff Bodies. *Journal of the Aeronautical Sciences*, *22*(2), 124–132. https://doi.org/10.2514/8.3286

- Saltara, F., Neto, A., & Lopez, J. I. H. (2011). 3D CFD Simulation of Vortex-induced Vibration of Cylinder. *International Journal of Offshore and Polar Engineering*, *21*, 192–197.

- Sarpkaya, T. (1995). Hydrodynamic Damping, Flow-Induced Oscillations, and Biharmonic Response. *Journal of Offshore Mechanics and Arctic Engineering*, *117*(4), 232–238. https://doi.org/10.1115/1.2827228

- Sarpkaya, T. (2004). A critical review of the intrinsic nature of vortex-induced vibrations. *Journal of Fluids and Structures*, *19*(4), 389–447. https://doi.org/10.1016/j.jfluidstructs.2004.02.005

- Shoemake, K. (1985). Animating rotation with quaternion curves. *Proceedings of the 12th Annual Conference on Computer Graphics and Interactive Techniques*.

- Singh, S. P., & Mittal, S. (2005). Vortex-induced oscillations at low Reynolds numbers: Hysteresis and vortex-shedding modes. *Journal of Fluids and Structures*, *20*(8), 1085–1104. https://doi.org/10.1016/j.jfluidstructs.2005.05.011

- Smogeli, O. N., Hover, F. S., & Triantafyllou, M. S. (2003). Force-Feedback Control in VIV Experiments. *Volume 3: Materials Technology; Ocean Engineering; Polar and Arctic Sciences and Technology; Workshops*, 685–695. https://doi.org/10.1115/OMAE2003-37340

- Srinil, N., & Zanganeh, H. (2012). Modelling of coupled cross-flow/in-line vortex-induced vibrations using double Duffing and van der Pol oscillators. *Ocean Engineering*, *53*, 83–97. https://doi.org/10.1016/j.oceaneng.2012.06.025

- Srinil, N., Zanganeh, H., & Day, A. (2013). Two-degree-of-freedom VIV of circular cylinder with variable natural frequency ratio: Experimental and numerical investigations. *Ocean Engineering*, *73*, 179–194. https://doi.org/10.1016/j.oceaneng.2013.07.024

- Sumer, B. M., & Fredsøe, J. (2006). *Hydrodynamics Around Cylindrical Structures* (Revised, Vol. 26). WORLD SCIENTIFIC. https://doi.org/10.1142/6248

- Tognarelli, M. A., Slocum, S. T., Frank, W. R., & Campbell, R. B. (2004). VIV Response of a Long Flexible Cylinder in Uniform and Linearly Sheared Currents. *All Days*, OTC-16338-MS. https://doi.org/10.4043/16338-MS

- Van Dyke, M., Abraham, R. H., Shaw, C. D., & Gollub, J. P. (1983). *An Album of Fluid Motion* and *Dynamics—The Geometry of Behavior; Part I: Periodic Behavior*. *American Journal of Physics*, *51*(1), 93–94. https://doi.org/10.1119/1.13408

- Vandiver, J. K., & Jong, J.-Y. (1987). The relationship between in-line and cross-flow vortex-induced vibration of cylinders. *Journal of Fluids and Structures*, *1*(4), 381–399. https://doi.org/10.1016/S0889-9746(87)90279-9

- Versteeg, H. K., & Malalasekera, W. (2007). *An introduction to computational fluid dynamics: The finite volume method* (2nd ed). Pearson Education Ltd.

- Wang, E., & Xiao, Q. (2016). Numerical simulation of vortex-induced vibration of a vertical riser in uniform and linearly sheared currents. *Ocean Engineering*, *121*, 492–515. https://doi.org/10.1016/j.oceaneng.2016.06.002

- Williamson, C. H. K. (1988). The existence of two stages in the transition to three-dimensionality of a cylinder wake. *Physics of Fluids*, *31*(11), 3165. https://doi.org/10.1063/1.866925

- Williamson, C. H. K. (1989). Oblique and parallel modes of vortex shedding in the wake of a circular cylinder at low Reynolds numbers. *Journal of Fluid Mechanics*, *206*, 579–627. https://doi.org/10.1017/S0022112089002429

- Williamson, C. H. K. (1996). Vortex Dynamics in the Cylinder Wake. *Annual Review of Fluid Mechanics*, *28*(1), 477–539. https://doi.org/10.1146/annurev.fl.28.010196.002401

- Williamson, C. H. K., & Govardhan, R. (2004). V ORTEX -I NDUCED V IBRATIONS. *Annual Review of Fluid Mechanics*, *36*(1), 413–455. https://doi.org/10.1146/annurev.fluid.36.050802.122128

- Williamson, C. H. K., & Roshko, A. (1988). Vortex formation in the wake of an oscillating cylinder. *Journal of Fluids and Structures*, *2*(4), 355–381. https://doi.org/10.1016/S0889-9746(88)90058-8

- Wu, J., Lie, H., Larsen, C. M., Liapis, S., & Baarholm, R. (2016). Vortex-induced vibration of a flexible cylinder: Interaction of the in-line and cross-flow responses. *Journal of Fluids and Structures*, *63*, 238–258. https://doi.org/10.1016/j.jfluidstructs.2016.03.001

- Zanganeh, H., & Srinil, N. (2014). Characterization of Variable Hydrodynamic Coefficients and Maximum Responses in Two-Dimensional Vortex-Induced Vibrations With Dual Resonances. *Journal of Vibration and Acoustics*, *136*(5), 051010. https://doi.org/10.1115/1.4027805

- Zdravkovich, M. M. (1997). *Flow around circular cylinders: A comprehensive guide through flow phenomena, experiments, applications, mathematical models, and computer simulations*. Oxford University Press.

- Zhao, M., & Cheng, L. (2011). Numerical simulation of two-degree-of-freedom vortex-induced vibration of a circular cylinder close to a plane boundary. *Journal of Fluids and Structures*, *27*(7), 1097–1110. https://doi.org/10.1016/j.jfluidstructs.2011.07.001

- Zhao, M., & Cheng, L. (2014). Vortex-induced vibration of a circular cylinder of finite length. *Physics of Fluids*, *26*(1), 015111. https://doi.org/10.1063/1.4862548Anderson, J. D., & Anderson, J. D. (2011). *Fundamentals of aerodynamics* (5th ed). McGraw-Hill.

Appendices

Appendix 1

In this section, results for all 36 cases under investigation, as well as the smooth cylinder case, are presented. The tables include values for lift and drag coefficients, in-line and cross-flow amplitudes, and the Strouhal number.

St	0.1791
$C_{D,rms}$	0.3396
$C_{L,rms}$	0.3067
y_{max}/D	0.5551
x_{rms}/D	0.0058

Table 6: Results from the smooth cylinder case

Groove Position	**30°**			**120°**			**150°**		
Groove Width	**Width = 10°**			**Width = 10°**			**Width = 10°**		
Groove Depth	**0.05D**	**0.075D**	**0.1D**	**0.05D**	**0.075D**	**0.1D**	**0.05D**	**0.075D**	**0.1D**
St	0.1771	0.1808	0.1811	0.1772	0.1832	0.1784	0.1782	0.1794	0.1773
$C_{D,rms}$	0.3389	0.3376	0.3377	0.3359	0.3359	0.3340	0.3421	0.3411	0.3414
$C_{L,rms}$	0.3028	0.3089	0.3100	0.3014	0.3034	0.3062	0.3147	0.3190	0.3199
y_{max}/D	0.5542	0.5543	0.5542	0.5516	0.5514	0.5511	0.5581	0.5581	0.5577
x_{rms}/D	0.0058	0.0058	0.0058	0.0057	0.0057	0.0057	0.0059	0.0058	0.0059

Table 7: Results for the p30, p120 and p150 cases with varying groove depths

Groove Position	**90°**								
Groove Width	**Width = 10°**			**Width = 15°**			**Width = 20°**		
Groove Depth	**0.05D**	**0.075D**	**0.1D**	**0.05D**	**0.075D**	**0.1D**	**0.05D**	**0.075D**	**0.1D**
St	0.1784	0.1738	0.1826	0.1788	0.1732	0.1764	0.1787	0.1824	0.1746
$C_{D,rms}$	0.3280	0.3268	0.3265	0.3166	0.3156	0.3161	0.3023	0.3025	0.3010
$C_{L,rms}$	0.3038	0.3062	0.3108	0.2978	0.3031	0.3086	0.2864	0.2934	0.3025
y_{max}/D	0.5452	0.5548	0.5449	0.5346	0.5341	0.5342	0.5199	0.5199	0.5196
x_{rms}/D	0.0056	0.0056	0.0056	0.0054	0.0054	0.0054	0.0052	0.0052	0.0052

Table 8: Results for the p90 cases with varying groove widths and depths

Groove Position	**60°**								
Groove Width	**Width = 10°**			**Width = 15°**			**Width = 20°**		
Groove Depth	**0.05D**	**0.075D**	**0.1D**	**0.05D**	**0.075D**	**0.1D**	**0.05D**	**0.075D**	**0.1D**
St	0.1816	0.1823	0.1823	0.1793	0.1829	0.1799	0.1779	0.1801	0.1779
$C_{D,rms}$	0.3433	0.3414	0.3414	0.3482	0.3489	0.3480	0.3563	0.3581	0.3570
$C_{L,rms}$	0.3261	0.3301	0.3340	0.3465	0.3516	0.3552	0.3667	0.3773	0.3842
y_{max}/D	0.5612	0.5610	0.5610	0.5690	0.5694	0.5693	0.5789	0.5802	0.5806
x_{rms}/D	0.0059	0.0059	0.0059	0.0060	0.0060	0.0060	0.0061	0.0062	0.0062

Table 9: Results for the p60 cases with varying groove widths and depths

Groove Position	**180°**								
Groove Width	**Width = 10°**			**Width = 15°**			**Width = 20°**		
Groove Depth	**0.05D**	**0.075D**	**0.1D**	**0.05D**	**0.075D**	**0.1D**	**0.05D**	**0.075D**	**0.1D**
St	0.1781	0.1781	0.1787	0.1781	0.1793	0.1779	0.1786	0.1793	0.1760
$C_{D,rms}$	0.3397	0.3398	0.3389	0.3410	0.3403	0.3403	0.3428	0.3423	0.3413
$C_{L,rms}$	0.3092	0.3109	0.3121	0.3114	0.3148	0.3163	0.3131	0.3180	0.3181
y_{max}/D	0.5558	0.5558	0.5555	0.5566	0.5567	0.5563	0.5579	0.5579	0.5577
x_{rms}/D	0.0058	0.0058	0.0058	0.0058	0.0058	0.0058	0.0059	0.0059	0.0059

Table 10: Results for the p180 cases with varying groove widths and depths

Mesh	y_{max}/D [-]	x_{rms}/D [-]	$C_{D,rms}$ [-]	$C_{L,rms}$ [-]
105 000 cells	0.5452	0.005614	0.30377	0.32799
39 000 cells	0.5464	0.005612	0.31085	0.32756
30 000 cells	0.54296	0.00554	0.30555	0.32322

Table 11: Results for the mesh convergence study

Appendix 2

This section displays several key input files that were essential for executing the Pimplefoam algorithm within OpenFOAM.

A2.1. *controlDict*

As a critical configuration file, the controlDict file guides the overall execution of the OpenFOAM simulations. It determines the start and end times of the simulation, the time step size, data write frequency, and the selection of numerical schemes, among other important aspects.

The following is the controlDict file used in the current setup:

```
/*--------------------------------*- C++ -*----------------------------------*\
| =========                 |                                                 |
| \\      /  F ield         | OpenFOAM: The Open Source CFD Toolbox           |
|  \\    /   O peration     | Version:  2.3.0                                 |
|   \\  /    A nd           | Web:      www.OpenFOAM.org                      |
|    \\/     M anipulation  |                                                 |
\*---------------------------------------------------------------------------*/
FoamFile
{
    version     2.0;
    format      ascii;
    class       dictionary;
    location    "system";
    object      controlDict;
}
// * * * * * * * * * * * * * * * * * * * * * * * * * * * * * * * * * * * * * //

application     pimpleFoam;
```

```
startFrom       latestTime;

startTime       0;

stopAt          endTime;

endTime         7;

deltaT          7.5e-06;

writeControl    adjustableRunTime;

writeInterval   0.1;

purgeWrite      0;

writeFormat     binary;

writePrecision  6;

writeCompression off;

timeFormat      general;

timePrecision   6;

runTimeModifiable true;

adjustTimeStep  yes;

maxCo           0.5;

functions
{

forces1
{
    type          forces;

    libs          ("libforces.so");

    writeControl  timeStep;
    timeInterval  1;

    log           yes;

    patches       ("cylinder");
    rho           rhoInf;     // Indicates incompressible
    log           true;
    rhoInf        1; // Redundant for incompressible
    origin (0 0 0);
    coordinateRotation
        {
```

```
        type            axesRotation;
        e2              (0 1 0);
        e1              (1 0 0);
      }
}
/*
    vorticity1
    {
       type       vorticity;
       libs       (fieldFunctionObjects);
    }
*/
}

// ************************************************************************* //
```

A2.2. *dynamicMeshDict*

The dynamicMeshDict file is an essential component for simulations involving moving or adaptive grids. It provides the necessary parameters for defining the mesh motion or changes, thereby enabling the accurate capture of flow characteristics around moving or deforming bodies.

The following is the dynamicMeshDict file used in the current setup:

```
/*--------------------------------*- C++ -*----------------------------------*\
| =========                 |                                                 |
| \\      /  F ield         | OpenFOAM: The Open Source CFD Toolbox           |
|  \\    /   O peration     | Version:  v1912                                 |
|   \\  /    A nd           | Website:  www.openfoam.com                      |
|    \\/     M anipulation  |                                                 |
\*---------------------------------------------------------------------------*/
FoamFile
{
    version     2.0;
    format      ascii;
    class       dictionary;
    object      dynamicMeshDict;
}
// * * * * * * * * * * * * * * * * * * * * * * * * * * * * * * * * * * * * * //
motionSolverLibs (sixDoFRigidBodyMotion);

motionSolver    sixDoFRigidBodyMotion;
```

```
displacementLaplacianCoeffs
{
    diffusivity     uniform 1;
}
dynamicFvMesh       dynamicMotionSolverFvMesh;

dynamicOversetFvMeshCoeffs
{
//    layerRelax 0.3;
}

sixDoFRigidBodyMotionCoeffs
{
    accelerationRelaxation 1.0;
    accelerationDamping 1.0;

    patches         (cylinder);
    innerDistance   0.1;
    outerDistance   0.11;

    mass            0.03575;
   centreOfMass    (0.0 0.0 0.0);
   momentOfInertia (1.144E-08 1.144E-08 1.144E-08);

   g               (0 0 0);
   rho             rhoInf;
   rhoInf          14817.1;
   report          on;

   solver
   {
      type symplectic;
   }
   constraints
   {
    zPlan
    {
      sixDoFRigidBodyMotionConstraint   plane;
      normal ( 0 0 1);
    }
    zAxis
    {
```

```
        sixDoFRigidBodyMotionConstraint orientation;
        centreOfRotation              (0 0 1);
    }
}
restraints
{
    spring
    {
        sixDoFRigidBodyMotionRestraint linearSpring;

        anchor         (0.0 0.0 0.0);
        refAttachmentPt (0.0 0.0 0.0);
        stiffness      78.42;
        damping        0.00;
        restLength     0;
    }
}
}
// ************************************************************************* //
```

A2.3. *decomposeParDict*

This file plays a crucial role in enabling parallel computing for the simulations. It provides the necessary parameters to partition the computational domain across multiple processors, improving the efficiency of large-scale simulations.

The following is the decomposeParDict file used in the current setup:

```
/*--------------------------------*- C++ -*----------------------------------*\
| =========                 |                                                 |
| \\      /  F ield         | OpenFOAM: The Open Source CFD Toolbox           |
|  \\    /   O peration     | Version:  2.3.0                                 |
|   \\  /    A nd           | Web:      www.OpenFOAM.org                      |
|    \\/     M anipulation  |                                                 |
\*---------------------------------------------------------------------------*/
FoamFile
{
    version     2.0;
    format      ascii;
    class       dictionary;
    object      decomposeParDict;
}
```

```
// * * * * * * * * * * * * * * * * * * * * * * * * * * * * * * * * * * * * * * * * * * * * * * * * * //
numberOfSubdomains 24;

method          scotch;
// method          ptscotch;
simpleCoeffs
{
    n               (4 1 1);
    delta           0.001;
}
hierarchicalCoeffs
{
    n               (3 2 1);
    delta           0.001;
    order           xyz;
}
manualCoeffs
{
    dataFile        "cellDecomposition";
}
// ************************************************************************* //
```

A2.4. *fvSchemes*

This input file is pivotal for setting up the discretization schemes for the various terms in the governing equations of the flow.

The following is the fvSchemes file used in the current setup:

```
/*--------------------------------*- C++ -*----------------------------------*\
| =========                 |                                                 |
| \\      /  F ield         | OpenFOAM: The Open Source CFD Toolbox           |
|  \\    /   O peration     | Version:  2.3.0                                 |
|   \\  /    A nd           | Web:      www.OpenFOAM.org                      |
|    \\/     M anipulation  |                                                 |
\*---------------------------------------------------------------------------*/
FoamFile
{
    version     2.0;
    format      ascii;
```

```
    class       dictionary;
    location    "system";
    object      fvSchemes;
}
// * * * * * * * * * * * * * * * * * * * * * * * * * * * * * * * * * * * * * * * * * * * * //

ddtSchemes
{
    default         backward;
}

gradSchemes
{
    default         Gauss linear;
}

divSchemes
{
    default         none;
    div(phi,U)      Gauss cubic;
    div((nuEff*dev(T(grad(U))))) Gauss linear;
    div((nuEff*dev2(T(grad(U))))) Gauss linear;
}

laplacianSchemes
{
    default         Gauss linear corrected;
    laplacian(diffusivity,cellMotionU) Gauss linear uncorrected;
}

interpolationSchemes
{
    default         linear;
}

snGradSchemes
{
    default         corrected;
}

fluxRequired
{
```

```
    default         no;
    pcorr           ;
    p               ;
}

// ************************************************************************* //
```

A2.5. *fvSolution*

The fvSolution file is responsible for specifying the solvers used to tackle the system of algebraic equations resulting from the discretization of the Navier-Stokes equations. It also includes parameters for controlling the convergence of these solvers and can play a substantial role in the overall computational efficiency of the simulations.

The following is the fvSolution file used in the current setup:

```
/*--------------------------------*- C++ -*----------------------------------*\
| =========                 |                                                 |
| \\      /  F ield         | OpenFOAM: The Open Source CFD Toolbox           |
|  \\    /   O peration     | Version:  2.3.0                                 |
|   \\  /    A nd           | Web:      www.OpenFOAM.org                      |
|    \\/     M anipulation  |                                                 |
\*---------------------------------------------------------------------------*/
FoamFile
{
    version     2.0;
    format      ascii;
    class       dictionary;
    location    "system";
    object      fvSolution;
}
// * * * * * * * * * * * * * * * * * * * * * * * * * * * * * * * * * * * * * //

solvers
{
    pcorr
    {
        solver          GAMG;
        tolerance       0.02;
        relTol          0;
        smoother        GaussSeidel;
```

```
    nPreSweeps      0;
    nPostSweeps     2;
    cacheAgglomeration no;
    nCellsInCoarsestLevel 10;
    agglomerator    faceAreaPair;
    mergeLevels     1;
}

p
{
    solver          GAMG;
    tolerance       0;
    relTol          0.01;
    smoother        GaussSeidel;
    nPreSweeps      0;
    nPostSweeps     2;
    cacheAgglomeration no;
    nCellsInCoarsestLevel 10;
    agglomerator    faceAreaPair;
    mergeLevels     1;
}

pFinal
{
    $p;
    tolerance       1e-06;
    relTol          0;
}

pcorrFinal
{
    $pcorr;
    tolerance       1e-06;
    relTol          0;
}
U
{
    solver          smoothSolver;
    smoother        symGaussSeidel;
    tolerance       1e-05;
    relTol          0.01;
}
```

```
    UFinal
    {
        $U;
        tolerance       1e-05;
        relTol          0;
    }

    cellMotionUx
    {
        solver          PCG;
        preconditioner  DIC;
        tolerance       1e-08;
        relTol          0;
    }
    cellMotionUxFinal
    {
        solver          PCG;
        preconditioner  DIC;
        tolerance       1e-08;
        relTol          0;
    }

    "cellDisplacement.*"
    {
        solver          GAMG;
        tolerance       1e-5;
        relTol          0;
        smoother        GaussSeidel;
        cacheAgglomeration true;
        nCellsInCoarsestLevel 10;
        agglomerator    faceAreaPair;
        mergeLevels     1;
    }

}

PIMPLE
{
    correctPhi          yes;
    nOuterCorrectors    3;
    nCorrectors         1;
```

```
    nNonOrthogonalCorrectors 0;
    pRefCell 1001;
    pRefValue 0;
}

relaxationFactors
{
    fields
    {
    }
    equations
    {
        "U.*"           1;
    }
}

// ************************************************************************* //
```

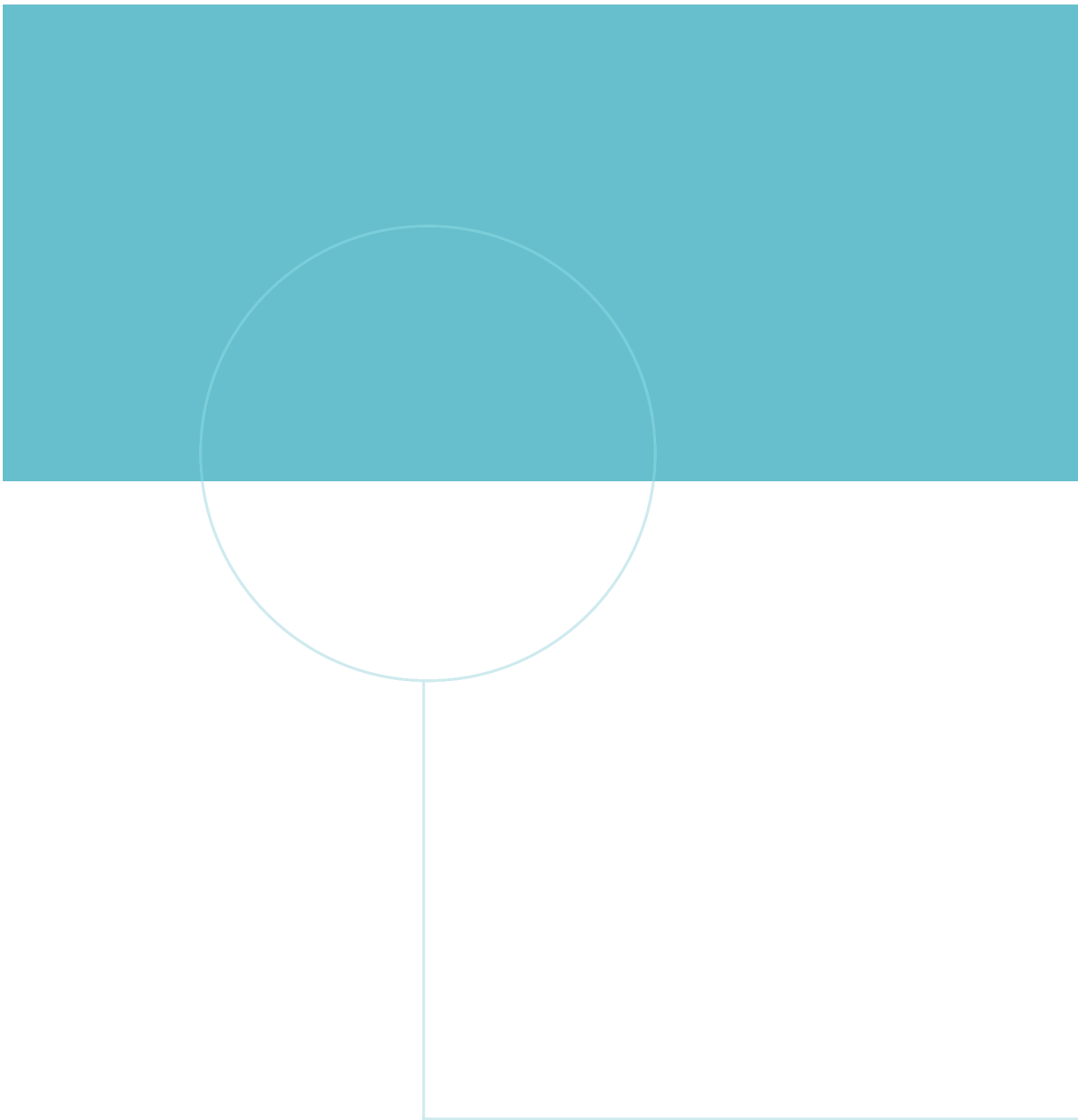

NTNU

Norwegian University of
Science and Technology